

**Plasma-Enhanced Pulsed Laser  
Deposition of metal oxynitride thin  
films for photoelectrochemical  
water splitting**

**Matthew Robert Hill**

Doctor of Philosophy

University of York

Physics

July 2024

# Abstract

Plasma-enhanced pulsed laser deposition (PE-PLD) is a novel thin film deposition method which employs radio-frequency plasmas and laser-ablated plasma plumes to produce semiconductor thin films. A high-powered, pulsed laser ablates material from a metal target into a plasma plume, which interacts with non-metal inductively-coupled plasma species to form metal compound material that deposits onto a substrate. PE-PLD has been shown to produce high-quality metal oxide thin films with many applications, including photocatalysts which use solar energy to produce hydrogen fuel from water splitting. PE-PLD remains an active area of research, particularly elucidating its underlying plasma physics and chemistry, such that thin films can be created according to specific criteria rather than empirical observation. This work centres around the suitability of PE-PLD in producing metal oxynitride thin films for photocatalysis.

This thesis presents results from modelling the laser ablation of different photocatalytic metals using the code POLLUX, showing the electron temperature and mass density of the plasma plume both increased with the atomic number of the material, whilst the mass density of the material had no observed effect on the electron temperature or particle density of the plume.

Additionally, the TALIF diagnostic provided absolute measurements of ground-state atomic O and N densities for a range of low-pressure O<sub>2</sub>/N<sub>2</sub> plasma mixtures, showing the relative flow input of O<sub>2</sub> and N<sub>2</sub> had the greatest control over the O:N atomic density ratio, allowing it to change by up to a factor of 100.

Finally, the structure and chemical composition of deposited metal oxynitride thin films were analysed with different diagnostics, showing a consistent lack of nitrogen present on the films and lack of visible light absorption, highlighting many areas of improvement for PE-PLD in producing oxynitride films, such as understanding interactions between O<sub>2</sub>/N<sub>2</sub> plasma species and their effect on deposition.

# Contents

<b>Abstract</b>	<b>2</b>
<b>List of Tables</b>	<b>7</b>
<b>List of Figures</b>	<b>8</b>
<b>Acknowledgements</b>	<b>17</b>
<b>Declaration</b>	<b>19</b>
<b>1 Introduction</b>	<b>20</b>
1.1 Motivation . . . . .	20
1.2 Thesis outline . . . . .	22
<b>2 Scientific Background</b>	<b>23</b>
2.1 Plasma-enhanced pulsed laser deposition . . . . .	23
2.2 Interaction of lasers with solids and plasmas . . . . .	28
2.2.1 Reflection, absorption, and ablation of solid material . . . . .	28
2.2.2 Inverse-Bremsstrahlung absorption . . . . .	29
2.3 Expansion of a plasma plume . . . . .	30
2.3.1 Plasma plume interactions with a vacuum background . . . . .	30
2.3.2 Plasma plume interactions with a non-vacuum background . . . . .	31
2.4 Deposition of plasma material onto a substrate . . . . .	32
2.5 Radio-frequency plasmas . . . . .	34
2.5.1 Capacitively and inductively coupled plasmas . . . . .	35
2.6 Equilibrium regimes . . . . .	36
2.7 Photocatalytic thin films . . . . .	37

<i>CONTENTS</i>	4
2.7.1 Metal oxide thin films . . . . .	37
2.7.2 Metal oxynitride thin films . . . . .	38
<b>3 Methodology</b>	<b>40</b>
3.1 Experimental setup . . . . .	40
3.2 POLLUX model . . . . .	44
3.2.1 Mesh . . . . .	44
3.2.2 Equation of State . . . . .	45
3.2.3 Energy absorption . . . . .	46
3.2.4 Ion and electron temperatures . . . . .	47
3.2.5 Mass transport and the FCT model . . . . .	48
3.2.6 Energy transport and the ICCG method . . . . .	48
3.2.7 Outputs from POLLUX . . . . .	49
3.3 TALIF plasma diagnostic . . . . .	50
3.3.1 Calibration with noble gases to obtain absolute atomic densities . . . . .	54
3.3.2 Collisional quenching . . . . .	55
3.3.3 Saturation of laser energy . . . . .	56
3.3.4 Calculating the atomic density . . . . .	59
3.3.5 Constants and error estimation . . . . .	60
3.3.6 Spectral Scans . . . . .	61
3.3.7 Fluorescence Decay . . . . .	63
3.4 Thin film diagnostics . . . . .	64
3.4.1 Scanning electron microscopy (SEM) . . . . .	64
3.4.2 Energy-dispersive X-ray spectroscopy (EDX) . . . . .	66
3.4.3 Ultraviolet–visible (UV/Vis) absorption spectroscopy . . . . .	67
3.4.4 X-Ray Diffraction (XRD) . . . . .	67
3.4.5 X-ray photoelectron spectroscopy (XPS) . . . . .	69
<b>4 Modelling laser ablation of metal targets</b>	<b>73</b>
4.1 Laser ablation of titanium metal . . . . .	73
4.2 Investigating the effects of material properties on titanium plasma plumes . . . . .	75
4.3 Comparison of the laser ablation of plasma plumes from different materials . . . . .	81
4.4 Conclusions . . . . .	83

<b>5</b>	<b>Characterising atomic O and N densities in a low-pressure O<sub>2</sub>/N<sub>2</sub> plasma</b>	<b>85</b>
5.1	Atomic density of pure oxygen . . . . .	85
5.2	Atomic N density of pure nitrogen . . . . .	88
5.3	Atomic density of oxygen and nitrogen plasma admixtures . . . . .	90
5.4	Conclusions . . . . .	96
<b>6</b>	<b>Analysis of thin films deposited by PE-PLD</b>	<b>99</b>
6.1	Titanium oxide thin films . . . . .	100
6.1.1	SEM and EDX Analysis - Film composition and surface morphology .	100
6.1.2	XPS analysis - Film chemical stoichiometry . . . . .	103
6.1.3	XRD analysis - Film crystal structure . . . . .	105
6.1.4	UV/Vis absorption spectroscopy - Film absorption . . . . .	106
6.2	Titanium oxynitride and nitride thin films . . . . .	107
6.2.1	SEM and EDX Analysis - Film composition and surface morphology .	107
6.2.2	XPS analysis - Film chemical stoichiometry . . . . .	113
6.2.3	XRD analysis - Film crystal structure . . . . .	116
6.2.4	UV/Vis absorption spectroscopy - Film absorption . . . . .	116
6.3	Tantalum oxide thin films . . . . .	120
6.3.1	SEM and EDX Analysis - Film composition and surface morphology .	121
6.3.2	XPS analysis - Film chemical stoichiometry . . . . .	122
6.3.3	UV/Vis absorption spectroscopy - Film absorption . . . . .	123
6.4	Tantalum oxynitride thin films . . . . .	123
6.4.1	SEM and EDX Analysis - Film composition and surface morphology .	123
6.4.2	XPS analysis - Film chemical stoichiometry . . . . .	125
6.4.3	UV/Vis absorption spectroscopy - Film absorption . . . . .	125
6.5	Conclusions . . . . .	126
6.6	Suggestions for future investigation . . . . .	127
<b>7</b>	<b>Conclusions</b>	<b>128</b>
7.1	Conclusions with respect to project aims . . . . .	128
7.2	Suggestions for future work . . . . .	130
<b>A</b>	<b>List of publications and communications</b>	<b>133</b>

<i>CONTENTS</i>	6
<b>List of References</b>	<b>134</b>

# List of Tables

3.1	Constructed tabular Chart-D EoS for Al, Au, Zn, Cu, Ti and Ta. . . . .	46
3.2	Constructed tabular Chart-D EoS for Al, Au, Zn, Cu, Ti and Ta . . . . .	50
3.3	Constants used for calculation of absolute atomic densities using equation 3.8.	60
6.1	Deposition conditions of the 7 thin films. All thin films were deposited onto a dual quartz/silicon substrate for 90 minutes, as outlined in section 3.1. . . .	100
6.2	Calculation for the chemical composition of the TiO <sub>2</sub> film using 10 kV 1,000x EDX analysis. Uncertainties in the percentage of average atomic content are derived from the standard deviations of the percentages of atomic content without silicon. . . . .	103
6.3	Average stoichiometries of the three TiON thin film deposition attempts calculated by EDX. A negligible amount of nitrogen was detected by EDX in the third attempt, despite the O:N ratio of 10:90, causing the atomic percentage of N present to equal 0%, resulting in no nitrogen in the stoichiometry calculation. The derivation of the uncertainty values is described in table 6.2.	111
6.4	Average stoichiometries of the three TiON thin film deposition attempts calculated by XPS. A negligible amount of nitrogen was detected by XPS in all three attempts, resulting in no nitrogen in the stoichiometry calculation. . . .	114
6.5	The average percentage of silicon content detected by EDX compared with the maximum UV/Vis absorbance for each of the five deposited titanium compound thin films. . . . .	119

# List of Figures

2.1	Schematic diagram of a typical PLD setup. . . . .	24
2.2	Schematic diagram of the PE-PLD setup in the York Plasma Institute Laboratories. . . . .	27
2.3	Decay of laser intensity during absorption into a solid target. . . . .	29
2.4	Illustration of fundamental process deposition onto a substrate and film growth. Steps shown are: a) nucleation; b) island growth; c) island coalescence and grain formation; d) island coarsening and formation of polycrystalline grains; e) further development of grains and film growth. . . . .	33
2.5	Standard configuration for low pressure RF plasma reactors. Left: CCP; Right: ICP. . . . .	36
2.6	UV-visible diffuse reflectance spectra of TaON and Ta <sub>2</sub> O <sub>5</sub> taken from Hitoki et al. [1]. . . . .	38
3.1	Schematic diagram of the PE-PLD apparatus in the York Plasma Institute Laboratories. . . . .	42
3.2	Photograph of substrate holder with a quartz and silicon hybrid substrate seen in the holder window. A small silicon shard is attached to a quartz disc. . . . .	43
3.3	Photograph of a TiON thin film deposited onto a quartz/silicon hybrid substrate. . . . .	44
3.4	Flowchart summarising the POLLUX algorithm. . . . .	45
3.5	TALIF excitation scheme. The laser selectively excites an electron from the ground state (level 1) of the atom to level 2 using two photons absorbed simultaneously. This electron subsequently decays to level 3, emitting a photon (e.g. 844 nm in case of oxygen) that is measured with e.g. an iCCD camera. . . . .	51

3.6	Schematic diagram of the TALIF diagnostic setup in the York Plasma Institute Laboratories. The green dotted line indicates the pulsed laser beam, traveling through the attenuators, mirrors, and lens, entering the GEC chamber containing the plasma, and terminating at a beam dump. The energy probe measures laser energy and is removed during fluorescence measurements. . . .	52
3.7	Timing scheme for the digital delay generator (DDG) in the TALIF setup in the York Plasma Institute Laboratories. The DDG externally pulses the plasma on at time $T_0$ , lasting 10 ms. The plasma pulse is powered off for 90 ms, creating a 10% duty cycle, coinciding with the laser pulse rate. The time at which the Q-switch triggers, $T_{Q-Switch}$ , can vary relative to the camera triggering, $T_{camera}$ , to study fluorescence at different times in the afterglow. However, the laser flashlamp always triggers at time $T_{flashlamp} = T_{Q-Switch} - 225\mu s$ to maximise the output energy of the tuneable laser. The camera gate-width was set to 200 ns. . . . .	54
3.8	Two-photon excitation scheme for atomic oxygen and xenon [2]. . . . .	55
3.9	Two-photon excitation scheme for atomic nitrogen and krypton [3]. . . . .	55
3.10	Schematic comparing the TALIF excitation scheme of a measured plasma species, e.g. atomic oxygen or nitrogen, with that of a reference gas species, e.g. xenon or krypton, with collisional quenching taken into account. In this schematic, the noble gas has an $n\%$ chance to decay from excited state 2 into lower excited state 3, which can be measured, and an $m\%$ chance to decay into lower excited state 4, which cannot be measured with the same optical filter. . . . .	56
3.11	Energy saturation curve for oxygen at a gas pressure of 20 Pa. The signal begins saturating after $E^2 \approx 5.3 \times 10^6 (\mu J)^2$ , or $E = 2309 \mu J$ . Therefore, 850 $\mu J$ was the approximate pulse energy chosen for oxygen experiments. . . . .	57
3.12	Energy saturation curve for xenon at a gas pressure of 20 Pa. The signal begins saturating after $E^2 \approx 2.4 \times 10^5 (\mu J)^2$ , or $E = 493 \mu J$ . Therefore, 305 $\mu J$ was the approximate pulse energy chosen for xenon calibration. . . . .	58

3.13 Energy saturation curve for nitrogen at a gas pressure of 20 Pa. The energy did not saturate within the measured range, but it was observed that increasing the laser energy increased plasma emissions at an increased rate, resulting in the fluorescence becoming more difficult to observe. Therefore, laser energy of approximately  $E = 435\mu\text{J}$  ( $E^2 = \sim 1.8 \times 10^5(\mu\text{J})^2$ ) was chosen for nitrogen experiments. . . . . 58

3.14 Energy saturation curve for krypton at a gas pressure of 20 Pa. The energy began saturating after  $E = 219\mu\text{J}$  ( $E^2 = \sim 4.7 \times 10^4(\mu\text{J})^2$ ). Laser energy of approximately  $E = 230\mu\text{J}$  ( $E^2 = \sim 1.8 \times 10^5(\mu\text{J})^2$ ) was chosen for krypton calibration to optimise fluorescence intensity. . . . . 59

3.15 Example of a fluorescence signal taken from the iCCD camera viewed on the Andor SOLIS software in the TALIF experimental setup in the York Plasma Institute Laboratories. Displays the fluorescence signal of an  $\text{O}_2$  plasma at 15 Pa pressure and 600 W power at the peak wavelength of fluorescence (225.65 nm). . . . . 62

3.16 Example of a spectral profile of atomic oxygen plasma at 20 Pa GEC chamber pressure and 600 W RF power. The spectral width of the laser is assumed to be the dominant broadening mechanism, which has a Gaussian profile, hence the Gaussian fit applied to the fluorescence. The area under this Gaussian is defined as the total fluorescence signal,  $S$ . . . . . 63

3.17 Example of a fitting of an exponential decay curve to a fluorescence signal of atomic oxygen plasma at 20 Pa GEC chamber pressure and 600 W RF power. The effective lifetime,  $\tau_{eff}$ , is derived from the decay constant of the exponential curve, which is required for calculating the optical branching ratio,  $b$ , and in turn the atomic density of the plasma. . . . . 64

3.18 Schematic of an SEM setup. . . . . 65

3.19 Schematic diagram of characteristic X-ray emission. As the high-energy electron beam causes inner shell electrons to be emitted, electrons from higher energy levels relax and occupy the holes left behind, emitting characteristic X-ray photons. . . . . 66

3.20	UV-Visible Spectrophotometer schematic. Wavelengths at intensity $I_0$ emitted by the light source are reflected off the monochromator, separating the wavelengths as they travel back through the sample and reach the detector, which measures the transmitted intensity, $I$ . . . . .	68
3.21	X-ray diffraction schematic. . . . .	69
3.22	Plan view of XPS schematic used in the University of York Department of Physics [4]. . . . .	70
3.23	Example of a full XPS spectrum of a thin film deposited in the York Plasma Institute. The intensity of each peak is relative to that of a carbon reference species, whose peak is located between binding energy 200-300 eV. The two peaks close together at approximately 460-465 eV correspond to the Ti $2p_{3/2}$ and $2p_{1/2}$ electrons detected by the diagnostic, which can also be seen in figure 3.24. The peak between 500-600 eV corresponds to O $1s$ electrons, and the peak in the 900-1000 eV range represents O electrons emitted due to the Auger effect [5]. . . . .	71
3.24	XPS figure identical to the spectrum in figure 3.23, with curve fitting on two key peaks within the 450-470 eV range. The raw data is shown by the black curve. The peak sum is the summation of all fitted peaks on top of the background. In this case, the background is a Shirley background, used to account for the effect of inelastic scattering of electrons specifically in XPS. The other two peaks in this example correspond to the Ti $2p_{3/2}$ and $2p_{1/2}$ electrons detected by the diagnostic. . . . .	72
4.1	Results of the laser ablation simulation showing the distribution of the electron temperature in an ablated titanium plasma plume calculated at 5 ns after the laser pulse. The laser fluence was $100.5 \text{ J cm}^{-2}$ and the laser focus was $100 \mu\text{m}$ . . . . .	74
4.2	Spatial distribution of the simulated axial velocity (top) and electron temperature (bottom) profiles of a titanium plasma plume for different times after the start of the 16 ns laser pulse. The laser fluence was $100.5 \text{ J cm}^{-2}$ and the laser focus was $100 \mu\text{m}$ . . . . .	75

4.3	1D plot comparing the spatial distribution of (a) the electron temperature and (b) the particle density of an ablated titanium plasma plume with varied atomic number 25 ns after the laser pulse. The default atomic number of titanium is 22. The laser fluence was $100.5 \text{ J cm}^{-2}$ and the laser focus was $100 \text{ }\mu\text{m}$ . . . . .	77
4.4	1D plot comparing the spatial distribution of (a) the electron temperature and (b) the particle density of an ablated titanium plasma plume with varied mass density 25 ns after the laser pulse. The default mass density of titanium is $4.506 \text{ g cm}^{-3}$ . The laser fluence was $100.5 \text{ J cm}^{-2}$ and the laser focus was $100 \text{ }\mu\text{m}$ . . . . .	79
4.5	Comparison of the spatial distribution of the electron temperature of an ablated titanium plasma plume with varied melting temperature 25 ns after the laser pulse. The default melting temperature of titanium is $1.675 \text{ meV}$ . The laser fluence was $100.5 \text{ J cm}^{-2}$ and the laser focus was $100 \text{ }\mu\text{m}$ . . . . .	80
4.6	Comparison of the spatial distribution of the electron temperature of an ablated titanium plasma plume with varied thermal conductivity coefficient 25 ns after the laser pulse. The default thermal conductivity of titanium is $22 \text{ W m}^{-1}\text{K}^{-1}$ . The laser fluence was $100.5 \text{ J cm}^{-2}$ and the laser focus was $100 \text{ }\mu\text{m}$ . . . . .	81
4.7	The spatial distribution of the electron temperature of plasma plumes from six different materials, 25 ns after the laser pulse. The laser fluence was $100.5 \text{ J cm}^{-2}$ and the laser focus was $100 \text{ }\mu\text{m}$ . . . . .	82
4.8	The spatial distribution of the particle density of plasma plumes from six different materials, 25 ns after the laser pulse. The laser fluence was $100.5 \text{ J cm}^{-2}$ and the laser focus was $100 \text{ }\mu\text{m}$ . . . . .	83
5.1	The evolution of atomic density of a pure oxygen plasma with respect to applied radiofrequency power. GEC chamber pressure is fixed at $20 \text{ Pa}$ and images are taken $700 \text{ }\mu\text{s}$ in the afterglow of the plasma pulse. . . . .	86
5.2	The evolution of atomic density of a pure oxygen plasma with respect to GEC chamber pressure. Applied radiofrequency power is fixed at $600 \text{ W}$ and images are taken $700 \text{ }\mu\text{s}$ in the afterglow of the plasma pulse. . . . .	87

5.3	(a) Decay of atomic nitrogen plasma at 20 Pa GEC chamber pressure and 600 W RF power; (b) background-subtracted fluorescence counts in the plasma afterglow. Uncertainties in counts were derived from the square root of the number of counts. . . . .	89
5.4	The evolution of atomic density of a pure nitrogen plasma with respect to applied radiofrequency power. GEC chamber pressure is fixed at 20 Pa and images are taken 700 $\mu$ s in the afterglow of the plasma pulse. . . . .	91
5.5	The evolution of atomic density of a pure nitrogen plasma with respect to GEC chamber pressure. Applied radiofrequency power is fixed at 600 W and images are taken 700 $\mu$ s in the afterglow of the plasma pulse. . . . .	91
5.6	The evolution of atomic density of oxygen in a 50/50 oxygen and nitrogen plasma admixture with respect to applied radiofrequency power. Chamber pressure is fixed at 20 Pa and images were taken 700 $\mu$ s in the afterglow of the plasma pulse. . . . .	92
5.7	The evolution of atomic density of oxygen in a 50/50 oxygen and nitrogen plasma admixture with respect to GEC chamber pressure. The applied radiofrequency power is fixed at 600 W and images are taken 700 $\mu$ s in the afterglow of the plasma pulse. . . . .	92
5.8	The evolution of atomic density of nitrogen in a 50/50 oxygen and nitrogen plasma admixture with respect to applied radiofrequency power. GEC chamber pressure is fixed at 20 Pa and images are taken 700 $\mu$ s in the afterglow of the plasma pulse. . . . .	93
5.9	The evolution of atomic density of nitrogen in a 50/50 oxygen and nitrogen plasma admixture with respect to pressure. Applied radiofrequency power was set to 600 W and images were taken 700 $\mu$ s in the afterglow of the plasma pulse. . . . .	93
5.10	The evolution of atomic density of oxygen and nitrogen with respect to percentage mix of oxygen content in an oxygen and nitrogen plasma admixture. The applied radiofrequency power was set to 600 W, the total pressure of the GEC chamber was set to 20 Pa, and images were taken 700 $\mu$ s in the afterglow of the plasma pulse. When the oxygen mix is 10%, the nitrogen mix is assumed to be 90%, and so on. . . . .	95

5.11 The evolution of the ratio of the atomic density of oxygen and nitrogen with respect to applied RF power in an oxygen and nitrogen plasma admixture. The total chamber pressure was set to 20 Pa and images were taken 700  $\mu$ s in the afterglow of the plasma pulse. . . . . 96

5.12 The evolution of the ratio of the atomic density of oxygen and nitrogen with respect to GEC chamber pressure in an oxygen and nitrogen plasma admixture. The applied radiofrequency power was set to 600 W and images were taken 700  $\mu$ s in the afterglow of the plasma pulse. . . . . 97

5.13 The evolution of the ratio of the density of atomic oxygen to nitrogen with respect to percentage content of oxygen. Applied radiofrequency power was set to 600 W, the total chamber pressure was set to 20 Pa, and images were taken 700  $\mu$ s in the afterglow of the plasma pulse. When the oxygen mix is 10%, the nitrogen mix is assumed to be 90%, and so on. . . . . 98

6.1 10 kV 1,000x SEM image of the bottom edge of the deposition area for the TiO<sub>2</sub> thin film deposited at 600 W RF power and 15 Pa pressure. . . . . 101

6.2 10 kV 1'000x EDX spectrum of TiO<sub>2</sub> thin film. . . . . 102

6.3 XPS spectrum of TiO<sub>2</sub> 2 p electrons from the titanium oxide thin film. . . . . 104

6.4 XPS spectrum of O 1s electrons from the titanium oxide thin film. . . . . 104

6.5 XRD spectrum of TiO<sub>2</sub> thin film. The peak at approximately 69° signifies (100) silicon. . . . . 106

6.6 UV/Vis absorption spectrum for deposited TiO<sub>2</sub> film, with absorption profile for plain quartz substrate subtracted. . . . . 107

6.7 10 kV 1,000x SEM image of part of the deposition area for the O:N = 50:50 TiON thin film no. 1 deposited at 300 W RF power and 20 Pa pressure. The large white cluster near the top left corner of the image is carbon dirt. . . . . 108

6.8 10 kV 1,000x SEM image of part of the deposition area for the O:N = 50:50 TiON thin film no. 2 deposited at 600 W RF power and 20 Pa pressure. The large, dark lines seen at the top of the image indicate slight scratching of the silicon substrate. . . . . 109

6.9	10 kV 1'000x EDX spectrum of TiON thin film no. 1 deposited at 300 W power, 20 Pa pressure, and O:N input ratio of 50:50. Figure zoomed upon the $K_{\alpha}O$ and $K_{\alpha}N$ intensity peaks. A carbon impurity is present between 0.25-0.3keV. . . . .	110
6.10	10 kV 1'000x EDX spectrum of TiON thin film no. 2 deposited at 600 W power, 20 Pa pressure, and O:N input ratio of 50:50. Figure zoomed upon the $K_{\alpha}O$ and $K_{\alpha}N$ intensity peaks. A carbon impurity is present between 0.25-0.3keV. . . . .	110
6.11	10 kV 1'000x EDX spectrum of TiON thin film no. 3 deposited at 600 W power, 15 Pa pressure, and O:N input ratio of 10:90. Figure zoomed upon the $K_{\alpha}O$ and $K_{\alpha}N$ intensity peaks. A carbon impurity is present between 0.25-0.3keV. . . . .	111
6.12	10 kV 1,000x SEM image of part of the deposition area for the TiN thin film deposited at 600 W RF power and 20 Pa pressure. . . . .	112
6.13	10 kV 1'000x EDX spectrum of TiN thin film deposited at 600 W power and 20 Pa pressure. Figure zoomed upon the $K_{\alpha}O$ and $K_{\alpha}N$ intensity peaks. A carbon impurity is present between 0.25-0.3keV. . . . .	113
6.14	XPS spectrum of Ti $2p_{3/2}$ and $2p_{1/2}$ electrons from the titanium oxynitride thin film deposition attempt with O:N input ratio 10:90 (figure repeated from figure 3.24 in section 3.4.5). . . . .	114
6.15	XPS spectrum of O 1s electrons from the titanium oxynitride thin film deposition attempt with O:N input ratio 10:90. . . . .	115
6.16	XPS spectrum of O 1s electrons from the titanium nitride thin film deposition attempt. . . . .	115
6.17	XRD spectrum of TiON thin film deposition attempt with flow ratio O:N = 10:90. The peak at approximately $69^{\circ}$ signifies (100) silicon. . . . .	116
6.18	UV/Vis absorption spectrum for deposited TiON film attempt no. 3 (O:N = 10:90), with absorption profile for plain quartz substrate subtracted. . . . .	117
6.19	UV/Vis absorption spectrum for all deposited titanium compound films, with absorption profile for plain quartz substrate subtracted. . . . .	118

6.20	UV/Vis absorption spectrum for all deposited titanium compound films, with absorption profile for plain quartz substrate subtracted and normalised absorbance, zoomed in on the $\lambda = 190 - 450\text{nm}$ region. . . . .	120
6.21	10 kV 1,000x SEM image of the bottom edge of the deposition area for the $\text{Ta}_2\text{O}_5$ thin film deposited at 600 W RF power and 20 Pa pressure. . . . .	122
6.22	10 kV 1'000x EDX spectrum of the $\text{Ta}_2\text{O}_5$ thin film deposited at 600 W power and 20 Pa pressure. A carbon impurity is present between 0.25-0.3keV. . . . .	122
6.23	XPS spectrum of O 1s electrons from the tantalum oxide thin film deposition attempt. . . . .	123
6.24	10 kV 1,000x SEM image of the bottom edge of the deposition area for the TaON thin film deposited at 600 W RF power and 17 Pa pressure. . . . .	124
6.25	10 kV 1'000x EDX spectrum of the TaON thin film deposited at 600 W power and 17 Pa pressure. Figure zoomed upon the $K_\alpha\text{Ta}$ , $K_\alpha\text{O}$ , and $K_\alpha\text{N}$ intensity peaks. A carbon impurity is present between 0.25-0.3keV. . . . .	124
6.26	XPS spectrum of O 1s electrons from the tantalum oxynitride thin film deposition attempt. The O=/ $-C$ and O=/ $-X$ contributions likely correspond to either carbon impurities or oxidation on the surface, though the intensity in the O=/ $-X$ contribution is too small to accurately specify. . . . .	125
6.27	UV/Vis absorption spectrum for deposited TaON film, with absorption profile for plain quartz substrate subtracted. . . . .	126

# Acknowledgments

It has been a long road to this point. In the four years I have worked on this PhD, I have had many enjoyable and difficult experiences, and changed in many ways. I have had to face unforeseen challenges from start to finish, from dealing with the uncertainty of the COVID-19 pandemic at the start of my PhD in September 2020, to dealing with heavy grief after the sudden passing of my younger brother, Stuart, in August 2023, just before beginning my final year. Though I have persevered until the end, I could not have done so without my family, friends, and colleagues. Consequently, I have many people I wish to thank for their support over the four years of my PhD, as well as the eight years of my time at the University of York.

I would like to begin by expressing my deepest gratitude to my supervisor, Erik Wage-naars. From my first lecturer as an undergraduate eight years ago to my supervisor over the last four years, your unwavering guidance, friendliness, dedication, and patience has been truly invaluable throughout this entire journey. Your commitment to your professional and personal life is unparalleled and inspirational. I am so grateful that you were my supervisor.

I would also like to thank the other academics in the LTP group at the YPI, past and present: James Dedrick who was always willing to lend his consultation (and talk my ear off!); Kari Niemi for his immeasurable wealth of technical knowledge and assistance during the many long and difficult lab days; Andrew Malcolm-Neale for being a friendly and helpful face during both my PhD and MPhys projects; and James Walsh, Andrew Gibson, and Deborah O'Connell for their advice and insight in many LTP areas. Many thanks to my fellow LTP students and friends: Max Kellermann-Stunt and Ryan Magee for the tremendous (and exhausting!) amount of collaborative work on the TALIF diagnostic, and Michael Mo for his support when the three of us started out; and to Ben Harris, Kittawat Poonsawat, Jidchanok Wangkanai, Jaka Olenik, Jaspar Burg, Helen Davies, and Greg Smith for being faces I enjoyed seeing at group meetings each week.

A big thanks to the students and staff from other University of York departments: Jack Bradley and Andy Pratt for their cooperation with the XPS analysis; Jon Barnard for his instruction with the SEM; David Lloyd for the XRD guidance; and Scott Hicks for the UV/Vis training.

I would like to extend my thanks to my friends and colleagues in all areas of the YPI family. Particularly, István Cziegler for his tenacity and encouragement as my MPhys supervisor; and his former PhD students, Steven Thomas and Yorick Enters, for their aid during my MPhys year. Special thanks to Andy Higginbotham for his support as my undergraduate pastoral supervisor. It has been a pleasure to have been part of the YPI community over the last five years, and I will miss everyone's faces as well as the Wednesday pub evenings.

I want to give a huge thanks to all my friends around York, especially the fine folks at PokéSoc and the University of York Concert Band, for bringing boundless joy to my Fridays and Saturdays each week. I *will* be sure to see you all again in the future. Thanks to my undergraduate coursemates and housemates, and my many friends outside York, old and new, home and abroad, for keeping me sane during these last few years and encouraging me to keep doing my best.

Finally, my most heartfelt thanks to my family. To my loving mum and dad, whom I cannot thank enough for their endless loyalty, devotion, and compassion, always allowing me to choose my own path and supporting everything I do. To my grandmother, for her counselling and for helping to make this PhD possible. And last, but not least, to my late brother, Stuart. It pains me greatly to come out of this PhD journey without you with us, but your smile will never be forgotten. I love you and miss you, Stuuie.

As tumultuous as this journey has been, it has given me the opportunity to experience much, and has well and truly shaped the man I am today. I will never forget the support and encouragement from everyone I have met along the way, I will never forget these amazing eight years I have spent at York, and above all else, I will never stop learning.

Thank you, all!

# Declaration

This thesis has not previously been accepted for any degree and is not being concurrently submitted in candidature for any degree other than Doctor of Philosophy of the University of York. This thesis is the result of my own investigations, except where otherwise stated. All other sources are acknowledged by explicit references.

All X-ray photoelectron spectroscopy (XPS) analysis presented in chapters 3 and 5 was performed and interpreted by Mr J. Bradley at the University of York School of Physics, Engineering & Technology.

Computational scripts used in the two-photon absorption laser-induced fluorescence (TALIF) data analysis presented in chapter 5 were developed by Mr M. Kellermann-Stunt at the York Plasma Institute, but all data in this section was obtained, analysed, and interpreted by me.

# Chapter 1

## Introduction

### 1.1 Motivation

Semiconductors are considered the building blocks of modern technology. They can be found in almost every modern digital device in existence, and have one of the widest ranges of applications of any material, including microbatteries, biomaterials, gas sensing, superconductors, and many more [6–10]. They also contribute significantly to many parts of social infrastructure, including the internet, GPS systems, and vehicles such as cars and trains. They are materials with conductivities between that of insulators and conductors, and are able to control the flow of electric current in electronic devices. Many semiconductors exist as thin films, which is the focus of this work. These are tiny materials that range from tens of nanometres to hundreds of microns thick. It is because of their compact size, along with their unique electrical properties, that they have gone further than any other material in shaping the modern digital, interconnected world.

Many of the methods used to manufacture thin films involve plasma-based deposition techniques. Pulsed laser deposition (PLD) is one of the well-established deposition techniques mostly used for deposition of semiconductor thin films. In PLD, a metal compound target, e.g. titanium oxide, is put inside a low-pressure vacuum chamber. A high-powered pulsed laser beam then ablates material from the target, vaporising it into a plasma plume, cooling down as it propagates through the chamber and deposits onto a substrate, forming the thin film. A strength of PLD compared to other methods is it allows for the production of films with complex chemical structure, but the main limitation is it usually requires complex material targets to begin with, due to the method having limited control over the

stoichiometry of the desired thin film.

Metal oxide thin films are of particular interest in many industrial applications, including photoelectrodes which use solar energy to dissociate water molecules into hydrogen and oxygen. The subsequent energy produced from this low-temperature photoelectrochemical reaction is stored in the chemical bond of  $H_2$ , which can be released by reacting the  $H_2$  with pure  $O_2$ , producing water once again. This process allows for cheap and efficient production of hydrogen fuel as a renewable carbon-free energy source [11, 12]. A novel version of PLD for producing metal oxide thin films is plasma-enhanced pulsed laser deposition (PE-PLD) where oxygen in the film comes from a background plasma and the metal comes from a pure metal target, thus allowing for more control over stoichiometry. This has been shown to produce copper and zinc oxide thin films to a reasonable standard [13]. However, PE-PLD is still being researched, with many aspects yet to be understood, including how the background plasma affects the deposition of the thin films. This current lack of understanding makes applications challenging.

Metal oxides such as  $TiO_2$  have been established as the most prevalent materials for thin films applied to photocatalytic processes since 1972, due to their active photocatalytic properties such as their resistance to photo-corrosion, high chemical stability, and non-toxicity [14, 15]. However, the main limitation of these materials is their band gaps typically correspond to radiation which lies in the ultraviolet region, which is only a small fraction of the solar spectrum. This means metal oxides are not as efficient at water splitting as they could be if they were photoactive in the visible range [16].

Metal oxides can be doped with nitrogen to create metal oxynitrides, a new class of materials which have been shown to have band gaps corresponding to visible light, allowing for a promising alternative photocatalytic material to metal oxides [17, 18]. Achieving the precise stoichiometry of metal oxynitrides for thin films remains a challenge.

The research presented in this work extends the possibilities of PE-PLD to metal oxynitrides, particularly  $TiON$  and  $Ta_3O_xN_y$ , due to their promising potential as photoelectrodes for water splitting to achieve a hydrogen economy. In addition to creating metal oxynitride thin films by direct experiment, a hydrodynamic modelling software, POLLUX, is utilised to model laser ablation of different photocatalytic metals, including titanium and tantalum, in the PE-PLD process, in order to investigate the links between material properties and their corresponding plasma plumes. Moreover, an established plasma diagnostic technique, two-

photon absorption laser-induced fluorescence (TALIF) is used to characterise the amount of oxygen and nitrogen plasma content in PE-PLD, in order to produce stoichiometric thin films. The findings from these three investigations will bring us one step closer to producing high-quality oxynitride thin films.

## 1.2 Thesis outline

This thesis comprises the following chapters:

**Chapter 2** gives detailed descriptions of the physics appropriate to this work, including laser ablation of metal and metal compound targets, radio frequency plasmas, photocatalytic thin films, and the current knowledge of the novel plasma-enhanced pulsed deposition technique.

**Chapter 3** specifies the methodology used in producing the results presented in chapters 4, 5, and 6. This includes the details of the models used in the hydrodynamic code POLLUX, and the experimental procedures of the plasma and thin film diagnostic techniques.

**Chapter 4** presents results from modelling the laser ablation of different metals using the 2D hydrodynamic laser ablation code POLLUX.

**Chapter 5** contains results from characterising the atomic densities in a low-pressure  $O_2/N_2$  plasma using the two-photon absorption laser-induced fluorescence diagnostic.

**Chapter 6** provides analysis of the chemical composition and crystalline structure of metal oxide and oxynitride thin films performed by appropriate thin film diagnostics.

**Chapter 7** summarises the work presented in this thesis, providing conclusions as well as suggestions for future work.

## Chapter 2

# Scientific Background

This chapter covers the appropriate background knowledge required for the work presented in this thesis. In addition to an introduction to PE-PLD and its current state of knowledge, it touches on the relevant laser and plasma physics of the process, as well as properties of metal oxide and oxynitride thin films.

### 2.1 Plasma-enhanced pulsed laser deposition

Pulsed laser deposition (PLD) is a renowned method of producing thin films. It was initially developed in 1987 and began commercial use in 1989 [10, 19]. A high-powered pulsed laser beam is incident on a target material inside a vacuum chamber. The laser transfers energy to the target via inverse bremsstrahlung (see section 2.2.2 for details), ablating material from the target surface, and vaporising and ionising the material into a plasma plume. The plume propagates through the chamber, expanding and cooling as it collides with particles within the atmosphere of the chamber in addition to particles within the plume itself before reaching the substrate where it is deposited onto the thin film, as shown in figure 2.1.

The laser-target system is isolated, meaning the plasma plume does not interact with surfaces that may contaminate the film, which is a notable advantage. Parameters such as laser energy, laser wavelength, and pulse width can be varied to control deposition rates. However, those parameters are not independent and cannot easily control the stoichiometry of the desired thin film. For example, CuO and Cu<sub>2</sub>O thin films produced in this way require a CuO or Cu<sub>2</sub>O target respectively, and compound targets are much more experimentally challenging compared to pure element targets. In the case of metal oxide thin films produced

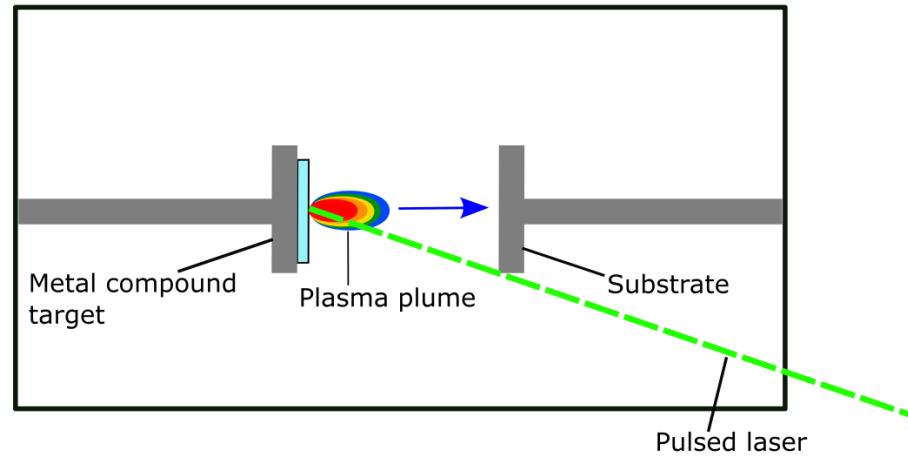


Figure 2.1: Schematic diagram of a typical PLD setup.

by PLD, most of the oxygen comes from the target, but the stoichiometry of the deposited film is not always consistent with the metal oxide target, and the films typically come out lacking in oxygen. To correct this, oxygen gas at a low pressure is commonly inserted into the chamber to improve thin film growth and stoichiometry. An additional caveat is that post-deposition annealing and substrate heating are often needed for depositing high-quality films, requiring additional energy to achieve structures that are desired.

Plasma-enhanced pulsed laser deposition (PE-PLD) has the potential to improve on PLD by using radio-frequency (RF) plasma (see section 2.5 for details) for the non-metal species instead of gas. The idea is that the introduction of this RF plasma allows for much greater flexibility over the materials used in producing the thin film. For example, a TiON thin film can be produced from either a titanium metal target and an oxygen/nitrogen plasma admixture, a titanium oxide target and a nitrogen plasma, or even a titanium nitride target and an oxygen plasma. The independent control of chemical species also allows for finer tuning of the stoichiometry of the desired film, which is a key advantage. The RF plasma used in this research is an inductively coupled plasma (ICP), which will transfer chemical energy to the growing film through surface interactions, meaning the substrate will not require any additional heating or annealing in post-production. Furthermore, it allows for additional

gases to be added into the system such as nitrogen for metal nitride films, opening up the possibilities for an even wider variety of thin films to be produced [20]. This is especially promising for metal oxynitride thin films as nitrogen and oxygen from separate sources can simultaneously contribute to the background plasma.

PE-PLD still has limitations of its own, such as a more expensive and complex setup than standard PLD or other thin film deposition techniques such as sputtering, and the ICP is able to interact with the solid target in addition to the plume, which risks the target becoming contaminated. The background plasma parameters must therefore be carefully controlled in order to prevent or reduce the impact of such contamination. Moreover, PE-PLD is still an active area of research, with many problems yet to be addressed or understood, including the plasma-plume chemistry.

PE-PLD has been performed in the literature in the past, such as in [21] where S-H. Huang et al. deposited ZnO films, albeit using a capacitively-coupled plasma (CCP) (see section 2.5 for details). Their method was shown to deposit thin films 3 times faster than standard PLD, but developed defects in the crystalline structure of the films and required additional oxygen pressure to reduce the defects. Additionally, A. De Giacomo et al. [22] deposited TiO<sub>2</sub> films with a CCP and a pulsed KrF excimer laser at 248 nm. They found that the additional plasma improved the stoichiometry, morphology, and deposition rate of the TiO<sub>2</sub> thin films. However, in both cases, substrate heating and annealing was required. More recently, M. Escalona et al. [23] compared the dynamics of a plasma plume in both PLD and PE-PLD of TiN films. They concluded that PE-PLD increased the background reactivity with the Ti plume, which they expected would improve thin film growth.

At the University of York, S. Rajendiran introduced and demonstrated the potential of PE-PLD in a proof-of-concept study on copper oxide thin films. She modelled the laser ablation of a Cu plasma plume using the hydrodynamic code POLLUX [24,25], and modelled the plasma properties of an inductively-coupled oxygen plasma using the 2D Hybrid code HPEM [26]. She then deposited copper oxide films experimentally in the York Plasma Institute (YPI) Laboratories using Cu metal targets and oxygen H-mode ICPs which varied at pressures between 4-20 Pa. Overall, the experiments were shown to deposit high-quality CuO and Cu<sub>2</sub>O films from a pure target with no substrate heating or post-annealing, and the ICP was able to tune the stoichiometry and crystal structure of the films [27]. D. Meehan built upon this work, using POLLUX to model the laser parameters for PE-PLD, as well

as characterising the behaviour of the laser ablation of both metal and metal oxide targets under conditions used in PE-PLD, in which metal targets were found to ablate in a much more stable manner than oxide compound targets, which exhibited more volatile ablations. Further, he used HPEM and experimental diagnostics to characterise other effects within the PE-PLD process, such as gas temperature and heat transfer to reactor walls; discovering that the temperature in the off-time of plasma pulses returned to room temperature regardless of pressure – an important result which does not limit PE-PLD to only materials of high heat resistance. Finally, he deposited and analysed the structures of a variety of different metal oxide films experimentally in the YPI Laboratories, including ZnO, SiO<sub>2</sub>, and Al<sub>2</sub>O<sub>3</sub>, which are each used in different industrial applications such as electronics and coatings [28].

This work also utilises the PE-PLD setup in the York Plasma Institute (YPI) Laboratories. Figure 2.2 displays a schematic diagram of this setup, including the laser and ICP conditions. The laser used is a Nd:YAG laser, widely used across many industries for its non-invasive nature.

The PE-PLD setup is made up of a chamber containing a low-pressure ICP and PLD system, with a transition metal target and a quartz or silicon substrate both mounted onto a separate holder each parallel to one another inside the chamber. First, a vacuum is established inside the chamber using an Edward nxDS 15i scroll pump, which aims to reduce the pressure in the chamber to below 1.5 Pa. Once that is reached, one or more gases such as oxygen or nitrogen (or both) are fed into the chamber, and a pressure between approximately 5-20 Pa is created by adjusting the flow rate on a mass flow controller (Center Two / Center Three Multi-Channel Controller), which could range between 0.68-14 sccm. Next, a plasma is created using a 13.56 MHz Advanced Energy Cesar RF power supply, matched through a Meidan Pi-type matching network, and water-cooled with a K1 Series cooler. This is connected to a 3-turn copper coil, 14 cm in diameter at the top of the chamber, which is separated from the gas by a 2.54 cm quartz wall. With this coil, along with a grounded, stainless steel, water-cooled electrode (10 cm in diameter) at the bottom of the chamber positioned 4 cm from the coil, a low-temperature plasma was created throughout the chamber. A frequency-doubled, Q-switched, 532 nm Nd:YAG laser beam is then aligned via the use of mirrors and focused by a lens of focal length 50 cm, before entering the chamber through a window with an anti-reflective coating for 532 nm. It is then directed at the metal target at an angle of 45° to the normal, with an unevenly circular focal spot size due

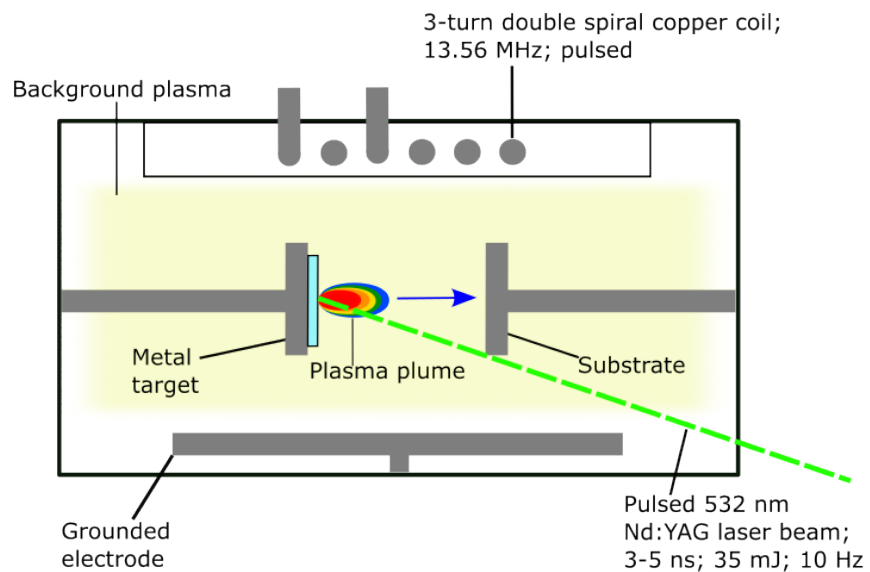


Figure 2.2: Schematic diagram of the PE-PLD setup in the York Plasma Institute Laboratories.

to the angle of incidence (this spot size would be 1 mm in diameter if perfectly circular). The laser ablates material from the surface of the target in 5 ns pulses, vaporising and ionising the material into a plasma plume (not to be confused with background plasma). The plume expands and cools due to collisions from atoms and ions within the plume itself as well as from surrounding particles, altering the plume's kinetics and chemistry. Gaseous material is

then deposited onto the substrate, creating the desired thin film.

## 2.2 Interaction of lasers with solids and plasmas

This section touches on important processes to consider when the laser initially interacts with both the solid target and ablated target material, as well as when the plasma plume interacts with the additional background plasma.

### 2.2.1 Reflection, absorption, and ablation of solid material

Part of the laser's radiation passes through the surface of a solid target, and part of it is reflected off the surface. The amount of light that passes through is dependent on three main factors: target material [29]; target temperature [30]; and the wavelength of the incident laser photons [29, 31]. Photons which are not reflected pass into the material and are absorbed, and the laser intensity drops as the laser propagates deeper into the material, according to the Beer-Lambert Law [32]:

$$I(z) = I_0 e^{-\alpha z} \quad (2.1)$$

where  $I$  is the intensity,  $I_0$  is the initial laser intensity value,  $z$  is the depth of penetration, and  $\alpha$  is the absorption coefficient (i.e. the inverse of the depth of penetration). The absorption coefficient can depend on temperature and wavelength, but it is heavily dependent on the material. Therefore, it is assumed constant here in equation 2.1, and only changes if the material changes. The final penetration depth of light into the material (at which light penetration becomes negligible),  $\delta$ , can be determined from  $\alpha$  according to equation 2.2:

$$\delta = 1/\alpha \quad (2.2)$$

The exponential decay of the intensity is shown schematically in figure 2.3.

The pulse duration of the laser can have significance on the physical processes involved the absorption of energy by the target across the total depth of penetration. In metals, electrons are excited by the laser and become hot, and this heat is subsequently transferred through the lattice via phonons. The time scale for the interaction between these hot electrons and lattice phonons in metal targets (electron-phonon coupling) lies approximately between the order of

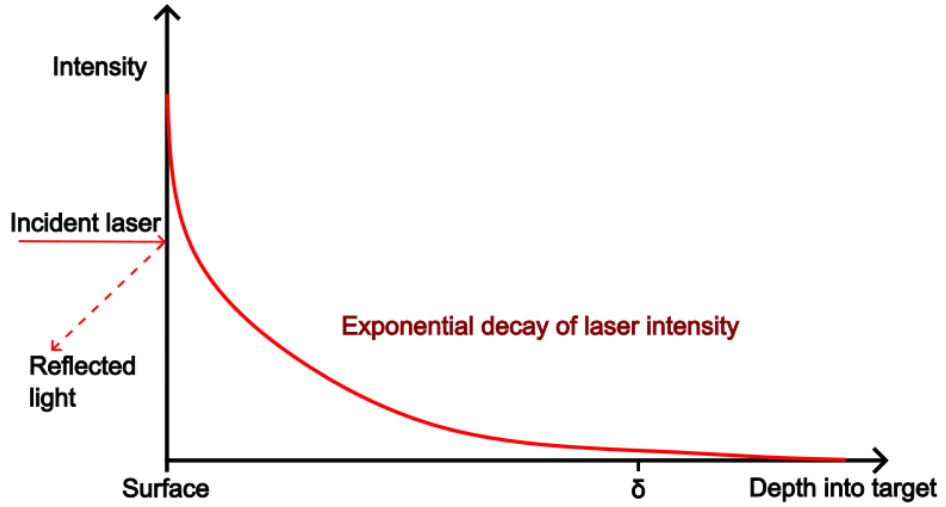


Figure 2.3: Decay of laser intensity during absorption into a solid target.

$10^{-12}$  and  $10^{-10}$  seconds [33]. If the laser used has a pulse length similar to or shorter than this time scale, e.g. picosecond (ps) and femtosecond (fs) lasers, these phonon interactions will be too significant to ignore, and uncommon phase changes such as sublimation are likely to occur in the target with lasers of such pulse lengths. However, lasers used in this work have pulse lengths on the order of nanoseconds (ns), at which the phonon interactions will become greatly overshadowed by other processes. Here, photo-thermal processes usually occur instead, meaning the target will undergo more classical phase changes: melting into a liquid; followed by evaporation into a gas; followed by ionisation into a plasma [33–35].

### 2.2.2 Inverse-Bremsstrahlung absorption

Inverse-Bremsstrahlung (IB) absorption is one of the main absorption mechanisms for most cases of energy coupling of nanosecond lasers into different media. It is prominent in cases in which free electrons in the medium, e.g. metal or plasma, are able to interact with the laser. It occurs when an electron in the Coulomb field of an ion absorbs energy from a photon [36–38]. The IB absorption coefficient is given as:

$$K_{ib} = 8\sqrt{\pi} \left( \frac{e^2}{4\pi\epsilon_0} \right) \frac{4}{3c^2} \frac{Z^2}{m_0^2} n_e n_Z \left( \frac{m_0}{2k_B T} \right)^{1/2} \frac{\pi^2 c^2}{\hbar \omega^3} \left( 1 - \exp\left(-\frac{\hbar\omega}{k_B T}\right) \right) \quad (2.3)$$

where  $e$  is the charge of an electron,  $\epsilon_0$  is the permittivity of free space,  $c$  is the speed of light,  $Z$  is the charge of the ion involved in the coupling,  $m_0$  is the electron rest mass,  $k_B$  is the Boltzmann constant,  $T$  is the electron temperature, and  $\omega$  is the laser frequency [38]. Since the electron is free, it can collide with neighbouring free electrons and nuclei, transmitting energy via heat [28].

The IB absorption coefficient is inversely proportional to the cube of the laser frequency, and is therefore proportional to the cube of the laser wavelength, meaning it is strongly dependent on the laser wavelength. IB is the most prominent form of energy coupling in this intensity range for infra-red and visible lasers, such as the 532nm Nd:YAG laser used in this work.

As the name suggests, IB absorption is the inverse of the bremsstrahlung process, in which an electron radiates electromagnetic energy as it accelerates in the field of an ion [38]. There is a second method of energy coupling of lasers into different media, known as photo-ionisation, which occurs when a photon interacts with an atom or molecule to form an ion [39]. There is also the process of multi-photon ionisation, in which more than one photon is absorbed at a time. However, this is typically observed with shorter wavelength (and thus higher photon energy) lasers, and not so much with the the 532 nm laser in the PE-PLD setup in this work, which typically operates at energies of approximately 2.3 eV, while first ionisation threshold of titanium is 6.821 eV [40]. Thus, although photoionisation does occur when the laser interacts with the solid metal target during the PE-PLD process, it will be dominated by IB absorption, especially in the expanding plume.

## 2.3 Expansion of a plasma plume

This section comprises two stages considered in this work when a plasma plume ablated from a solid target expands and interacts with its surroundings, as well as the behaviour of species within the plasma plume during this part of the process.

### 2.3.1 Plasma plume interactions with a vacuum background

Plasma plume expansion into a vacuum can be described as an adiabatic expansion, with no loss of energy or material to the surroundings. The model proposed by Anismov et al. [41] describes how the velocity, density, and entropy of the expanding plume develops in a vacuum

over time, according to the following three gas dynamic equations:

$$\begin{aligned}\frac{\partial \rho}{\partial t} + \nabla(\rho v) &= 0 \\ \frac{\partial v}{\partial t} + v \nabla(v) + \frac{1}{\rho} \nabla p &= 0 \\ \frac{\partial S}{\partial t} + v \nabla(S) &= 0\end{aligned}\tag{2.4}$$

In the above three equations,  $\rho$ ,  $p$ ,  $v$ , and  $S$  are the density, pressure, velocity, and entropy per unit mass, respectively. The plume is modelled as an ideal gas with a constant adiabatic index  $\gamma = c_p/c_v = 5/3$  (where  $c_p$  and  $c_v$  are the specific heat coefficients at constant pressure and volume respectively). Although mass and energy are assumed to not be lost, a more complex model is required to observe whether temperature and entropy are also constant, or are affected by processes like collisions or recombinations of ions/electrons. The Stapleton model [42] assumes the initial plume conditions to be either isothermal or isentropic, and the following ordinary differential equation controls the adiabatic expansion of the plume:

$$X \frac{d^2 X}{dt^2} = Y \frac{d^2 Y}{dt^2} = Z \frac{d^2 Z}{dt^2} = \omega \frac{E}{M} \left( \frac{X_0 Y_0 Z_0}{XYZ} \right)^{\gamma-1}\tag{2.5}$$

where  $M$  is the plume total mass,  $E$  is the total plume energy,  $\omega$  is equal to  $(\gamma - 1)$  for an isothermal expansion, and equal to  $(5\gamma - 3)$  for isentropic expansion.  $X$ ,  $Y$ , and  $Z$  give the plume dimensions at time  $t$ , and  $X_0$ ,  $Y_0$ , and  $Z_0$  are the respective plume dimensions at time  $t = 0$ .

### 2.3.2 Plasma plume interactions with a non-vacuum background

Interactions between the plume and any non-vacuum background can be described by both physical conditions affecting the plume, and chemical reactions that occur between the plume and the background.

Harilal et al. observed the expansion of an aluminium plume in different background pressures of argon. At the lower pressure they measured with (20 Pa, the plume travels and expands much faster with the leading edge of the plume being much denser compared to the plume in the higher argon pressure of 1333 Pa, which was less dense at the leading edge and more closely confined [42]. This effect is caused by physical collisions between the plasma plume and background, with the denser, higher pressure case having a greater number of

collisions and therefore reducing the plume's velocity.

Orsel et al. ablated a plasma plume from a  $\text{LaAlO}_2$  target within an oxygen atmosphere. They showed via laser-induced fluorescence (LIF) that chemical reactions between the plume and the background can occur, affecting the chemical composition of the plume, and is more prominent around the edge of the plume where species will be in direct contact with the background [43].

For standard PLD, factors that must be considered to deposit films of desired stoichiometry include the control of shape and velocity by background pressures, and the composition of gases to chemically react with the plume [39]. PE-PLD uses chemically reactive species generated by background plasmas rather than gases to greatly improve thin film stoichiometry.

## 2.4 Deposition of plasma material onto a substrate

If an incident particle on a substrate has too much kinetic energy, either from being an element with high atomic mass, or having a large velocity, then sputtering of substrate atoms can occur. This is used in sputtering and etching processes, but is not ideal for thin film growth.

In its proof of concept [27], PE-PLD was classified as non-epitaxial, similar to PLD. This means the film growth and structure is *not* determined by the structure of the underlying substrate [44]. This is because the ablated plume has sufficiently high densities for particles incident onto the substrate to begin depositing particles and forming clusters, before diffusion onto lattice sites of the substrate is a dominant effect. Additionally, plume particles with higher kinetic energy have been shown to greatly improve thin film growth [45].

Atoms begin to form groups, or 'islands,' on the surface of the substrate. Once large enough, the islands coalesce with each other, forming larger grains. At this stage, enough atoms are present for diffusion into a crystal lattice forming a crystalline structure of the film, in which the atoms are arranged in an ordered lattice. The grains may enlarge and roughen, but each grain is able to form different crystalline structures, leading to a polycrystalline film. This type of thin film growth is known as 'island growth,' and is illustrated in figure 2.4. The substrate and film layers are not as sharply defined in practice as the figure would suggest. There is a 'transition' region between the two, which arises from the bonds formed

between the film and the substrate, which is not necessarily consistent in structure with the film. The transition layer's thickness indicates the difference between the lattice size of the substrate and the film [46].

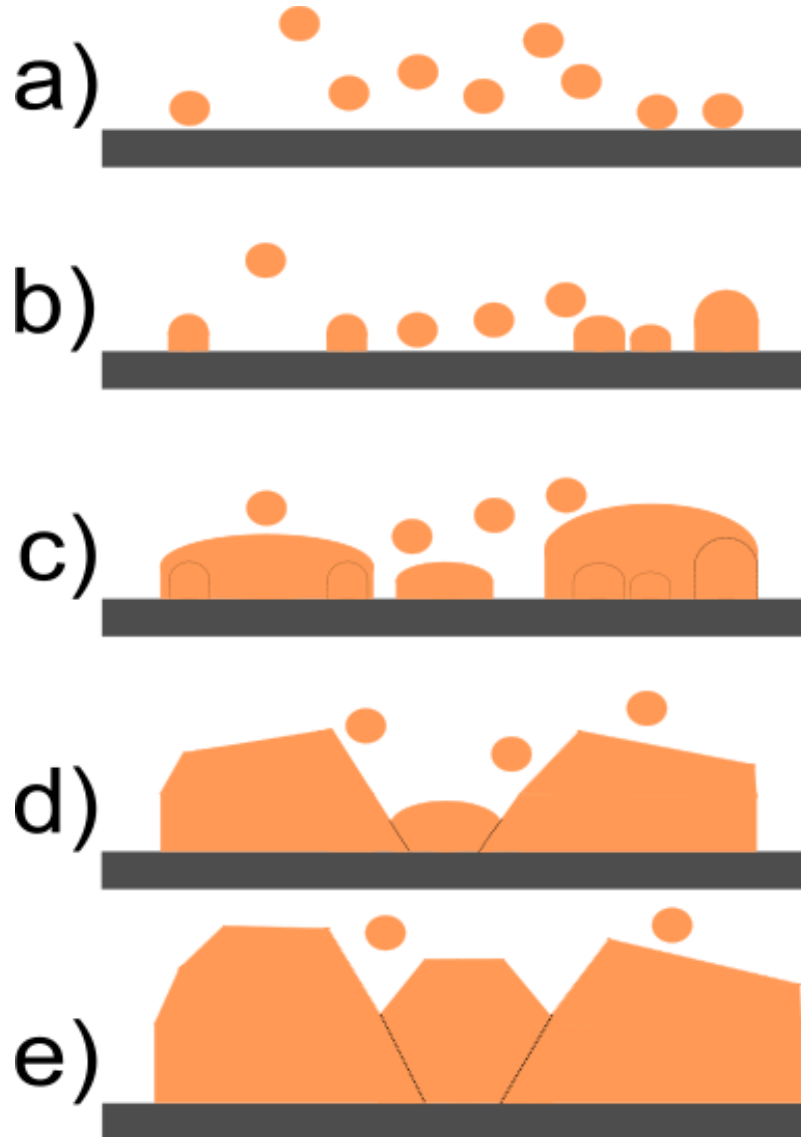


Figure 2.4: Illustration of fundamental process deposition onto a substrate and film growth. Steps shown are: a) nucleation; b) island growth; c) island coalescence and grain formation; d) island coarsening and formation of polycrystalline grains; e) further development of grains and film growth.

Non-epitaxial growth techniques like PLD have little control over grain structure and transition layer thickness during film growth, and require annealing after the film has been produced, which can change the film grain structure and phase, e.g. can turn amorphous  $\text{TiO}_2$  films into anatase, or even rutile at higher temperatures. Annealing can also affect

the film's optical properties, which can be useful depending on its desired application [47]. Epitaxial techniques, such as molecular beam epitaxy [48], lack control as well, but also use controlled 'seeding' layers, which have pre-determined lattice constants to influence grains grown during deposition [46, 49].

## 2.5 Radio-frequency plasmas

In this work, the background plasma the plume interacts with is a radio-frequency (RF) plasma. RF plasmas work by exciting electrons within a gas by an external electric field at an RF frequency, typically 13.56 MHz and its harmonics, which are frequencies approved internationally for industrial, scientific, and medical (ISM) purposes. Ions are not accelerated due to greater mass and thus lower mobility. The result is a plasma with high electron temperatures and lower ion temperatures, known as a non-equilibrium plasma, or low-temperature plasma (LTP) [50]. The free electrons are able to undergo collisions and chemical reactions with the heavier species within the plasma, but the number of collisions is not sufficient to redistribute their energy among them, especially in a low-pressure environment. Thus, thermal equilibrium is never achieved in this scenario, causing the plasma to remain an LTP. Due to the free electrons' ability to react with the heavier species, RF plasmas are usually found to comprise a diverse range of chemically reactive species. As such, they have an expansive range of applications in industry, including medicine, jet propulsion, microelectronics, and, of course, thin films.

The plasma sheath (or Debye sheath) is a region of net-positive charge between the plasma and the walls of the container housing it. This phenomenon is present in almost every type of plasma, but the sheath is an important feature for RF plasmas in particular. Once the plasma is formed with free electrons and heavy ions, both species are free to leave the main bulk of the plasma. However, the electrons escape first, due to their much lighter mass and greater velocity, and as such, negative charge is built up on the walls of the container. This leads to the repulsion of electrons that remain within, and the attraction of the positive ions. The result is a region of positive charge surrounding the plasma bulk and electrons enclosed. The thickness of the sheath,  $s$ , is given by equation 2.6 [50]:

$$s = \sqrt{\frac{2eV_0}{k_b T_e}} \cdot \lambda_d \quad (2.6)$$

where  $e$  is the charge of an electron,  $V_0$  is the voltage drop across the sheath,  $k_B$  is the Boltzmann constant,  $T_e$  the electron temperature, and  $\lambda_d$  is the Debye length, given in equation 2.7:

$$\lambda_d = \sqrt{\frac{\epsilon_0 k_B T_e}{n_e e^2}} \quad (2.7)$$

where  $\epsilon_0$  is the permittivity of free space, and  $n_e$  is the electron density. The Debye length is the length at which electric fields in the plasma screen out the electrons in the plasma bulk. Plasmas with higher electron density will have a much shorter Debye length, and therefore a smaller sheath thickness. The Debye length and sheath thickness will play an important factor depending on the desired application of the plasma, and the method used to generate the plasma. This will be discussed briefly in the next subsection.

### 2.5.1 Capacitively and inductively coupled plasmas

There are two main methods to generate RF plasmas, whose schematics can both be seen in figure 2.5. A capacitively-coupled plasma (CCP) is a plasma formed when a gas is fed into a chamber with two electrodes; one being grounded and the other being powered by an RF generator. An electric field is formed between the two electrodes, permeating the gas and exciting the electrons, forming a plasma in which ions either accelerate towards or away from the powered electrode, depending on phase of the voltage [51]. CCPs are often used in applications in which a surface is roughened by the reactive gas species in the plasma, or the sputtering of atoms from the surface [52].

An inductively-coupled plasma (ICP) also uses a grounded electrode, but instead of a powered electrode, it uses a planar coil external to the plasma volume connected to the RF power generator. The key distinction of an ICP is that the applied power causes the current from the coils to be sufficiently high enough to induce an electron current within the plasma, resulting in much higher plasma densities compared to CCPs. ICPs have two modes of operation: E-mode, in which the plasma is used at relatively lower powers and pressures, resulting in plasmas with dimmer visual appearances and relatively lower densities; and H-mode, in which a relatively higher power is applied to the plasmas, initiating a magnetic field which leads to the induced electron current mentioned earlier. With E-mode, the relatively lower power results in a potential difference (and subsequently an electric field) between the

spiral coil and grounded electrode, generating the plasma in a similar way to a CCP.

An ICP is used in this work due to its ability to create plasmas of high density in H-mode, which can benefit thin film growth. Additionally, since power in an ICP is transmitted via magnetic coils and not a powered plate electrode, there will be much smaller plasma sheaths, leading to significantly less ion bombardment to the walls and other surfaces within the chamber, subsequently resulting in a lack of unwanted etching of the deposited thin film.

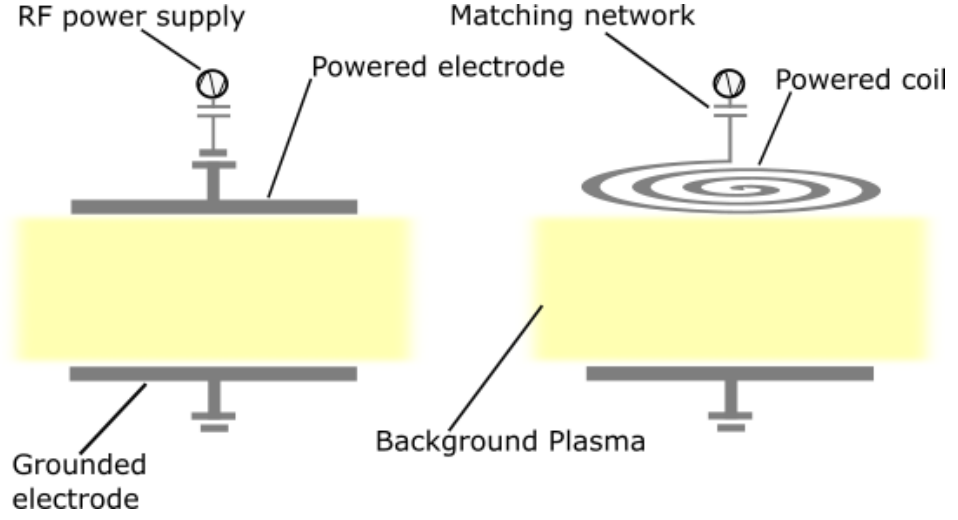


Figure 2.5: Standard configuration for low pressure RF plasma reactors. Left: CCP; Right: ICP.

## 2.6 Equilibrium regimes

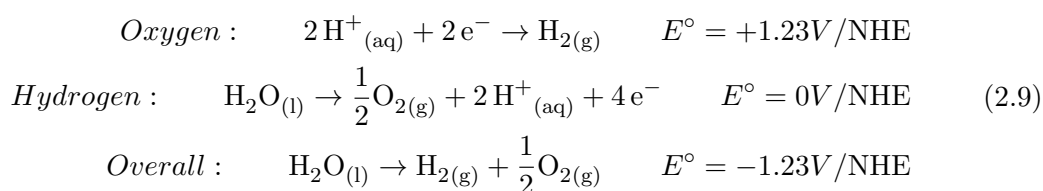
Unlike RF plasmas, the temperatures of electrons and heavier species in laser-produced plasmas can attain a state of equilibrium if they are dense enough for sufficient collisions to occur between each other. Plasmas such as these are said to be in local thermal equilibrium (LTE) [53]. The condition required to meet LTE is defined by the McWhirter criterion:

$$n_e > 1.6 \times 10^{12} T^{1/2} (\Delta E_{ij})^3 \quad (2.8)$$

where  $n_e$  denotes the electron density in  $\text{cm}^{-3}$ ,  $T$  is the temperature of the system in K, and  $\Delta E_{ij}$  is the difference in energy between states  $i$  and  $j$  [54].

## 2.7 Photocatalytic thin films

This section details the thin films of interest in this research. Photocatalytic thin films act as catalysts in a photoelectrochemical reaction used to split water molecules into hydrogen and oxygen, by absorbing energy via sunlight. The mechanism for photocatalytic water splitting is outlined in 2.9:



where NHE is the Normal Hydrogen Electrode, a reference electrode used for determining cell potentials on all half-cell potential reactions. [55]. Since this method for producing hydrogen requires only sunlight, water, and photocatalytic thin films, it allows for a clean, carbon-free method of producing hydrogen fuel, with one of the lowest emission levels of any method of energy production. Currently, this method has low energy efficiency and high cost per unit, but since only sunlight is required, it is predicted to become a more favoured method with the advancement of technology [56]. The materials currently being researched for photocatalysis include metal oxides, and more recently, metal oxynitrides.

### 2.7.1 Metal oxide thin films

The photocatalytic properties of metal oxides have been intensively researched in the literature over the past few decades. Established materials for photocatalysis in industry include  $\text{TiO}_2$  and  $\text{ZnO}$  as the materials are abundant, cheap, and easy to produce in addition to being resistant to photo-corrosion. However, their band gaps are wide enough such that they lie in the ultraviolet range at approximately 3.1 eV each, limiting their use in the visible region. Some metal oxides, including strontium titanate ( $\text{SrTiO}_3$ ), which has similar photocatalytic properties to  $\text{TiO}_2$ , have even wider band gaps, making them less favourable for water splitting using sunlight. Some other metal oxides such as  $\text{CuO}$  and  $\text{Cu}_2\text{O}$  have smaller band gaps of 1.2 eV and 2.1 eV respectively, but are less efficient at photocatalysis compared to  $\text{TiO}_2$ .

In 2015, H. Ahmad et al. [57] published an extensive review of potential photocatalytic

materials for water splitting and have given particular attention to how  $\text{TiO}_2$  can be modified to become more efficient at photocatalysis, including depositing additional metals [58, 59], coupling with carbon nanomaterials or binary composites [60–65], modifying surface particles with adsorbants [66, 67], inorganic dyes [68, 69], or non-metallic elements [70, 71]. Among such materials were metal oxynitrides [72].

### 2.7.2 Metal oxynitride thin films

Metal oxynitrides are novel materials which are currently being researched for their promising potential as photocatalysts. Like metal oxides, they are corrosion-resistant, conduct electricity well, and are composed of abundant elements [72]. In addition, they benefit from the lower electronegativity of nitrogen with respect to oxygen, resulting in a smaller band gap compared to their oxide counterparts. According to A. Fuertes [16], the absorption edge shifts from 4 eV (UV) in  $\text{Ta}_2\text{O}_5$  to 1.8 eV (visible) in TaON, and a similar absorption edge shift occurs between  $\text{TiO}_2$  and TiON. In 2002, Hitoki et al. [1] compared the absorption edge of TaON with  $\text{Ta}_2\text{O}_5$  and produced a diffusive reflectance spectra of the two materials as seen in figure 2.6. The reflectance spectra showed that the absorption edge of TaON was located at approximately 500 nm compared to  $\text{Ta}_2\text{O}_5$ , which had an absorption edge of approximately 300 nm, which lies outside the visible range. The authors did, however, note that the TaON sample they prepared for the experiment was nonstoichiometric, indicating an area for improvement in future work.

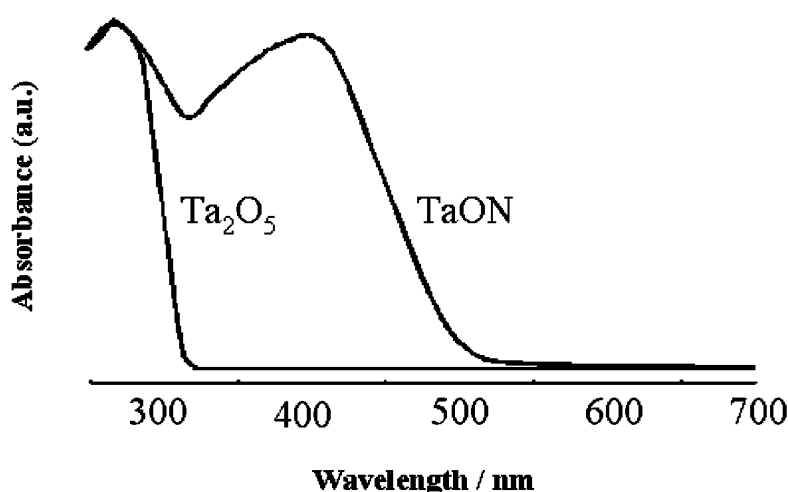


Figure 2.6: UV-visible diffuse reflectance spectra of TaON and  $\text{Ta}_2\text{O}_5$  taken from Hitoki et al. [1].

PE-PLD of titanium oxynitride thin films has been attempted in previous literature, but to little success, due to the difficulty to achieve the correct stoichiometry. M. Yamaguchi et al. attempted to make titanium oxynitrides using a sintered  $\text{TiO}_2$  target and a nitrogen plasma beam bombarding the substrate, which in turn required heating to  $400^\circ\text{C}$ . They expected the nitrogen content in the produced thin film could be controlled by varying the emission current of the nitrogen plasma particles, increasing composition from  $\text{TiO}_{1.16}\text{N}_{0.276}$  to  $\text{TiO}_{0.362}\text{N}_{0.818}$  [73]. Whilst the material was able to absorb some visible light well, there were a few caveats, such as the substrate heating requirements, the fact that a metal oxide target had to be prepared rather than having separate sources for the titanium and oxygen, and most importantly, the nitrogen ion beam having the potential to contaminate the target.

Additionally, N. Mucha et al. produced titanium oxynitride using PLD [74]. The setup consisted of a 248 nm KrF laser ablating a TiN target, background oxygen gas at different pressures (i.e. no background plasma), and indium tin oxide (ITO)-coated glass substrates which required heating to  $400^\circ\text{C}$ . The composition of the thin films produced was found to be  $\text{TiO}_{0.72}\text{N}_{0.42}$  and showed almost no signs of varying. The measured band gap of the thin films was between 1.60 eV and 1.64 eV, which lies comfortably in the visible range.

## Chapter 3

# Methodology

This chapter presents detailed descriptions of all the apparatus used throughout this work, including the PE-PLD laboratory setup; the numerical hydrodynamic code, POLLUX, used to model the laser ablation of metal targets; the plasma diagnostic technique, TALIF, used to characterise background plasma species in PE-PLD; and the various thin film diagnostics used to identify the properties of deposited thin films.

### 3.1 Experimental setup

Figure 3.1 contains a schematic of the complete PE-PLD setup in the York Plasma Institute Laboratories. As seen in figure 2.2, the deposition process takes place in a 6-way-cross vacuum chamber approximately 25 litres in effective volume (i.e. the maximum volume available for gas to take up). A vacuum is attained by two pumps: a scroll pump (Edwards nxDS 15i) used to sustain a base pressure of 1.5 Pa; and a turbo pump (Pfeiffer TPU 170) used to reduce the pressure even further, as low as  $5.6 \times 10^{-6}$  Pa. Oxygen and nitrogen gas are delivered to the chamber via mass flow controllers (MKS Instruments), and the pressure is varied by changing the flow rate between 1-20 sccm (standard cubic centimetres per minute). A needle valve is used to throttle the gas pumping line. This is so the pressure in the system can be controlled by varying the incoming gas flow rate.

Once the desired flow rate is established, an ICP is generated using a 13.56 MHz RF power supply (Advanced Energy Cesar 1330), which feeds power to a 3-turn double-spiral copper coil on the top side of the chamber, protected from the gas with a 2.54 cm quartz plate. The RF can produce power of up to 1 kW through a Pi-type impedance matching

network (Meidan), and the E-H mode transitions for both oxygen and nitrogen plasma species in this work lie at approximately 370 W. The vacuum chamber is based on the Gaseous Electronics Conference (GEC) reference cell, a device recognised within the global community for easy comparison between experiments, including different experiments within this thesis (see section 3.3) [75]. A GEC and an Advanced Energy Cesar 1330 RF power supply are also used to create the plasmas used in the TALIF diagnostic work presented in this thesis (see section 3.3 and results chapter 5), but the chamber pressure in that setup was achieved with a throttle valve instead of a needle valve, and the plasma was generated with an automatic matching network, as opposed to a manual matching network with the PE-PLD setup.

The laser used in the apparatus is a Continuum Minilite laser. This is a Q-switched, frequency-doubled Nd:YAG laser operating at 532 nm, with a pulse length of 5 ns and total beam energy of 35 mJ per pulse, and a repetition rate of 10 Hz. The laser is aligned with the use of mirrors, and focused with a lens of focal length 50 cm, entering the chamber through a window with a designated anti-reflective coating for 532 nm, and arriving at the target surface at an angle of  $45^\circ$  to the normal. This angle offset causes the focal spot of the laser on the target surface to be slightly elliptical in shape. If it were perfectly circular, its diameter would be 1 mm, but this is not its smallest possible size. In the interest of increasing the amount of material ablated per shot, it was intentionally made slightly larger than the minimum, hence 1 mm.

All components within the setup are controlled by a digital delay generator (DDG) from Stanford Instruments. First, the RF generator is powered on, producing the ICP. This is pulsed to optimise the power input during the time the plasma is active, and to reduce the overall heating of the setup. The plasma pulse duration is set to 10 ms. 5 ms into the plasma pulse, the flashlamp is powered on for 10  $\mu$ s, generating gain within the lasing medium. 170  $\mu$ s after the flashlamp is powered on, the gain reaches its maximum, at which point the Q-switch is powered on, causing laser emission and ablation of target material into a plasma plume. The plume propagates through the chamber, reaching the substrate approximately 4 cm from the target. The time taken for material to travel from the target to the substrate has been found to be approximately 2 ms [27]. After the 10 ms plasma pulse, no power is applied to the system for 90 ms in order to be consistent with the laser repetition rate of 10 Hz. Once those 90 ms expire, the cycle begins again, giving a duty cycle of 10%.

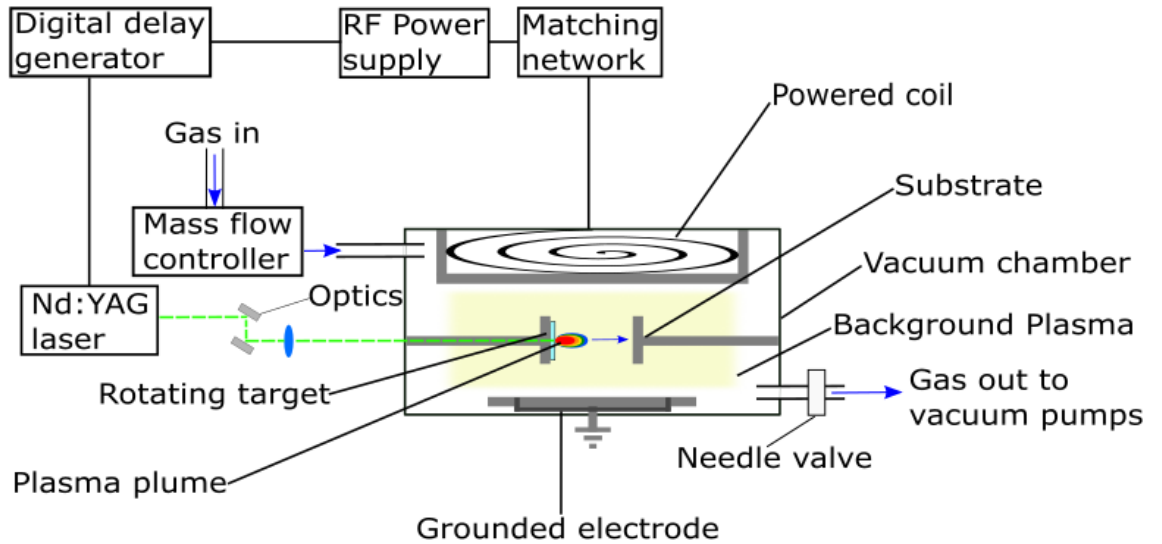


Figure 3.1: Schematic diagram of the PE-PLD apparatus in the York Plasma Institute Laboratories.

Metal targets of 99% purity were used: square titanium targets, which were 1 mm in thickness and 2.54 cm in both length and width; and circular tantalum targets, which were 4 mm in thickness and 2.3 cm in diameter. Both materials were from Testbourne Ltd. The targets were held within the chamber between the two electrodes and secured onto a manually rotatable stage, which could be controlled from outside the chamber. Substrates were fixed in place in a similar way to the metal targets, albeit on a stationary stage with a window of 2.54 cm square dimensions on the opposite flange to the target holder. The substrate holder was also water cooled and grounded to let out charge accumulated onto the substrate during deposition from ionisation. There were two key substrates used in this work: quartz ( $\text{SiO}_2$ ) and silicon (Si); sometimes both at once, in this case, a small silicon shard was attached to a larger quartz disc via carbon tape, and positioned within the window such that half of what was seen in the window was quartz, and the other half was silicon, as shown in figure 3.2. Both substrates were used at once to ensure the same deposited thin film could be used with all thin film diagnostics of interest – only the quartz substrates

were compatible with UV/Vis spectroscopy, and only the silicon substrates were compatible with the X-ray diffraction, EDX, and XPS diagnostics. Before entering the chamber, the targets and substrates were cleaned with isopropanol to remove potential impurities from the surface. An example of a thin film deposited onto both substrates is shown in figure 3.3.

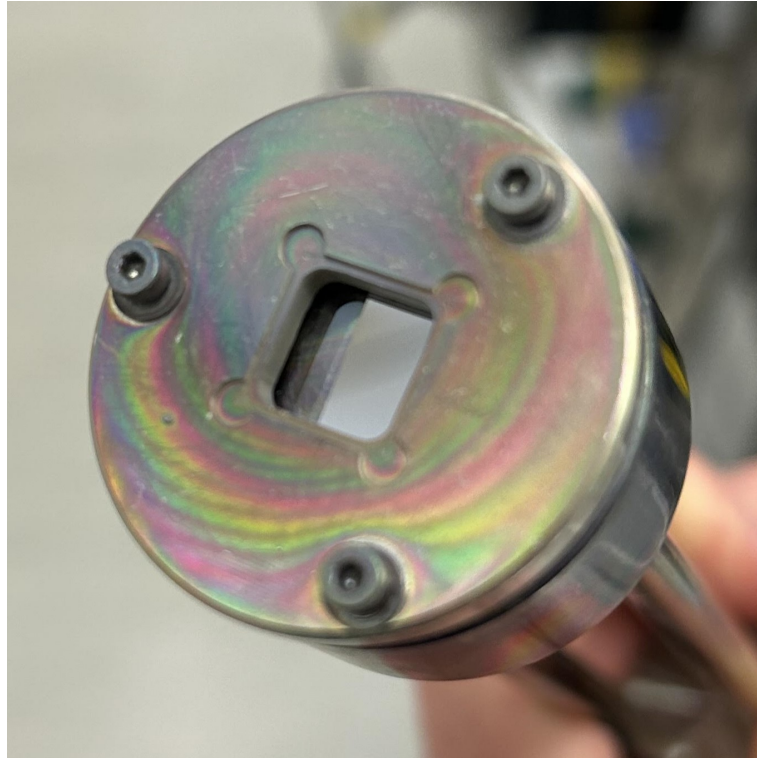


Figure 3.2: Photograph of substrate holder with a quartz and silicon hybrid substrate seen in the holder window. A small silicon shard is attached to a quartz disc.

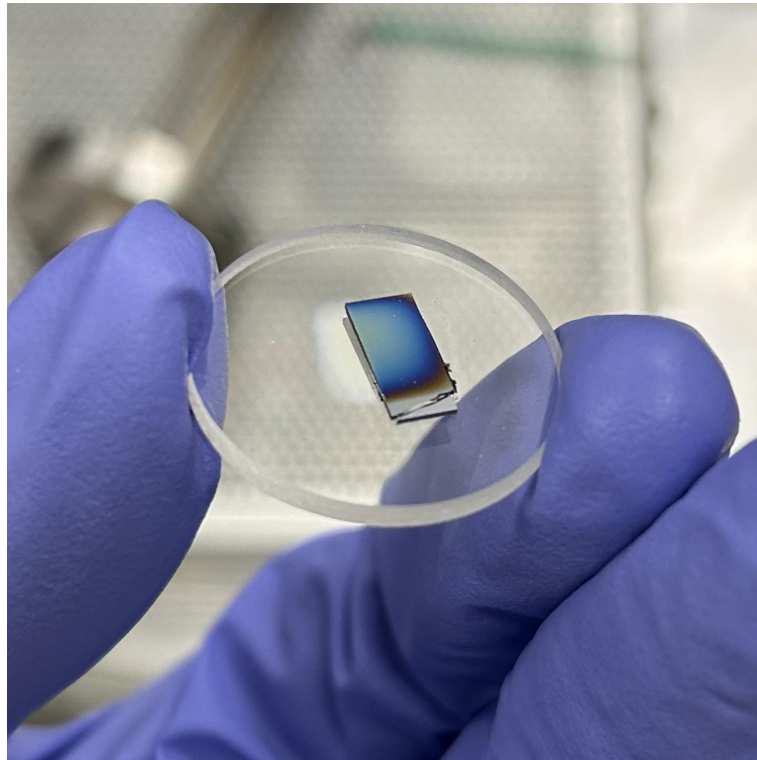


Figure 3.3: Photograph of a TiON thin film deposited onto a quartz/silicon hybrid substrate.

## 3.2 POLLUX model

The POLLUX code is used in chapter 4 of this work to model the laser ablation processes in PE-PLD. It is a 2D hydrodynamic code developed by G.J. Pert et al. [76–79] to model pulsed nanosecond laser ablation and the evolution of a plasma plume as it expands and travels over time. In the past, it has been used to investigate the ablation of different metal plasma plumes using lasers of different wavelength [52, 80, 81]. Laser interaction with the material target and laser interaction with the subsequent plasma plume are both included in POLLUX. A summary of the algorithm of the code in its latest version can be seen in figure 3.4.

### 3.2.1 Mesh

To model mass transport, POLLUX solves the three first-order differential equations of hydrodynamic flow by applying the flux corrected transport (FCT) algorithm by J.P. Boris and D.L. Book [82]. Calculations assume azimuthal (cylindrical) symmetry around the  $z$ -axis with the target and region above the target surface represented by a 2D  $(z, r)$  Eulerian mesh,

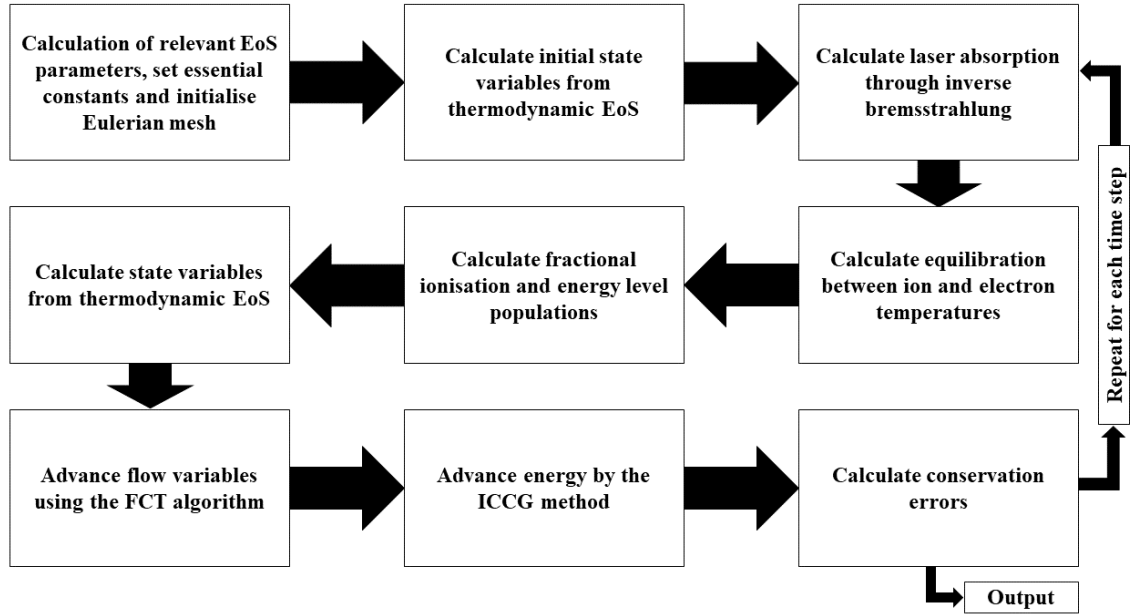


Figure 3.4: Flowchart summarising the POLLUX algorithm.

where  $z$  defines the axis along the target surface normal, and  $r$  defines the radial coordinate orthogonal to  $z$ . The laser pulse is modelled as a Gaussian spatial and temporal profile in which the full-width at half maximum (FWHM) of the beam diameter and pulse duration can be controlled by the user.

### 3.2.2 Equation of State

POLLUX simulates laser-target interactions, including the phase changes of the target during the laser ablation, using two models: The Chart-D equation of state (EoS) developed at Sandia National Laboratories [83] models the nuclear and thermodynamic terms; and the Thomas-Fermi model [84] handles electronic terms, including ionisation within the plume. Finally, energy transport is handled using the Incomplete Cholesky-Conjugate Gradient (ICCG) method [85].

The Chart-D EoS requires a set of input parameters as shown in table 3.1 for the elements investigated in this work. The parameters for Al, Au, Zn and Cu are taken from the original Chart-D database. For Ta and Ti, the parameters are found in the literature.

Table 3.1: Constructed tabular Chart-D EoS for Al, Au, Zn, Cu, Ti and Ta.

<b>Chart-D Variable</b>	<b>Aluminium, Al</b>	<b>Gold, Au</b>	<b>Zinc, Zn</b>	<b>Copper, Cu</b>	<b>Titanium, Ti</b>	<b>Tantalum, Ta</b>
Mass density (g cm <sup>-3</sup> )	2.70 [86]	19.3 [86]	7.140 [86]	8.940 [86]	4.506 [86]	16.4 [86]
Bulk modulus (Barye)	$7.03 \times 10^{11}$ [86]	$2.17 \times 10^{12}$ [86]	$7.2 \times 10^{11}$ [86]	$1.37 \times 10^{12}$ [86]	$1.14 \times 10^{12}$ [87]	$1.91 \times 10^{12}$ [88]
Gruneisen coefficient	2.06 [83]	3.054 [83]	1.390 [83]	2.020 [83]	1.184 [89]	1.59 [90]
Debye temperature (eV)	$3.69 \times 10^{-2}$ [91]	$1.47 \times 10^{-2}$ [91]	$4.40 \times 10^{-2}$ [91]	$5.03 \times 10^{-2}$ [91]	$3.62 \times 10^{-2}$ [91]	$3.45 \times 10^{-2}$ [91]
Enthalpy of sublimation (ergs g <sup>-1</sup> )	$1.22 \times 10^{11}$ [92]	$1.87 \times 10^{10}$ [93]	$1.99 \times 10^{10}$ [94]	$5.3 \times 10^{10}$ [95]	$9.87 \times 10^{10}$ [96]	$4.32 \times 10^{10}$ [97]
Melting temperature (eV)	$1.17 \times 10^{-1}$ [86]	$1.15 \times 10^{-1}$ [86]	$5.97 \times 10^{-2}$ [86]	$1.17 \times 10^{-1}$ [86]	$1.68 \times 10^{-1}$ [86]	$2.84 \times 10^{-1}$ [86]
Thermal conductivity coefficient (ergs cm <sup>-1</sup> eV <sup>-1</sup> )	$2.73 \times 10^{11}$ [98]	$3.71 \times 10^{11}$ [98]	$1.35 \times 10^{11}$ [98]	$4.65 \times 10^{11}$ [98]	$2.55 \times 10^{10}$ [98]	$1.97 \times 10^{10}$ [98]
Atomic number	13	79	30	29	22	73

### 3.2.3 Energy absorption

The metal target absorbs laser energy via inverse Bremsstrahlung, as outlined in 2.2.2. The method the POLLUX code uses to calculate inverse bremsstrahlung is outlined by G.J. Pert

in [79]. The inverse bremsstrahlung coefficient,  $\mu$ , is given by:

$$\mu = b\rho^2 t^{-3/2} \quad (3.1)$$

where  $\rho$  is the mass density of the element or material,  $t$  is the temperature of the plasma plume, and  $b$  is an additional parameter dependent on other laser and material parameters. For the particular case of inverse bremsstrahlung in a plasma:

$$b = (3 \times 10^{36}) \left( \frac{\alpha Z_i}{A} \right)^{3/2} \frac{\alpha Z_i^3}{A^2} \lambda^2 \ln \Lambda' \quad (3.2)$$

where  $\lambda$  is the laser wavelength,  $Z_i$  and  $A$  are the ion charge and mass numbers respectively,  $\alpha = 1 + T_i/Z_i T_e$  is the equilibration factor, and  $\ln \Lambda'$  denotes the Coulomb logarithm for transport as defined in [24, 25].

### 3.2.4 Ion and electron temperatures

As seen in figure 3.4, once the IB coefficient is calculated, the next step is to calculate the equilibration between ion and electron temperatures. The Thomas-Fermi model, which deals with the electronic terms and ionisation within the plume, restricts the plasma plume in POLLUX to LTE due to boundary conditions within the model requiring sufficiently high electron densities to create a sufficient electric potential [99], which could be inappropriate for some plume conditions, especially for long expansion times and expansion into a vacuum. However, given the short timescales ( $\leq 100$  ns) and expansion of the plume into a background gas, LTE will be a reasonable assumption for this work [53, 100]. To equilibrate the ion and electron temperatures, the Spitzer-Härm model is used [101]. This model characterises the effect that electron-ion collisions have on the electrical conductivity of a plasma. This electrical conductivity is known as the Spitzer-Härm conductivity,  $\sigma_{SH}$ , and its relationship with the frequency of electron-ion collisions,  $\nu_{ei}$ , is described in equation 3.3:

$$\sigma_{SH} = 3 \frac{\sqrt{\pi}}{2} \frac{e^2 n}{m_e \nu_{ei}} \quad (3.3)$$

where  $e$  is the charge of an electron,  $n$  is the number density of species within the plasma, and  $m_e$  is the electron mass.

### 3.2.5 Mass transport and the FCT model

The next stage of the POLLUX algorithm is the transport of mass. As mentioned in section 3.2.1, this involves two different techniques: one based in hydrodynamics; the other involving the flux corrected transport model [82].

First, there are several hydrodynamic equations to be solved, including fluid velocity, momentum, and energy equations. A key assumption made is there must be a continuity of mass and energy, as illustrated in equation 3.4. These, along with the other hydrodynamic equations given in [82] are Euler equations, as POLLUX models the laser-ablated plasma plume as an Eulerian fluid.

$$\begin{aligned} \frac{\partial m}{\partial t} + \frac{\partial}{\partial z}(mv) &= 0 \\ \rho_0 &= \frac{m}{XY} \end{aligned} \tag{3.4}$$

Here,  $X, Y$  are the total distance in the respective  $X$  and  $Y$  planes,  $z$  denotes a small change in the  $Z$  plane,  $m$  is the unit mass contained within the volume caused by  $z$ , and  $\rho_0$  us the the initial mass density of the system.

In his work in 1983, G. Pert outlined the hydrodynamic equations of motion, momentum, and energy conservation to be solved [102]. Though these equations provide a means of calculating velocities and transport of mass in POLLUX, they can only determine how fast each cell of density is travelling, and cannot provide a means of quantifying the movement of variables between neighbouring cells. The solution to this is the second technique, utilising the Flux Corrected Transport (FCT) model, created by Boris and Book. Many versions of the FCT model exist in literature and other work, but the one in this work is the SHASTA (SHarp And Smooth Transport Algorithm) model. Key phases to this model are the transport phase, and the anti-diffusion phases, which are outlined in greater detail in [82].

### 3.2.6 Energy transport and the ICCG method

Next within the POLLUX algorithm is the transport of energy. After the material absorbs energy from the laser, or if the Spitzer-Härm model determines a change in equilibrium temperature from collisions, the Thomas-Fermi (TF) model is used to work out how much this change in energy will affect the magnitude of the volume in the model. This change

in volume is then compared to the set volume of each cell, and any energy outside the set volume is transported into allocated cells outside the ones with set volume. These cells are described in the form of vectors with  $z$  and  $r$  directions.

Once the TF calculations are complete, the Incomplete Cholesky-Conjugate Gradient (ICCG) method is used to provide an even more accurate calculation of the transport of energy. This fast-processing vectorisable algorithm uses an series of iterative equations to compute a system of unknown vectors  $x$ , and  $y$ , with matrix  $M$  assumed to be symmetric and positive-definite.

$$Mx = y \quad (3.5)$$

Additionally, the matrix  $M$  be described as a combination of its lower triangular matrix,  $L$ , and its transpose,  $L^T$ , as in equation 3.6:

$$M = LL^T \quad (3.6)$$

An assumption for the ICCG algorithm to be accurate is that  $M$  must be symmetric and positive-definite, in which all diagonal cells are non-zero.

### 3.2.7 Outputs from POLLUX

There are eight output parameters from POLLUX that are of interest in this work, as outlined in table 3.2. At each iteration of a simulation, each of these are provided for each cell in the Eulerian mesh. After a simulation is finished, the output parameters are stored in files which can be imported into other data handling software for graphic plots or further analysis. In this work, the MATLAB programming platform was used to analyse files outputted from POLLUX, such as by creating contour plots of the temporal evolution of different output parameters.

Table 3.2: Constructed tabular Chart-D EoS for Al, Au, Zn, Cu, Ti and Ta

<b>Parameter of plasma plume</b>	<b>Unit</b>
Axial position	(cm)
Radial position	(cm)
Mass density	(g cm <sup>-3</sup> )
Axial velocity	(cm s <sup>-1</sup> )
Radial velocity	(cm s <sup>-1</sup> )
Ion temperature	(eV)
Electron temperature	(eV)
Average ionisation state	1 = neutral, 2 = 1 <sup>+</sup> , 3 = 2 <sup>+</sup> , etc.

### 3.3 TALIF plasma diagnostic

Two-photon absorption laser-induced fluorescence (TALIF) is a diagnostic used to characterise the background plasma content in our PE-PLD setup. This is done by measuring the atomic oxygen and nitrogen densities, as it is this parameter that is known to be the starting point of any highly reactive oxygen and nitrogen species, primarily created through electron impact dissociation of O<sub>2</sub> and N<sub>2</sub>. The atomic oxygen and nitrogen densities are measured against three key parameters of O<sub>2</sub> and N<sub>2</sub> plasmas to achieve stoichiometric metal oxynitride thin films: applied RF power; chamber pressure; and the ratio of oxygen:nitrogen content in O/N admixtures. TALIF works by firing a tunable pulsed laser at the plasma species of interest, exciting ground-state atoms into higher electronic states, as shown in figure 3.5. This emits fluorescence, which is then measured to derive the population of ground-state atoms, and subsequently the ground-state atomic density, which is how the desired amount of background plasma content is characterised.

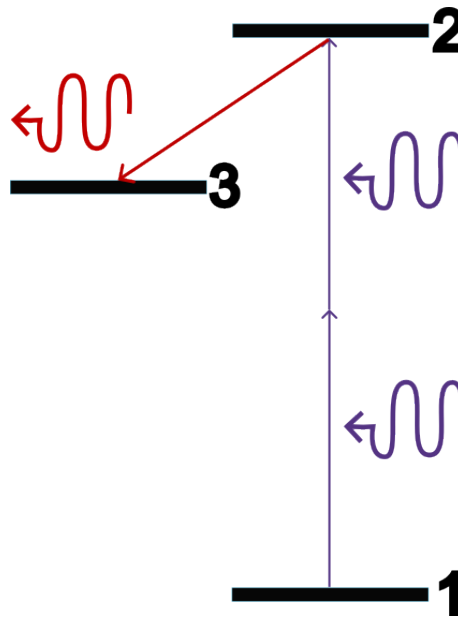


Figure 3.5: TALIF excitation scheme. The laser selectively excites an electron from the ground state (level 1) of the atom to level 2 using two photons absorbed simultaneously. This electron subsequently decays to level 3, emitting a photon (e.g. 844 nm in case of oxygen) that is measured with e.g. an iCCD camera.

TALIF is built on the well-established laser-induced fluorescence (LIF) diagnostic by using two photons to excite atomic species instead of one, which is useful if the laser wavelength required to excite is unavailable, as is the case for oxygen and nitrogen plasma species [103]. A schematic diagram of the experimental setup of the TALIF diagnostic in the York Plasma Institute Laboratories can be seen in fig 3.6.

In fig 3.6, a Continuum Surelite EX Nd:YAG laser produced a photon beam of pump wavelength 355 nm which was pulsed at a temporal width of 5-7 ns FWHM. The pulsed laser then passed through a Continuum Horizon optical parametric oscillator (OPO) unit, which tuned the photons to specific wavelengths selected to cause transitions of interest for species within the plasma, within its available range of 192-2750 nm. The laser then travelled through a pair of  $\text{CaF}_2$ -coated variable attenuators (Layertec), which controlled the energy of the laser to keep it below saturation. Two pairs of attenuators were used overall, whose transmission wavelength differed: a pair of 226 nm transmission-wavelength attenuators were used if oxygen was the species to be measured; and a pair of 206 nm-wavelength attenuators were used if nitrogen was to be measured. Both pairs were mounted on a stage and simultaneously adjusted using a Zaber T-NM17A04 stepper motor. A beam splitter was put in place after the attenuators to divert approximately 1-2% of the

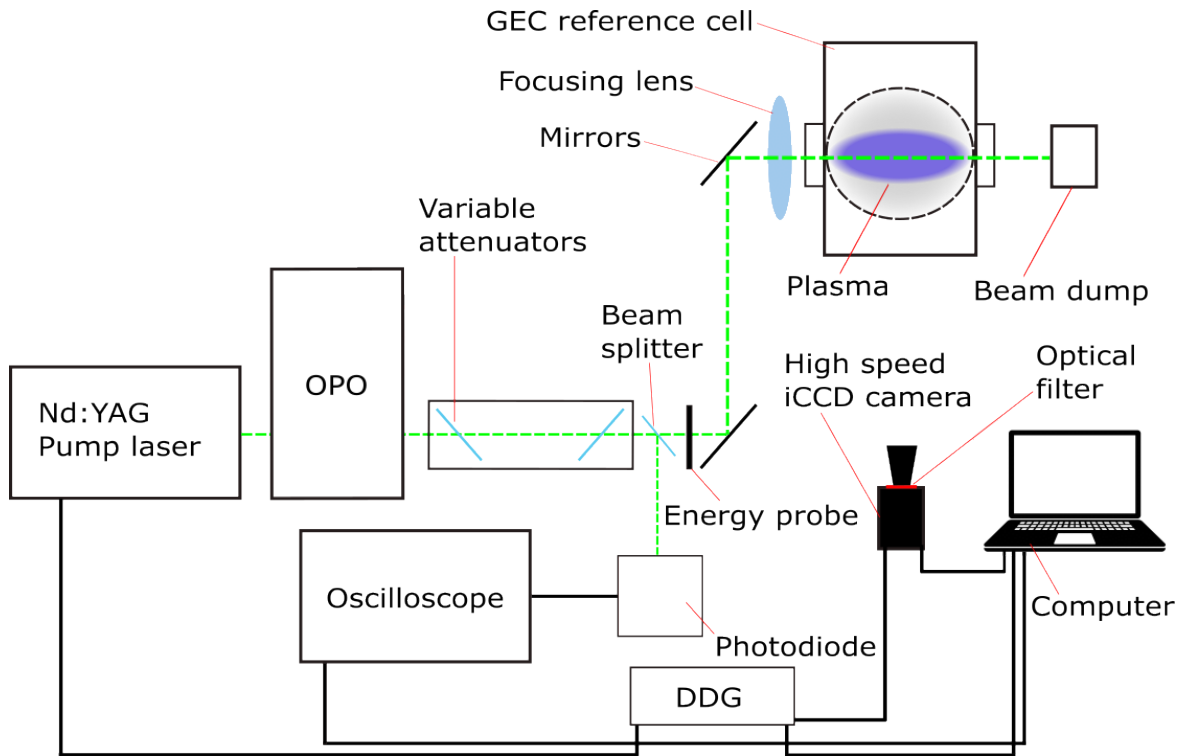


Figure 3.6: Schematic diagram of the TALIF diagnostic setup in the York Plasma Institute Laboratories. The green dotted line indicates the pulsed laser beam, travelling through the attenuators, mirrors, and lens, entering the GEC chamber containing the plasma, and terminating at a beam dump. The energy probe measures laser energy and is removed during fluorescence measurements.

laser energy to a photodiode (ThorLabs DET10A/M), which measured the pulse time and energy of the beam in situ with measurements. The remainder of the laser pulse was directed to the Gaseous Electronics Conference (GEC) reference cell where the plasma was generated. Two mirrors were used to align the laser beam through a focusing lens in front of the GEC, which positioned the focal point at the centre of the GEC. The first mirror was positioned ahead of the variable attenuators in the setup, and the second was positioned in front of the GEC and the lens.

The plasma was an ICP generated in a similar way to the PE-PLD background plasma (see section 3.1). Although the plasma chamber used here was different to the one used in PE-PLD, the GEC reactor and RF generator were identical, with two key differences: the automatic matching network was used with the RF generator in the TALIF setup, whereas the one in the PE-PLD setup had a manual matching network; and the pressure of the GEC chamber could be changed using an MKS 600 Series pressure controller, meaning the overall

chamber pressure could be controlled without having to alter the set points or flow rates on the mass flow controller. The laser passed through the GEC chamber, approximately 14 mm above the bottom electrode, and was terminated by a beam dump. Fluorescence occurred in the chamber when the generated plasma was excited by the laser, which could be viewed through a quartz window ( $\sim 20$  cm diameter) on the side of the GEC perpendicular to the laser direction. The fluorescence was then captured by a high speed iCCD camera (Andor iStar DH224T-18U-73, 500 kHz maximum repetition rate) facing the window, as seen in figure 3.6.

An optical bandpass filter was placed behind the iCCD camera lens, which filtered out wavelengths outside the range of interest, differing depending on the species being measured:  $844.6 \pm 1$  nm for O; 740-750 nm for N;  $835 \pm 10$  nm for Xe; and  $825 \pm 10$  nm for Kr. The two noble gases were used to calibrate against the oxygen and nitrogen species respectively, as described in more detail in subsection 3.3.6. Additionally, a SIGMA DC Optical Stabilizer lens was set up in front of the camera to aid with imaging the fluorescence onto the charge-coupled device (CCD). Once the camera captured an image, it was viewed on the Andor SOLIS computer software. For each scan, a series of images was taken with the camera; for each series, a background measurement was taken without the presence of the laser fluorescence at the beginning of each scan to remove possible background noise produced from either the plasma or the camera.

The triggering of the laser, plasma pulse, and camera were all synchronised by a digital delay generator (DDG). The synchronisation can either be done manually on the DDG, or programmed via script using the Andor SOLIS software (see figure 3.7 for the timing of each component during each TALIF cycle). The photodiode was connected to an oscilloscope (LeCroy Waverunner 204MXi-A 2 GHz 10 GSs<sup>-1</sup>), which measured its generated voltage. The oscilloscope was also used to display waveforms corresponding to the plasma pulse, laser pulse, duration of which the camera shutter was active, and so on. The oscilloscope can display multiple waveforms simultaneously, which provided useful information on the values of the timings of each event used on the DDG.

Finally, an energy probe was placed between the beam splitter and the mirror in front of it to measure the laser pulse energy before each set of measurements. After the laser energy was measured, it was placed out of the path of the laser away from the setup, while experiments were in progress. Further details on each component are described in [104].

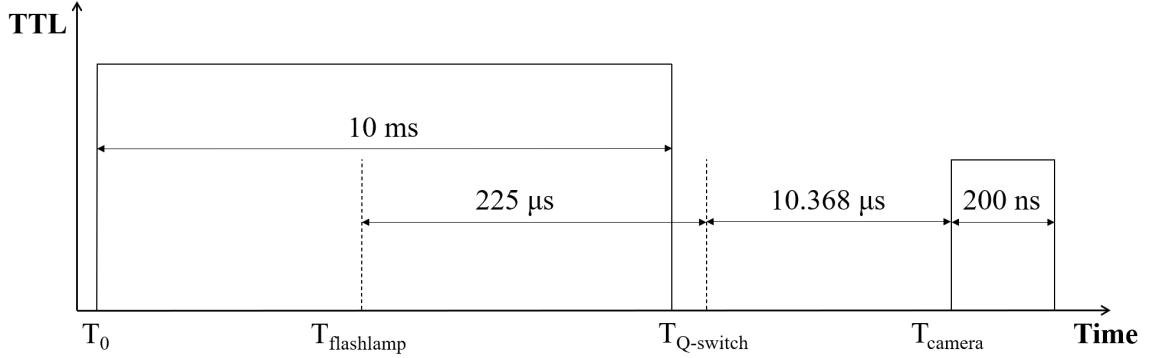


Figure 3.7: Timing scheme for the digital delay generator (DDG) in the TALIF setup in the York Plasma Institute Laboratories. The DDG externally pulses the plasma on at time  $T_0$ , lasting 10 ms. The plasma pulse is powered off for 90 ms, creating a 10% duty cycle, coinciding with the laser pulse rate. The time at which the Q-switch triggers,  $T_{Q-Switch}$ , can vary relative to the camera triggering,  $T_{camera}$ , to study fluorescence at different times in the afterglow. However, the laser flashlamp always triggers at time  $T_{flashlamp} = T_{Q-Switch} - 225\mu s$  to maximise the output energy of the tuneable laser. The camera gate-width was set to 200 ns.

### 3.3.1 Calibration with noble gases to obtain absolute atomic densities

In experimental practice, fluorescence scans are done for both the species of interest and a noble gas the diagnostic is calibrated with, to obtain absolute densities. This is because it is impossible to obtain absolute densities with excited plasma particles, as they are unstable and spontaneously decay by photon emission [3]. Therefore, noble gases with similar two-photon resonances are used, and absolute density can be quantified from the ground-state pressure, using the ideal gas law. As seen in figures 3.8 and 3.9 the case of oxygen, xenon is used. For nitrogen, krypton is used. This calibration method was used in [2], and is not the only method that can calibrate the fluorescence signal into absolute number densities. Titration methods can also be used, though such methods introduce further experimental complications unnecessarily.

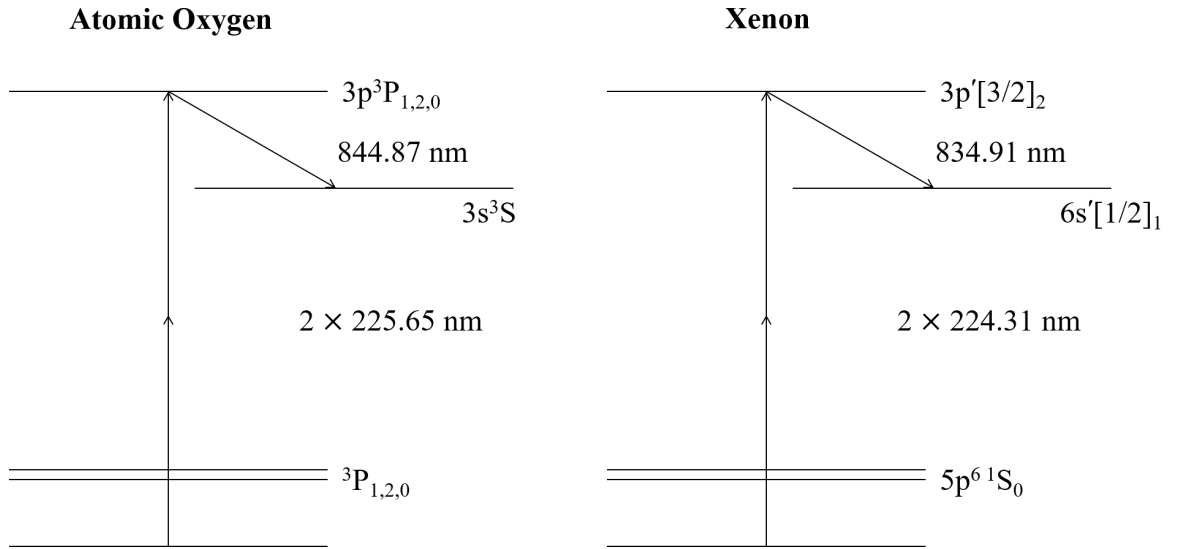


Figure 3.8: Two-photon excitation scheme for atomic oxygen and xenon [2].

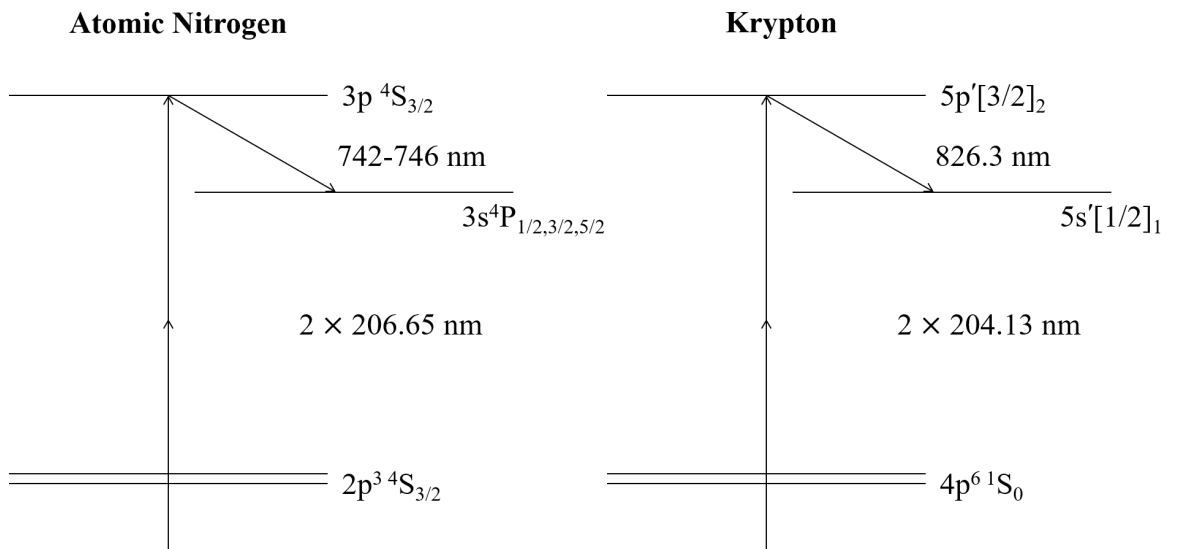


Figure 3.9: Two-photon excitation scheme for atomic nitrogen and krypton [3].

### 3.3.2 Collisional quenching

Excited states in the plasma species can collide with other species, including ground-state neutrals, resulting in a faster decay in fluorescence intensity compared to if there were no collisions. This is called collisional quenching. Due to this phenomenon, it is infeasible to identify the fraction of excited species that decays to the energy level which can be measured, so this must be accounted for to obtain the correct atomic density. Only one transition is permitted for atomic oxygen and atomic nitrogen respectively [105] [106], but the noble gases,

xenon and krypton, have more than one allowed transition with different probabilities, yet the optical filter in the experimental setup only allows for one of these transitions to be measured, and not the other, as illustrated in figure 3.10.

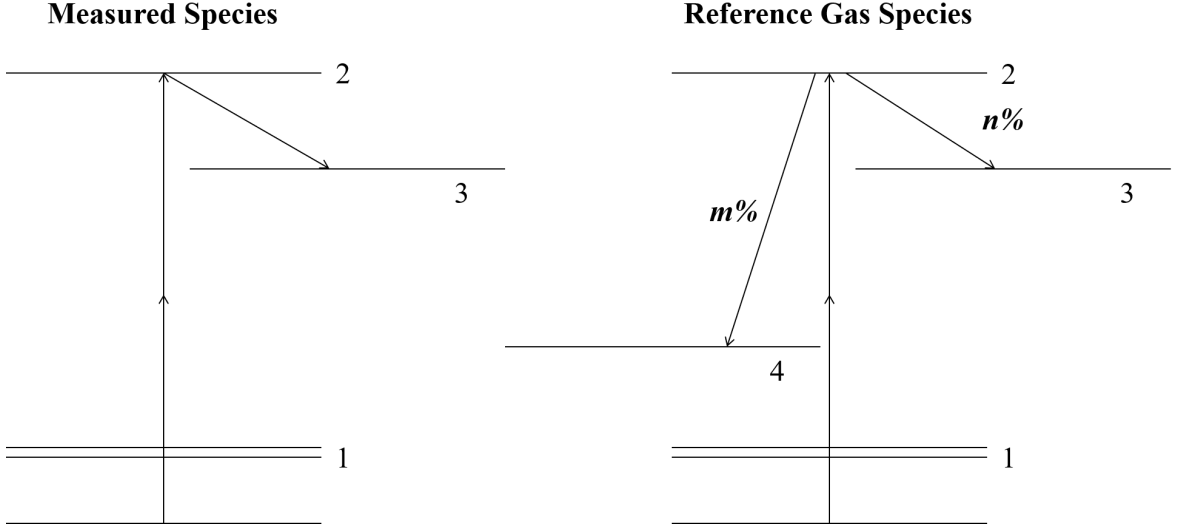


Figure 3.10: Schematic comparing the TALIF excitation scheme of a measured plasma species, e.g. atomic oxygen or nitrogen, with that of a reference gas species, e.g. xenon or krypton, with collisional quenching taken into account. In this schematic, the noble gas has an  $n\%$  chance to decay from excited state 2 into lower excited state 3, which can be measured, and an  $m\%$  chance to decay into lower excited state 4, which cannot be measured with the same optical filter.

The probability of the measurable transition is known as the optical branching ratio,  $b$ , which is calculated from the natural and effective lifetimes from equation 3.7:

$$a_{23} = b_{23} \frac{\tau_{eff}}{\tau_{nat}} \quad (3.7)$$

where  $\tau_{nat}$  denotes the natural lifetime of the fluorescence,  $a_{23}$  is the optical branching ratio from excited state 2 to decayed state 3 (see figure 3.10);  $b_{23}$  is the pure optical branching ratio into any specific state 3 [107].

### 3.3.3 Saturation of laser energy

For each plasma species, an appropriate value for the energy of the laser pulse must be chosen, which is measured by the beam probe in figure 3.6. Increasing the laser energy can improve the signal-to-noise ratio of the TALIF signal. However, if the energy is too high, saturation effects can occur, leading to a loss of fluorescence signal through photoionisation

effects. Moreover, if the laser energy is high enough, photodissociation effects may arise, resulting in an overestimation of the fluorescence signal. Thus, an energy saturation curve must be determined for each plasma species by recording fluorescence signals at different beam energies. The signal is plotted against the square of the beam energy, as shown in figures 3.11-3.14, and a linear relationship is observed until deviations occur at high enough beam energies. Saturation occurs at such energies, and an appropriate pulse energy within the linear fit is chosen.

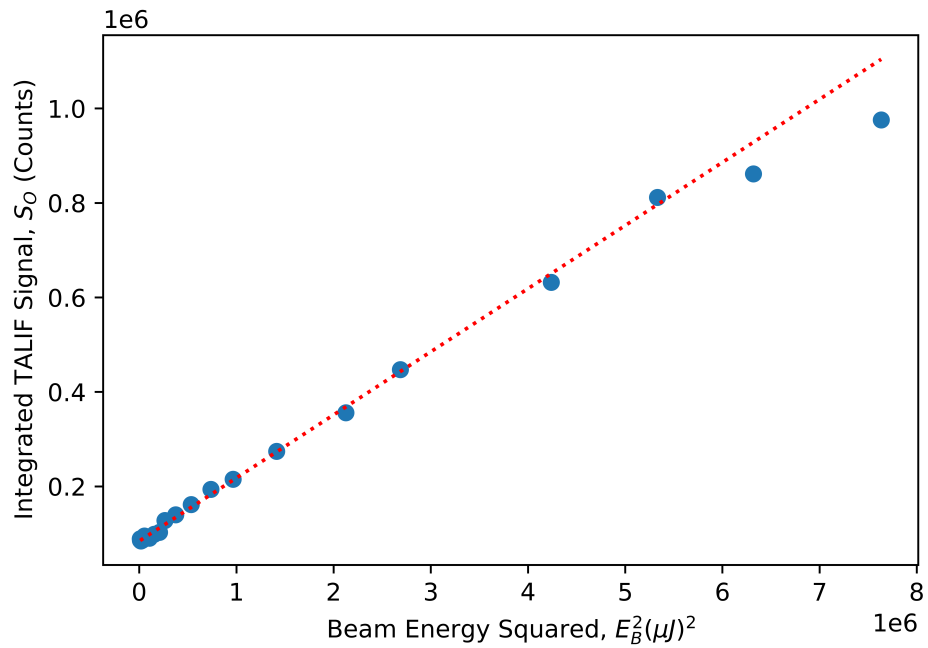


Figure 3.11: Energy saturation curve for oxygen at a gas pressure of 20 Pa. The signal begins saturating after  $E^2 \approx 5.3 \times 10^6 (\mu\text{J})^2$ , or  $E = 2309 \mu\text{J}$ . Therefore, 850  $\mu\text{J}$  was the approximate pulse energy chosen for oxygen experiments.

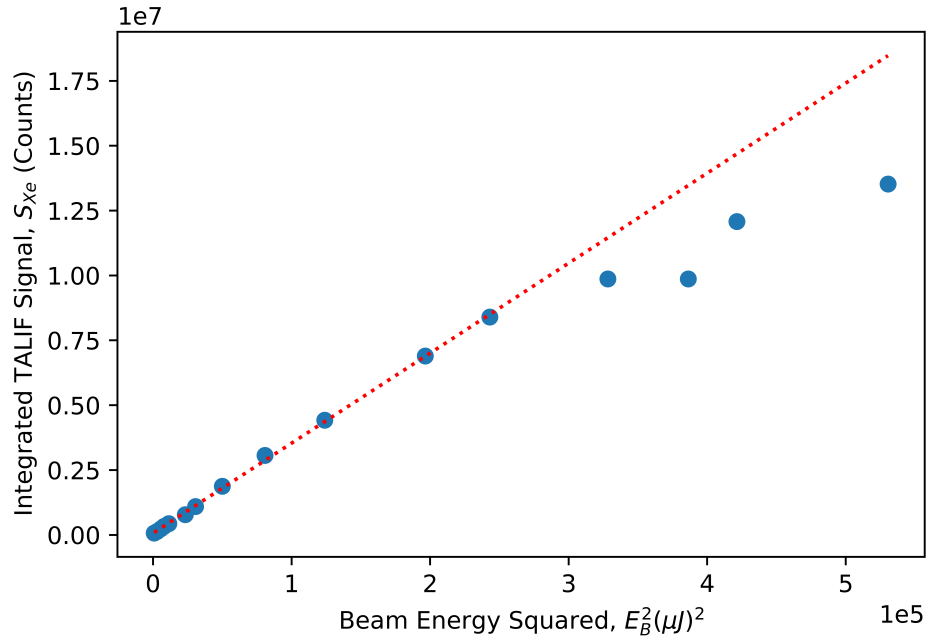


Figure 3.12: Energy saturation curve for xenon at a gas pressure of 20 Pa. The signal begins saturating after  $E^2 \approx 2.4 \times 10^5 (\mu\text{J})^2$ , or  $E = 493 \mu\text{J}$ . Therefore, 305  $\mu\text{J}$  was the approximate pulse energy chosen for xenon calibration.

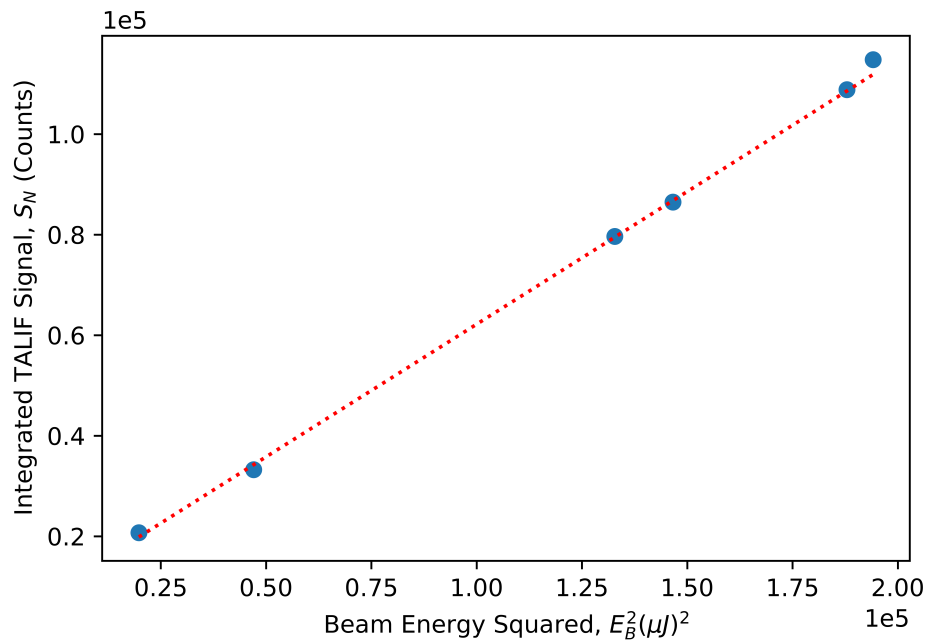


Figure 3.13: Energy saturation curve for nitrogen at a gas pressure of 20 Pa. The energy did not saturate within the measured range, but it was observed that increasing the laser energy increased plasma emissions at an increased rate, resulting in the fluorescence becoming more difficult to observe. Therefore, laser energy of approximately  $E = 435 \mu\text{J}$  ( $E^2 \approx 1.8 \times 10^5 (\mu\text{J})^2$ ) was chosen for nitrogen experiments.

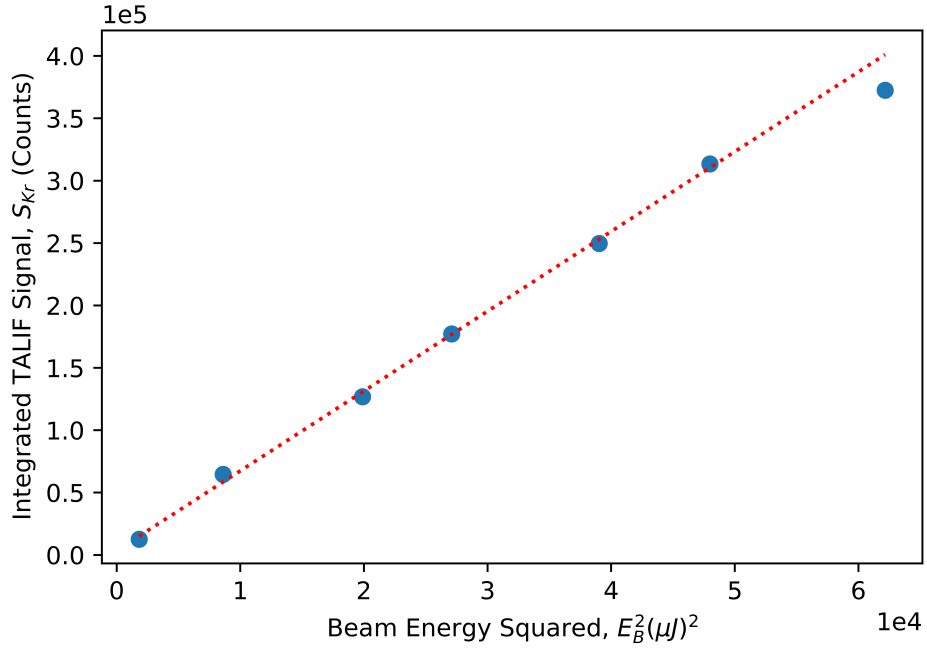


Figure 3.14: Energy saturation curve for krypton at a gas pressure of 20 Pa. The energy began saturating after  $E = 219\mu\text{J}$  ( $E^2 = \sim 4.7 \times 10^4(\mu\text{J})^2$ ). Laser energy of approximately  $E = 230\mu\text{J}$  ( $E^2 = \sim 1.8 \times 10^5(\mu\text{J})^2$ ) was chosen for krypton calibration to optimise fluorescence intensity.

### 3.3.4 Calculating the atomic density

To calculate the atomic density from the fluorescence signal, equation 3.8 is used [104]:

$$n_x = \frac{S_X \eta_X T_X a_{23R}}{S_R \eta_R T_R a_{23X}} \left( \frac{E_R}{E_X} \right)^2 \left( \frac{\lambda_R}{\lambda_X} \right)^2 \frac{\sigma_R^{(2)}}{\sigma_X^{(2)}} n_R \quad (3.8)$$

in which parameters denoted with subscript  $X$  correspond to those of the investigated species, which is calibrated against parameters corresponding to noble gas species, represented by subscript  $R$ ;  $S$  is the fluorescence signal;  $\eta$  is the quantum efficiency of the detector;  $T$  is the optical filter transmission;  $E$  is the laser pulse energy;  $a_{23}$  is the optical branching ratio from excited energy level 2 to fluorescence channel 3, which is the particular transition of interest in this work;  $\lambda$  is the laser pulse energy; and  $\frac{\sigma_R^{(2)}}{\sigma_X^{(2)}}$  is the two-photon excitation cross-section ratio.  $\eta$  and  $T$  are known values provided with iCCD camera and optical filters respectively. The  $\lambda$  wavelengths are determined by experiment, as mentioned in section 3.3.6, and the two-photon excitation cross-sections are obtained from the literature. To simplify the equation, all constant parameters can be represented by constant  $C$ , and all effective

decay parameters ( $E$ ,  $a_{23}$ ) can be grouped together and represented by constant  $A$  [104], giving equation:

$$n_x = C \frac{S_X}{S_R} \frac{A_R}{A_X} n_R \quad (3.9)$$

### 3.3.5 Constants and error estimation

Table 3.3 contains constants used in equation 3.8 to calculate absolute densities of O and N. All four filter transmission efficiencies were measured by an Ocean Optics HR4000CG-UV-NIR spectrophotometer (0.06 nm resolution), and all four quantum efficiencies were taken as stated by the manufacturer of the detector.

Table 3.3: Constants used for calculation of absolute atomic densities using equation 3.8.

Species	$\lambda$ (nm)	$\tau_{nat}$ (ns)	$b$	$T_X$ (%)	$T_R$ (%)	$\eta$ (%)
O	225.65 [2]	$34.7 \pm 1.7$ [2]	1.0	$73.4 \pm 1$	-	$18.02 \pm$ 0.02
N	206.72 [2]	$29.6 \pm 0.1$ [103]	1.0	$58.3 \pm 1$	-	$24.19 \pm$ 0.02
Xe	224.31 [2]	$40.8 \pm 2.0$ [2]	0.733 [108]	-	$60.1 \pm 1$	$19.52 \pm$ 0.02
Kr	204.20 [2]	$34.1 \pm 0.1$ [103]	0.958 [103]	-	$81.0 \pm 1$	$20.60 \pm$ 0.02

For the two-photon excitation cross-section ratio, the following values are used for O and N respectively [103]:

$$\frac{\sigma_{Xe}^{(2)}}{\sigma_O^{(2)}} = 0.36(\pm 20\%) \quad (3.10)$$

$$\frac{\sigma_{Kr}^{(2)}}{\sigma_N^{(2)}} = 0.67(\pm 50\%) \quad (3.11)$$

The uncertainties of the  $n_x$  values are taken by adding each term in equation 3.8 in quadrature. There was a systematic error in the Horizon software which resulted in an experimental offset for the optimal wavelength of fluorescence for each species. This was cal-

ibrated by changing each wavelength value to the correct wavelength with a simple shift. The atomic oxygen and xenon wavelength offsets were both  $\sim 2.12$  nm, and the wavelengths which gave peak fluorescence signals were 223.52 nm for atomic oxygen and 222.19 nm for xenon. Additionally, there was a wavelength offset of  $\sim 1.5$  nm for atomic nitrogen and krypton, and the wavelengths which gave peak fluorescence signals were 205.14 nm for atomic nitrogen and 202.65 nm for krypton. The theoretical vacuum laser wavelengths for each species in the literature were used in calculating  $n_x$  from equation 3.8. The spectral scans account for the uncertainty in the wavelength due to their definitive peaks (see figure 3.16). As for the other uncertainties, the quantum efficiency errors were provided by the manufacturer of the iCCD camera. The error in the optical filter transmission is 1%. The errors associated with the remaining parameters in table 3.3 are explained in the literature cited with each value. Of each of the parameters, the two-photon cross-section error contributes the most to the final error in the atomic density measurement, which is estimated to be more than  $\pm 50\%$ . This is a systematic error, meaning any correlations observed will still be preserved. It is also important to note that atomic densities can vary over several orders of magnitude, and so an error of 50% is reasonable on a logarithmic scale.

### 3.3.6 Spectral Scans

For each species, fluorescence can occur over a range of neighbouring laser wavelengths due to causes such as instrumental broadening. Therefore, at the beginning of each TALIF experiment, a spectral scan was required to obtain a spectral profile of the laser wavelength, which was then integrated to obtain the total fluorescence signal,  $S$ . By obtaining the spectral profile, the optimal fluorescence wavelength for the species of interest was also determined. The laser wavelength was varied, observing the subsequent fluorescence signal, and recording the signal strength. Initially, a rough estimate for the peak wavelength was obtained based on the theoretical peak wavelength and taking the systematic error of the Horizon software into account. Then, a spectral scan was performed over a range of wavelengths below and above this estimated wavelength, in small increments of 0.01 nm. This provided a precise peak wavelength of fluorescence within the 0.01 nm resolution, which was then used as the central wavelength in future spectral scans of the respective plasma species, as well as the wavelength during fluorescence decay scans. For example, when determining the peak wavelength for atomic nitrogen, an estimate for the wavelength offset was determined based on an offset

for krypton which had been established in previous work with the TALIF setup [109], which was approximately 1.48 nm. Subtracting this from the theoretical peak wavelength of atomic nitrogen gave a value of 205.17 nm. Thus, a spectral scan was performed ranging from 205.10-205.23 nm in steps of 0.01 nm. Repeat scans showed that 205.14 nm was the wavelength which consistently gave the strongest fluorescence signal for atomic nitrogen, hence was used in all future atomic nitrogen measurements. For all experiments with all species, the range of each spectral scan was  $\pm 0.07$  nm around the central wavelength in steps of 0.01 nm (e.g. from 223.45-223.59 nm for atomic oxygen, whose peak wavelength was 223.52 nm). Figure 3.15 shows an example of an image with fluorescence taken by the iCCD camera. The fluorescence signal,  $S$ , is the photon emitted due to the transition of the electron in the second state (2) to the third state (3), as seen in figures 3.8 and 3.9.

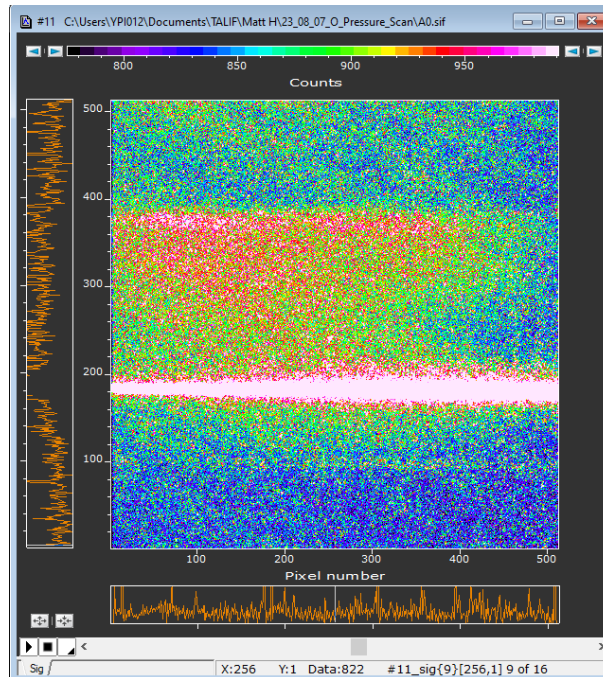


Figure 3.15: Example of a fluorescence signal taken from the iCCD camera viewed on the Andor SOLIS software in the TALIF experimental setup in the York Plasma Institute Laboratories. Displays the fluorescence signal of an  $O_2$  plasma at 15 Pa pressure and 600 W power at the peak wavelength of fluorescence (225.65 nm).

The fluorescence signal strength varies with wavelength, following a Gaussian curve, and peaking at one specific wavelength, e.g., 225.65 nm in the case of oxygen, as displayed in figure 3.16. This peak wavelength is used as the fixed wavelength in fluorescence lifetime measurements, as well as a parameter in calculating the atomic density of the plasma species

of interest. The spectral width of the TALIF signal that can be measured is a convolution of multiple mechanisms: spectral width of the laser (assumed to be the primary broadening mechanism); Doppler broadening; and pressure broadening.

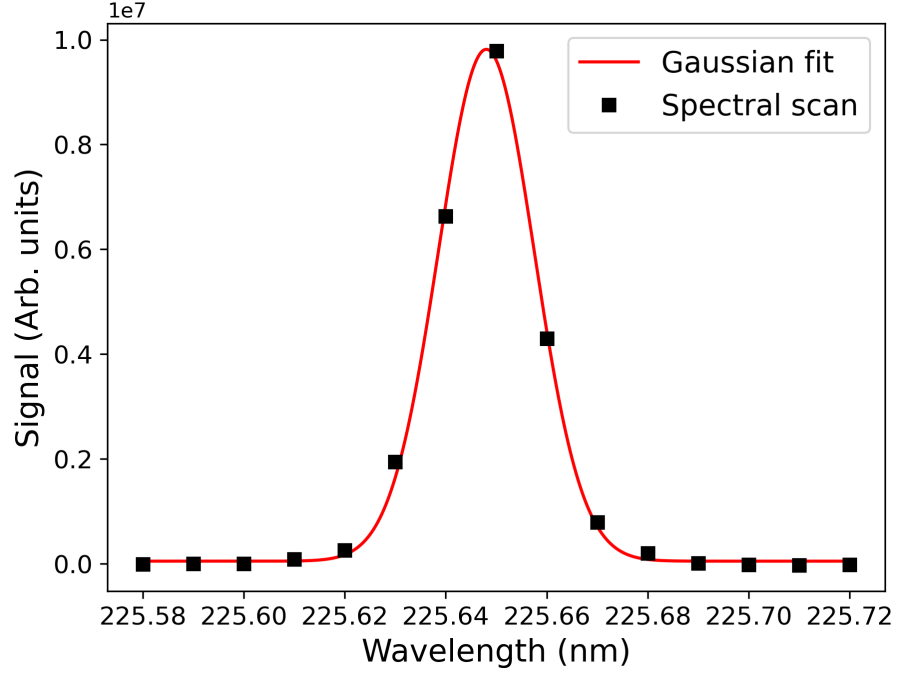


Figure 3.16: Example of a spectral profile of atomic oxygen plasma at 20 Pa GEC chamber pressure and 600 W RF power. The spectral width of the laser is assumed to be the dominant broadening mechanism, which has a Gaussian profile, hence the Gaussian fit applied to the fluorescence. The area under this Gaussian is defined as the total fluorescence signal,  $S$ .

### 3.3.7 Fluorescence Decay

Once the optimal wavelength of fluorescence is obtained, it is used in measuring the decay of the fluorescence. This provides the effective lifetime of the fluorescence,  $\tau_{eff}$ , which is another parameter required to work out atomic density, see equation 3.8.

The effective lifetime,  $\tau_{eff}$ , accounts for quenching according to equation 3.12:

$$\frac{1}{\tau_{eff}} = \frac{1}{\tau_{nat}} + \sum_q k_q n_q = A^* \quad (3.12)$$

where  $\tau_{nat}$  denotes the natural lifetime of the fluorescence,  $k_q$  is the quenching coefficient,  $n_q$  is the density of the quenching partner (i.e. the species which quench the excited plasma state), and  $A^*$  is the effective decay rate.

An example of a fluorescence decay is displayed in figure 3.17. The effective lifetime of

the fluorescence,  $\tau_{eff}$ , is derived from an exponential fit applied to the data. The natural lifetime of the species in question,  $\tau_{nat}$ , is known from the literature. The effective lifetime and the ground-state atomic density will differ depending on the pressure of the chamber.

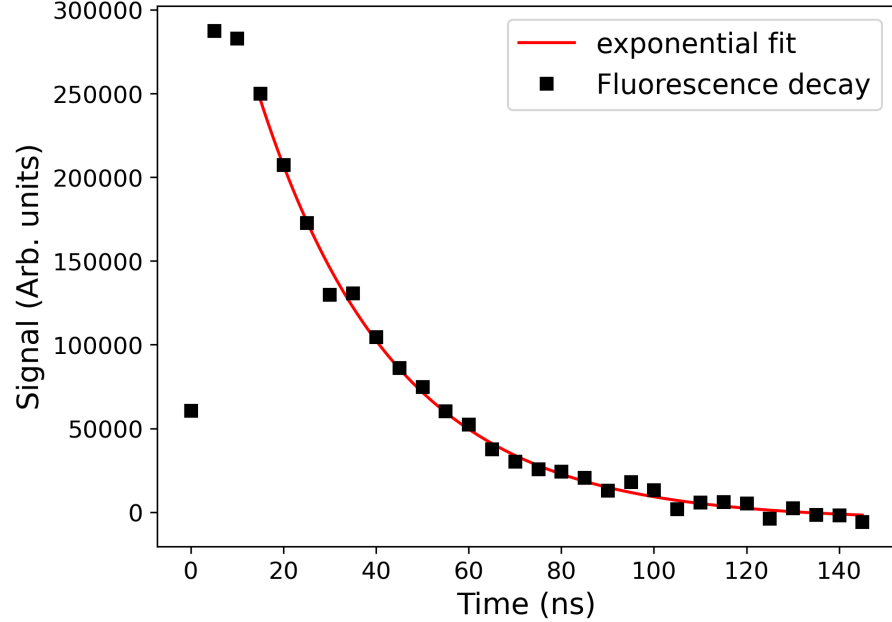


Figure 3.17: Example of a fitting of an exponential decay curve to a fluorescence signal of atomic oxygen plasma at 20 Pa GEC chamber pressure and 600 W RF power. The effective lifetime,  $\tau_{eff}$ , is derived from the decay constant of the exponential curve, which is required for calculating the optical branching ratio,  $b$ , and in turn the atomic density of the plasma.

The final equation used to calculate absolute atomic density  $n$  with all parameters accounted for is shown in 3.8 [104].

## 3.4 Thin film diagnostics

The diagnostics addressed in this section are used to investigate various characteristics of deposited thin films, including surface characteristics and chemical composition.

### 3.4.1 Scanning electron microscopy (SEM)

Scanning electron microscopy (SEM) is an imaging technique which creates nanoscale images of a solid sample by scanning the surface with a focused beam of high-energy electrons. In this work, SEM imaging is used to probe surfaces of thin films and substrate samples, with and without thin films deposited onto them. Figure 3.18 displays a diagram of an SEM

setup. The electrons are produced by a gun at the top of the column and are accelerated down through a vacuum to energies up to 30 keV. They are passed through a combination of lenses and apertures to produce a focused beam of electrons, which is directed at the surface of the sample. The beam penetrates the sample to a depth of approximately a few microns, depending on the accelerating voltage of the electrons and sample density. As the electrons interact with the sample, they produce secondary and backscattered electrons. These signals are collected by different detectors to form images which can be viewed on computer software.

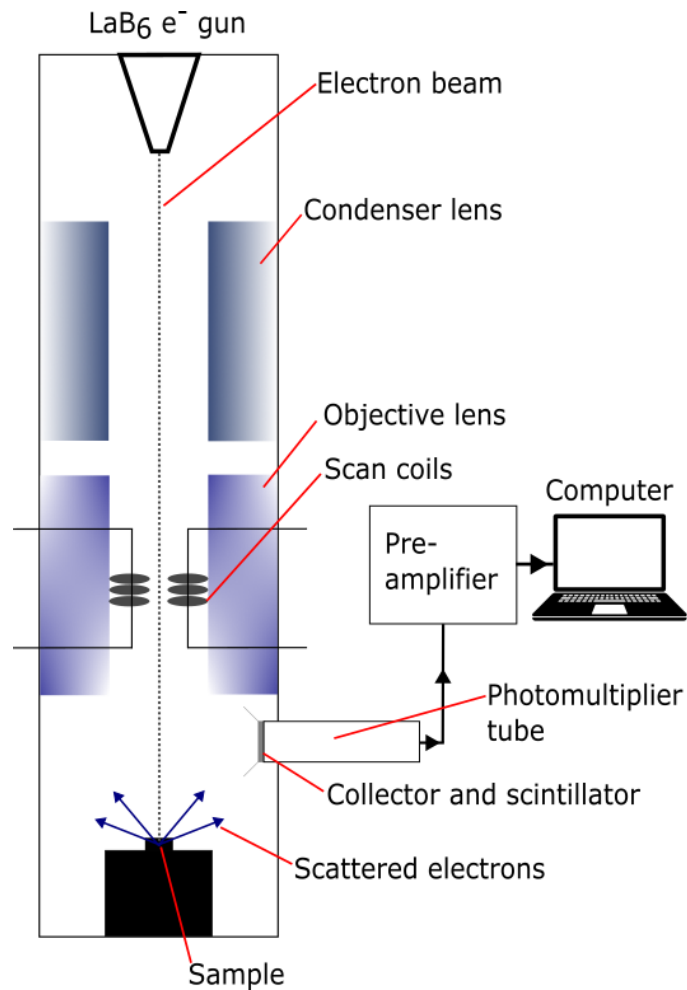


Figure 3.18: Schematic of an SEM setup.

Most modern SEMs can provide image resolution between 1-20 nm and some can even provide resolution below 1 nm. However, a limitation is the sample must conduct electricity well, meaning silicon substrates fare better than quartz for this method. It is common to use other diagnostics alongside SEM to detect and measure other types of emitted radiation, such as X-rays.

### 3.4.2 Energy-dispersive X-ray spectroscopy (EDX)

Energy Dispersive X-Ray Spectroscopy (EDX) is a technique often used in conjunction with SEM. It is used to identify the chemical composition of a sample by measuring the energy and intensity distribution of characteristic X-rays emitted from the surface of a sample during collisions of the SEM electron beam with the sample. Electrons released from the sample leave behind vacant holes which are subsequently filled by electrons from higher energy levels (known as K, L, and M levels). This results in the emission of characteristic X-ray photons of energy unique to the element from which they were emitted. These X-ray photons typically have names such as  $K_\alpha$ ,  $K_\beta$ ,  $L_\alpha$ , etc, with  $\alpha$  and  $\beta$  indicating the higher shell the electron decayed from to fill the vacancy and produce the photon. A schematic diagram of characteristic X-ray emission following electron interaction with an atom is shown in figure 3.19.

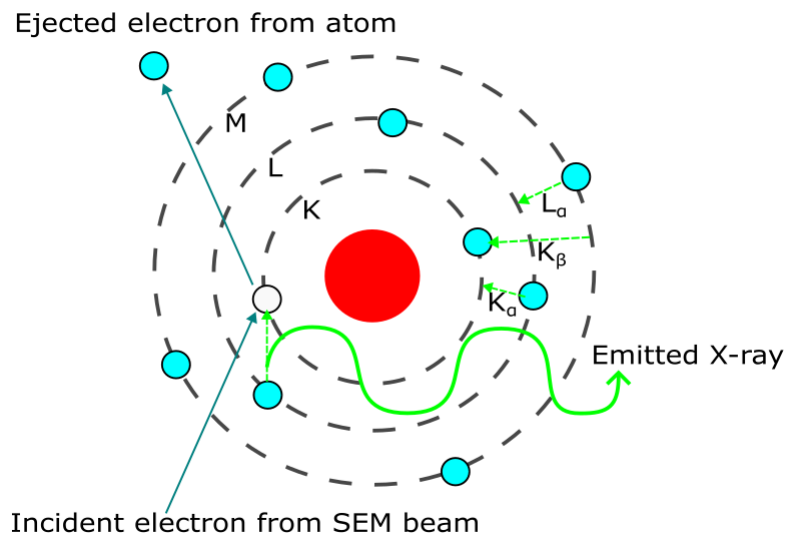


Figure 3.19: Schematic diagram of characteristic X-ray emission. As the high-energy electron beam causes inner shell electrons to be emitted, electrons from higher energy levels relax and occupy the holes left behind, emitting characteristic X-ray photons.

The characteristic X-rays are received by a silicon drift detector fixed within the SEM, which produces a current for photons measured directly proportional to photon energy. A histogram of X-ray energy as a function of X-ray counts is then plotted, with peaks corresponding to different chemical species present in the sample. The position of the peak is compared to literature, which provides the element detected. By calculating the area under the peak, the quantity of the element present in the sample can be obtained, hence

the stoichiometry of the constituent elements of the thin film.

In this work, all thin films analysed using EDX had the following SEM conditions:

Working distance: 10 mm

Beam energy: 10 keV

Detector types: LED filter 3

Magnification: 1000x

Probe current: 12  $\mu\text{A}$

### 3.4.3 Ultraviolet–visible (UV/Vis) absorption spectroscopy

UV/Vis absorption spectroscopy is a diagnostic used to measure the absorbance profiles of chemical species in thin films. As such, it is used in this work to investigate the suitability of deposited thin films as water-splitting photocatalysts from the fraction of UV and visible light absorbed. A thin film sample is inserted into a spectrophotometer, as shown in figure 3.20. A source of radiation (typically a heated tungsten filament) emits continuous wavelengths at intensity  $I_0(\lambda)$  through a monochromator which separates the wavelengths. Each individual wavelength is reflected back and transmitted through the sample, arriving at the photodetector one at a time. The wavelength that arrives at the photodetector can be changed by rotating the grating. The photodetector measures transmitted intensity,  $I(\lambda)$ . The spectrophotometer plots absorbance as a function of wavelength using equation 3.13:

$$A(\lambda) = \log_{10} \frac{I_0(\lambda)}{I(\lambda)} \quad (3.13)$$

UV/Vis spectroscopy is simple to use, but unlike the SEM and EDX diagnostics, transparent substrates such as quartz are required for the spectroscopy to work on thin films deposited in this work. Since the photodetector will absorb some light from the substrate in addition to the film, a spectrum must also be taken from a blank quartz substrate with no film deposited onto it and subtracted from each substrate with a deposited thin film to provide more accurate absorption spectra for each thin film.

### 3.4.4 X-Ray Diffraction (XRD)

X-Ray Diffraction (XRD) is a widely-established technique used to determine the crystal structure of solid samples. In this work, XRD is used to assess the crystal structure and

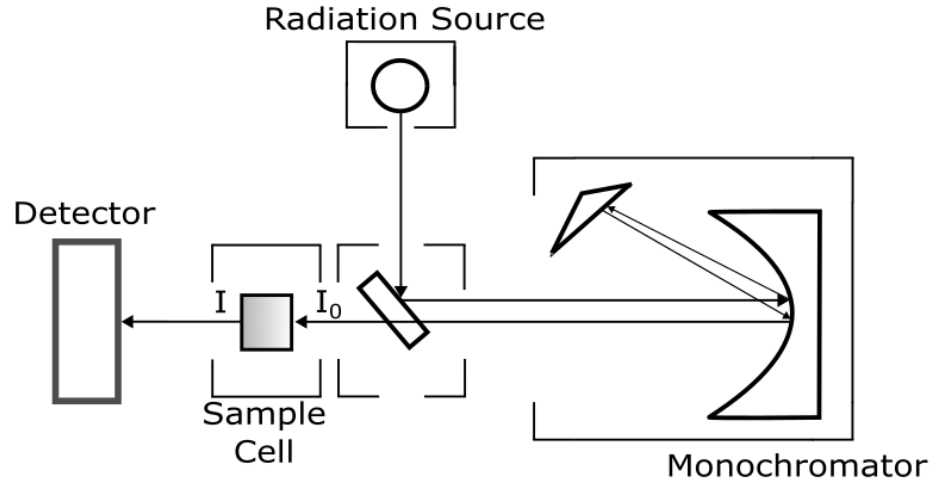


Figure 3.20: UV-Visible Spectrophotometer schematic. Wavelengths at intensity  $I_0$  emitted by the light source are reflected off the monochromator, separating the wavelengths as they travel back through the sample and reach the detector, which measures the transmitted intensity,  $I$ .

grain size of deposited films. A schematic of the experimental setup is displayed in figure 3.21. Here, a beam of X-rays is directed onto the sample with angle of incidence,  $\theta$ , and are scattered off by electrons of atoms present in the sample without altering the wavelength. The wavelengths of X-rays are mostly shorter than the interatomic spacing within the film, meaning most X-ray photons will not interact with the film at all as they pass through, but some will reflect and can be picked up by an X-ray detector [28]. When the angle of incidence equals the scattering angle (known as Bragg's angle), and the path difference between two reflected beams from different planes in the crystal differs by an integer multiple of wavelengths, constructive interference occurs, resulting in a peak in the observed signal. This peak corresponds to a specific lattice spacing,  $d$ , and the angle at which the peak is observed can be calculated using equation 3.14:

$$\lambda = 2d \sin \theta \quad (3.14)$$

where  $\lambda$  is the wavelength. Such angles can be compared to known values in databases or literature [110, 111] to ascertain the structure of deposited films.

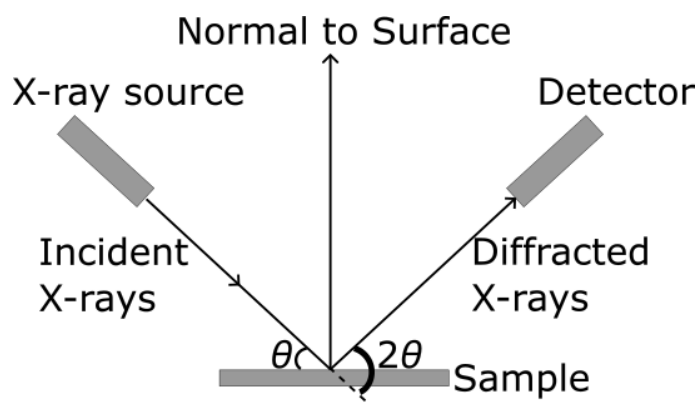


Figure 3.21: X-ray diffraction schematic.

### 3.4.5 X-ray photoelectron spectroscopy (XPS)

X-ray photoelectron spectroscopy (XPS), sometimes referred to as electron spectroscopy for chemical analysis (ESCA), is a technique which utilises the photoelectric effect to analyse the surface chemistry of a material. In addition to elemental composition, the diagnostic can measure the electronic state of atoms within a material. Renowned for its simple setup and capability of showing which elements and compounds are present in a sample, it is the most widely-used surface analysis technique.

An X-ray source of photon energy  $h\nu$  is directed onto the surface of the sample material, emitting photoelectrons from approximately the top 1-10 nm of the sample. These photoelectrons are captured by an electron energy analyser and their kinetic energy is measured, as in equation 3.15

$$E_k = h\nu - (E_B + \phi) \quad (3.15)$$

where  $E_B$  is the binding energy of the electron attracted to its respective nucleus, and  $\phi$  is the work function of the atomic species, i.e. the minimum energy required to remove an electron from the species. Afterwards, a spectrum of the ejected photoelectron counts over a range of kinetic energies is recorded, and the quantification of chemical content on the surface, including content of individual elements, can be deduced by the corresponding energies and intensities of the photoelectron peaks [112].

Figure 3.22 contains an plan view of the XPS schematic used in the University of York Department of Physics. The diagnostic uses a bandpass filter, which the electrons enter. If they are travelling too fast or too slow, they hit the walls of the filter. Electrons moving at

just the right speed will reach the detector, which determines the number of electrons that have reached it, which will all have a specific kinetic energy. From this and equation 3.15, the binding energy of the electron corresponding to the specific species can be determined. This is displayed on plots such as in figure 3.23, in which the intensity is a combination of the amount of species present, relative to the intensity of a reference species (carbon).

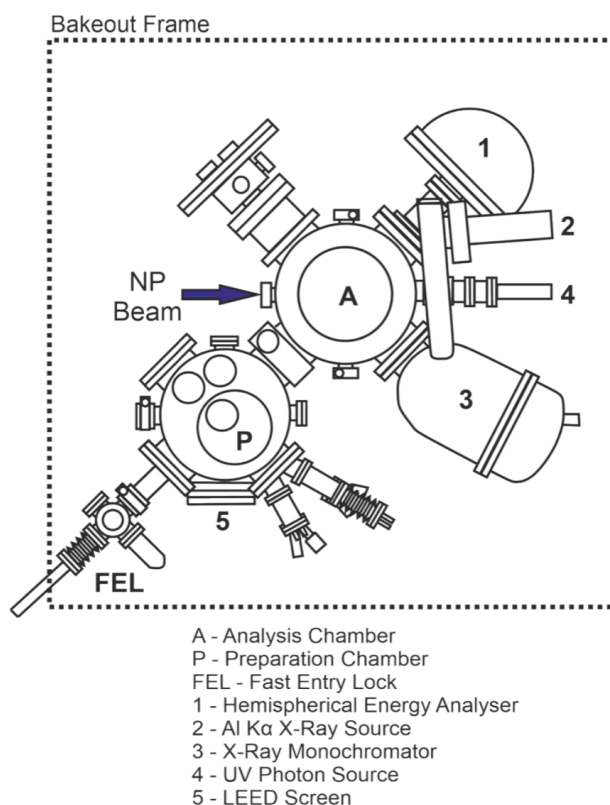


Figure 3.22: Plan view of XPS schematic used in the University of York Department of Physics [4].

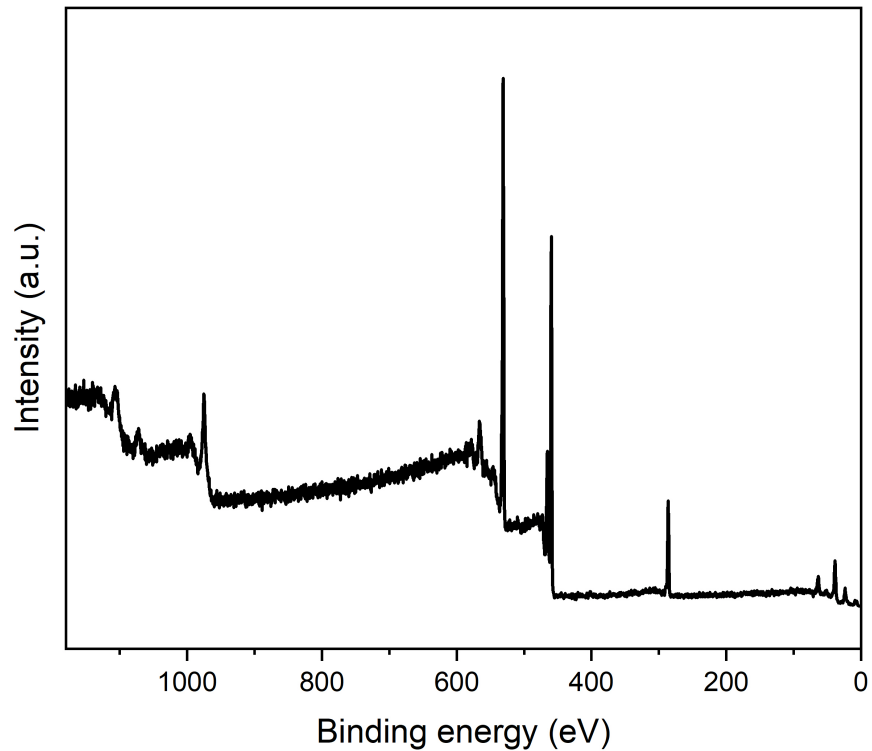


Figure 3.23: Example of a full XPS spectrum of a thin film deposited in the York Plasma Institute. The intensity of each peak is relative to that of a carbon reference species, whose peak is located between binding energy 200-300 eV. The two peaks close together at approximately 460-465 eV correspond to the Ti  $2p_{3/2}$  and  $2p_{1/2}$  electrons detected by the diagnostic, which can also be seen in figure 3.24. The peak between 500-600 eV corresponds to O  $1s$  electrons, and the peak in the 900-1000 eV range represents O electrons emitted due to the Auger effect [5].

Curve fitting is used to extract chemical information from the spectra produced, see figure 3.24 as an example. In this work, the background curve is known as a Shirley background, in which the background intensity at any given binding energy is proportional to the intensity of the total peak area above the background in the lower binding energy peak range [112,113].

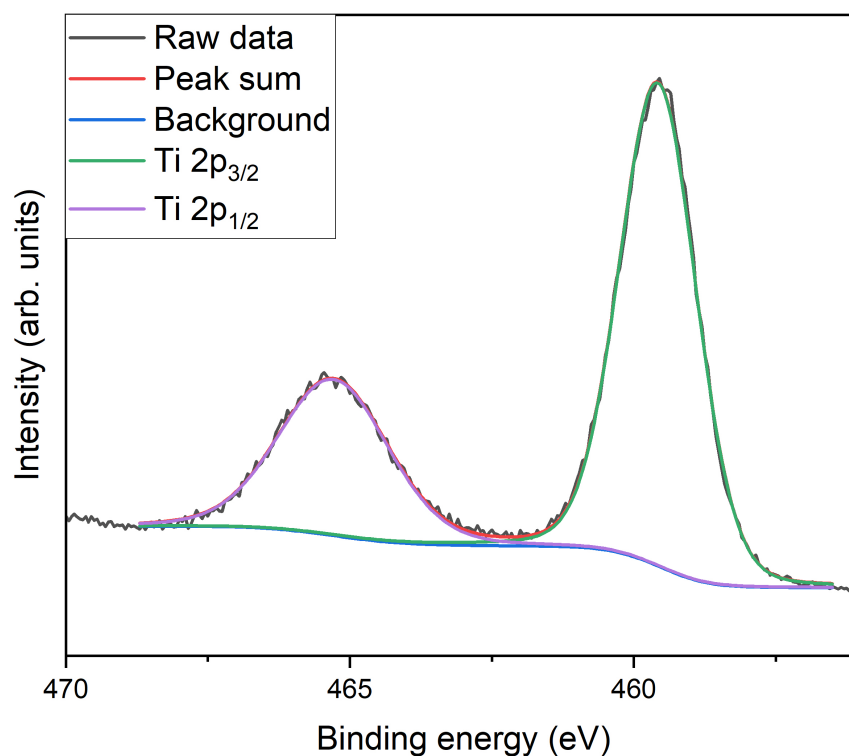


Figure 3.24: XPS figure identical to the spectrum in figure 3.23, with curve fitting on two key peaks within the 450-470 eV range. The raw data is shown by the black curve. The peak sum is the summation of all fitted peaks on top of the background. In this case, the background is a Shirley background, used to account for the effect of inelastic scattering of electrons specifically in XPS. The other two peaks in this example correspond to the Ti  $2p_{3/2}$  and  $2p_{1/2}$  electrons detected by the diagnostic.

To calculate the ratios of the species of interest, e.g. O and Ti, the normalised area under the curve of one species (e.g. oxygen) is divided by the normalised area of the other (e.g. titanium).

## Chapter 4

# Modelling laser ablation of metal targets

This first results chapter will present modelling results of the nanosecond laser ablation of six different material targets simulated using the hydrodynamic code POLLUX, as described in section 3.2. This work focuses on identifying links between material properties and specific plasma plume characteristics.

### 4.1 Laser ablation of titanium metal

As a reference point, POLLUX was used to model the laser ablation of titanium plasma plumes. Figure 4.1 contains an example of a contour plot of the distribution of the electron temperature,  $T_e$ , of a titanium plasma plume, modelled 5 ns after the laser pulse. In this work, time  $t = 0$  is defined as the time at the end of the laser pulse. The vertical and horizontal axes in each plot are  $z$ , the distance normal to the target surface (axial distance), and  $r$ , the radial distance, respectively. In figure 4.1, the plume has expanded approximately 800  $\mu\text{m}$  from the target surface, and in the radial direction the plume has expanded to roughly 600  $\mu\text{m}$  (the laser focus had a radius of 100  $\mu\text{m}$ ). Temperatures in the plasma plume reach up to approximately 6 eV in the middle of the plume. These plume sizes and electron temperatures are roughly in line with observations and modelling of plasma plumes under similar laser conditions, e.g. [52, 80, 81]. The modelled background gas density leads to unphysical predictions of increased density and temperature in the leading edge of the plume for times later than about 25 ns. However, the plasma plume densities up until this

point are much higher than the background density. Therefore, the hydrodynamic effects, which are the biggest contributor to the error following the unphysically high background density assumptions in the POLLUX modelling, will be insignificant over these short time scales of 25 ns.

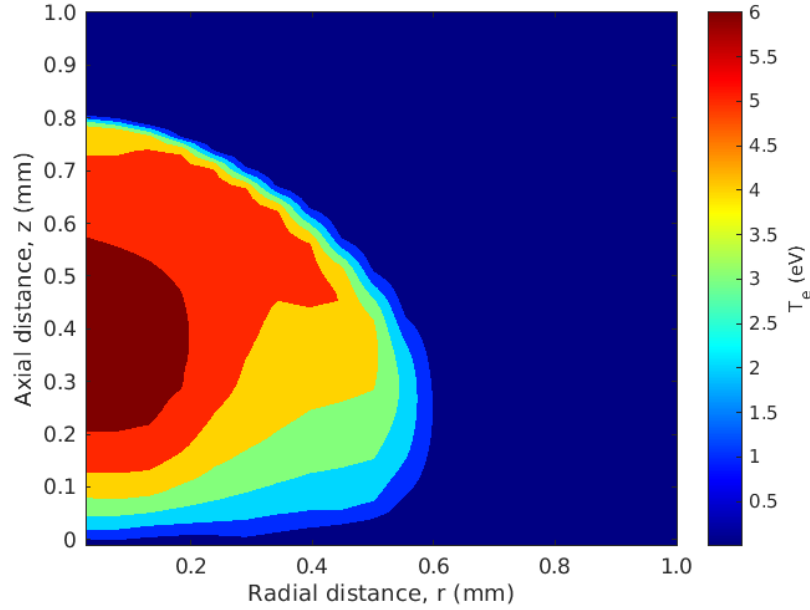


Figure 4.1: Results of the laser ablation simulation showing the distribution of the electron temperature in an ablated titanium plasma plume calculated at 5 ns after the laser pulse. The laser fluence was  $100.5 \text{ J cm}^{-2}$  and the laser focus was  $100 \text{ }\mu\text{m}$ .

Figure 4.2 displays the spatial distribution of the axial velocity and electron temperature profiles of the titanium plasma plume along the laser axis. It can be observed that the ablated material moves away from the target surface with a velocity of approximately  $5.5 \times 10^6 \text{ cm s}^{-1}$ , with the highest velocities at the leading edge of the plume. This is expected, as the material at the front of the plume will have greater kinetic energy. The electron temperature near the beginning of the plume expansion is approximately 5.5 eV. It can be seen from both plots that the axial length of the plasma plume increases over time, but at a slightly diminishing rate, possibly due to the resistance and viscosity due to the background gas. The peaks of the electron temperature and velocity in the respective plots also appear to reduce over time. These observations are qualitatively in line with many previous studies, e.g., [52,81]. However, since laser parameters (pulse duration, spot size, fluence) and material details are slightly different, it is impossible to qualitatively compare results, which is required to uncover the subtle differences between different materials.

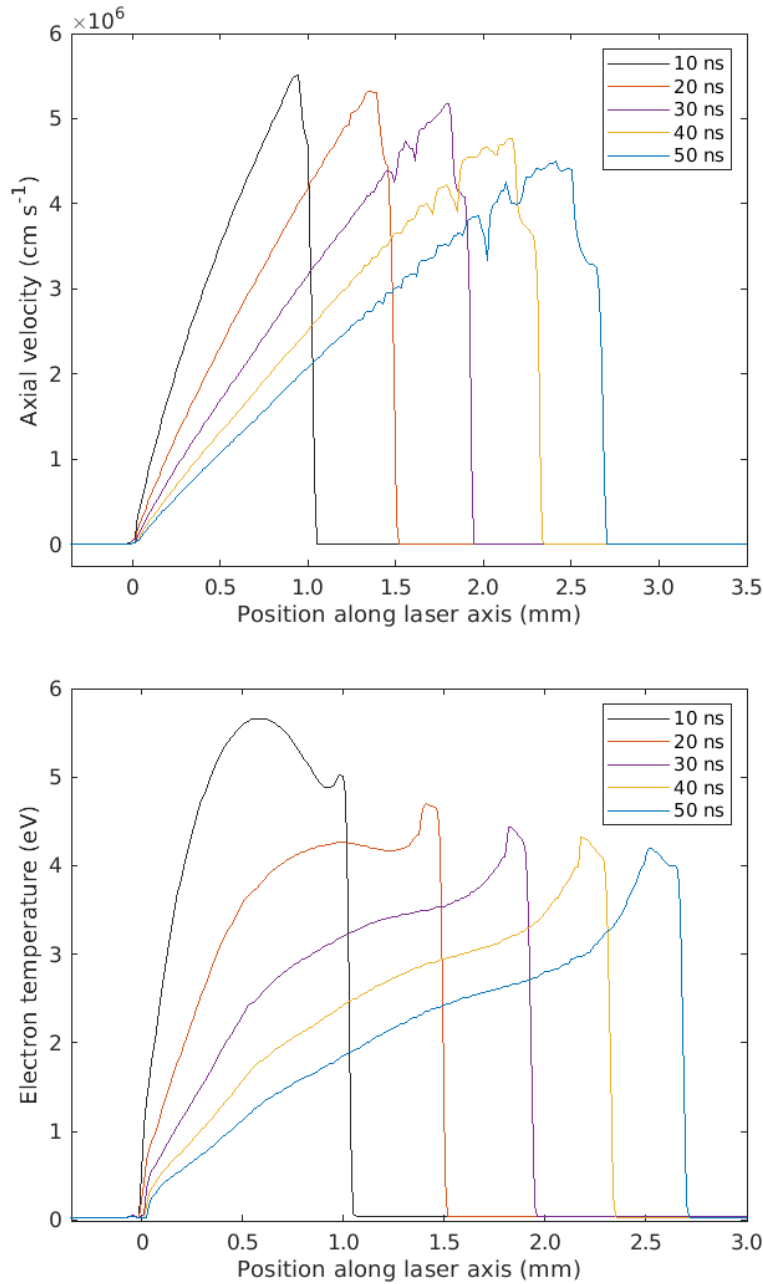


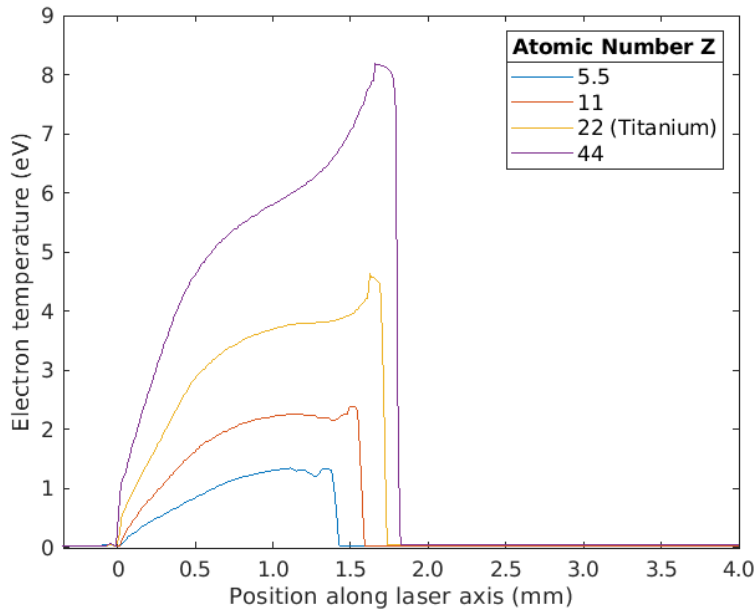
Figure 4.2: Spatial distribution of the simulated axial velocity (top) and electron temperature (bottom) profiles of a titanium plasma plume for different times after the start of the 16 ns laser pulse. The laser fluence was  $100.5 \text{ J cm}^{-2}$  and the laser focus was  $100 \text{ }\mu\text{m}$ .

## 4.2 Investigating the effects of material properties on titanium plasma plumes

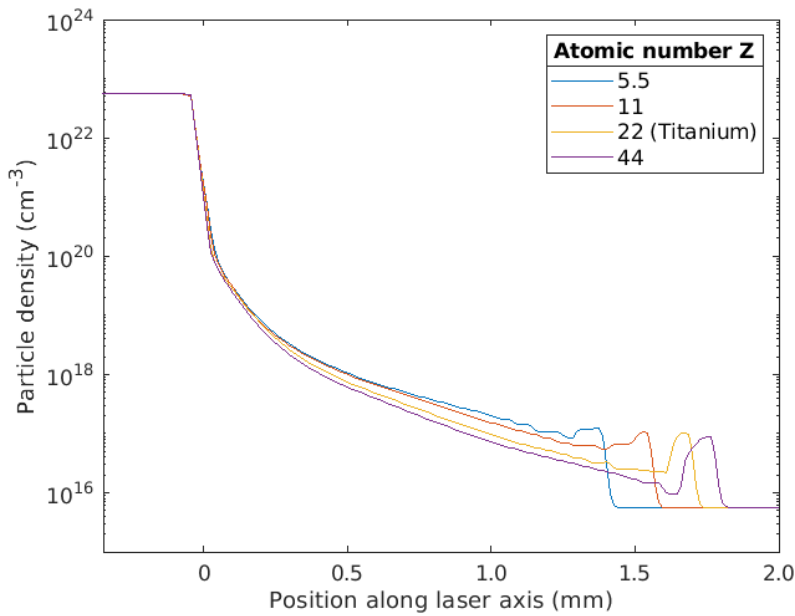
In order to truly identify which material parameters influence the plasma plume behaviour, different parameters were varied for each simulation of titanium ablation, creating non-

existing elements using the parameters for titanium as a benchmark. In each simulation, one parameter in the Chart-D EoS input for titanium was varied, whilst the other parameters were kept constant. First, the atomic number of titanium,  $Z$ , was varied in multiples of its actual atomic number (22), and the effects of this variation on the electron temperature and particle density of the plasma plume (i.e. total number density of all species in the plasma) were studied and displayed in figure 4.3. These results clearly dictate that the electron temperature and the length of the plasma plume increases with the atomic number of the material, and that the front of the plume has higher atomic density for lower atomic numbers.

The atomic number will have an effect on several processes within laser ablation, for instance in the material EoS which affects the material evaporation and ionisation state. Subsequently, the laser absorption through inverse bremsstrahlung will also be affected directly by a change in atomic number (see equations 3.1 and 3.2), and indirectly through changes in the plume properties e.g., the density  $\rho$  or ionisation state  $Z_i$ . Even though it is clear from Figure 4.3a that electron temperature increases and particle density decreases with atomic number, it is not a single process that determines this; it is a complex interplay between the different processes mentioned, resulting in the overall effects observed. Nevertheless, it is clear that a change in atomic number changes the density and temperature of the plasma plume significantly.



(a) Electron temperature



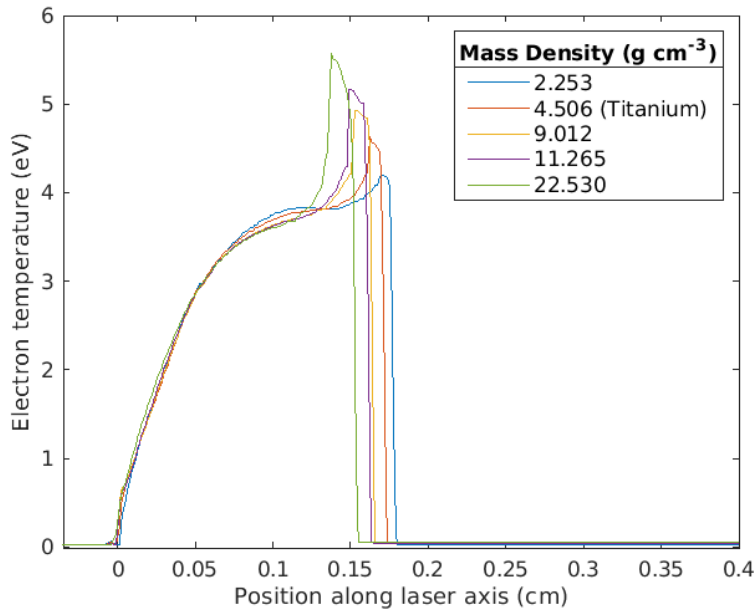
(b) Particle density

Figure 4.3: 1D plot comparing the spatial distribution of (a) the electron temperature and (b) the particle density of an ablated titanium plasma plume with varied atomic number 25 ns after the laser pulse. The default atomic number of titanium is 22. The laser fluence was  $100.5 \text{ J cm}^{-2}$  and the laser focus was  $100 \text{ }\mu\text{m}$ .

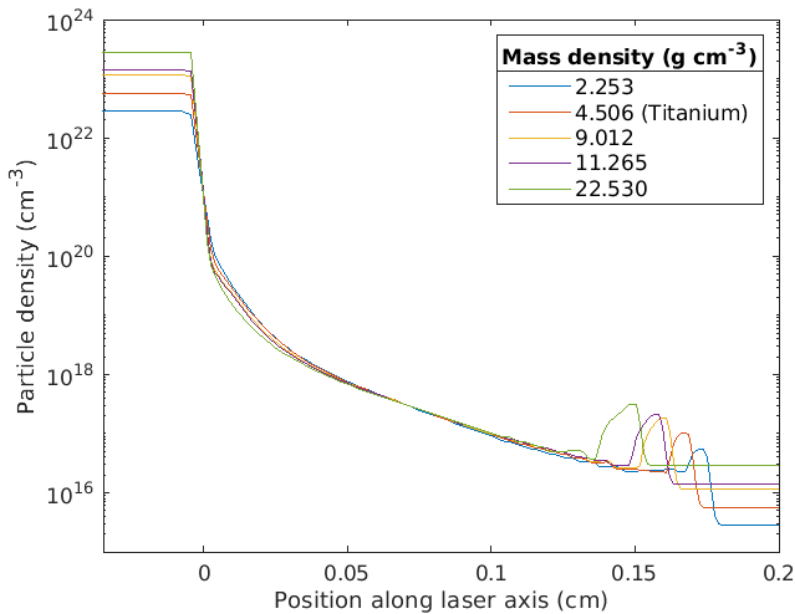
Following on from the investigations in which atomic number was varied, further simulations were performed in which the mass density,  $\rho$ , of titanium was modified in multiples

of its actual value ( $4.506 \text{ g cm}^{-3}$ ) whilst the atomic number and other parameters were kept constant, in order to investigate how the mass density of the target material contributed to the plume size and temperature. Figure 4.4a shows that for these investigations the peaks in electron temperature of the plume increased slightly with increasing target mass density. In addition, length of the plume (at the same time) is shorter as mass density increases.

However, the significance of these findings is debatable when the limitations of the model are considered. The peaks towards the front of the plume, as seen in figure 4.4b, are artefacts of the code and the need to have a non-zero background density. The phenomena responsible for the peaks is known as the ‘snowplough effect,’ in which resistance and viscosity from the background gas slows down the front of the plume as it expands into the background. As the target density is varied, the background gas density varies along with it. This means there is more background gas pressure for greater target densities, which increases the snowplough effect. The snowplough build-up gives a higher particle density, and therefore a bigger peak in figure 4.4b. Subsequently, because of the higher plasma density, inverse bremsstrahlung absorption increases (equation 3.1), resulting in a hotter plasma at the position of the density peak, see figure 4.4a. The varying background density also provides an explanation for why the plume becomes shorter with higher target density. The plume has a higher gas density to move through, so is slowed down more, resulting in shorter plumes. Therefore, it appears that the observed changes in temperature and density in the plume front are related to the background density, which is a limitation of the code, rather than the target density, which was the purpose of the investigation. In addition, the temperatures and densities behind the plume front are very similar for all target densities. Therefore, it can be concluded that the target density has limited influence on the plume properties, certainly for positions away from the plume front.



(a) Electron temperature



(b) Particle density

Figure 4.4: 1D plot comparing the spatial distribution of (a) the electron temperature and (b) the particle density of an ablated titanium plasma plume with varied mass density 25 ns after the laser pulse. The default mass density of titanium is  $4.506 \text{ g cm}^{-3}$ . The laser fluence was  $100.5 \text{ J cm}^{-2}$  and the laser focus was  $100 \text{ }\mu\text{m}$ .

Two other material parameters were investigated for their effect on the behaviour of the plasma plume: the melting temperature and the thermal conductivity coefficient. Simula-

tions were performed for each of them in a similar way to mass density and atomic number, with respective results presented in figures 4.5 and 4.6. The melting temperature, Figure 4.5, was found to have negligible effect on the plasma plume properties, with the spatial distributions of the electron temperature of the individual plots overlapping almost completely with each other. Since melting does not take place in laser ablation, these results are expected. For the variation in thermal conductivity, figure 4.6, plumes were observed to remain a similar size. However, the electron temperature distribution within the plasma plume itself appeared to change slightly with less flat profiles for higher conductivity. This is to be expected, as materials with higher thermal conductivity allow for quicker redistribution of heat within their respective plasma plumes. The plasma density was shown not to vary with changes in either melting temperature nor thermal conductivity.

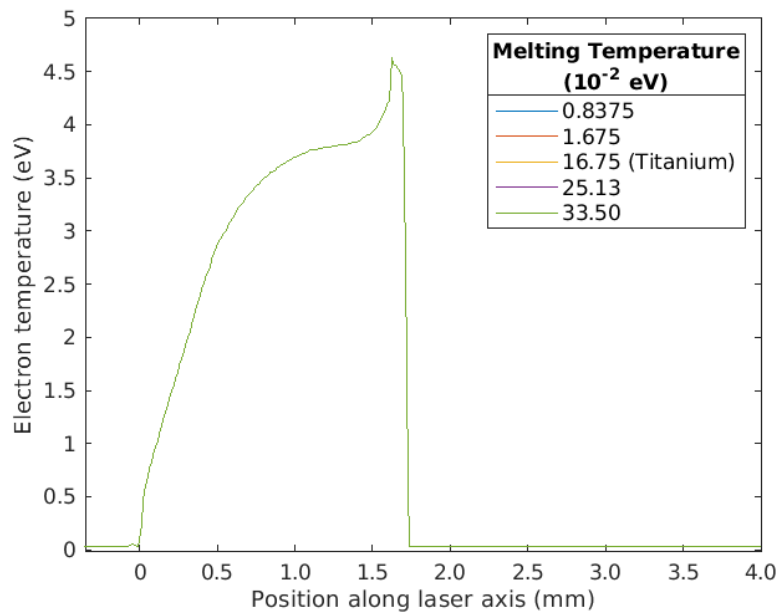


Figure 4.5: Comparison of the spatial distribution of the electron temperature of an ablated titanium plasma plume with varied melting temperature 25 ns after the laser pulse. The default melting temperature of titanium is 1.675 meV. The laser fluence was  $100.5 \text{ J cm}^{-2}$  and the laser focus was  $100 \text{ }\mu\text{m}$ .

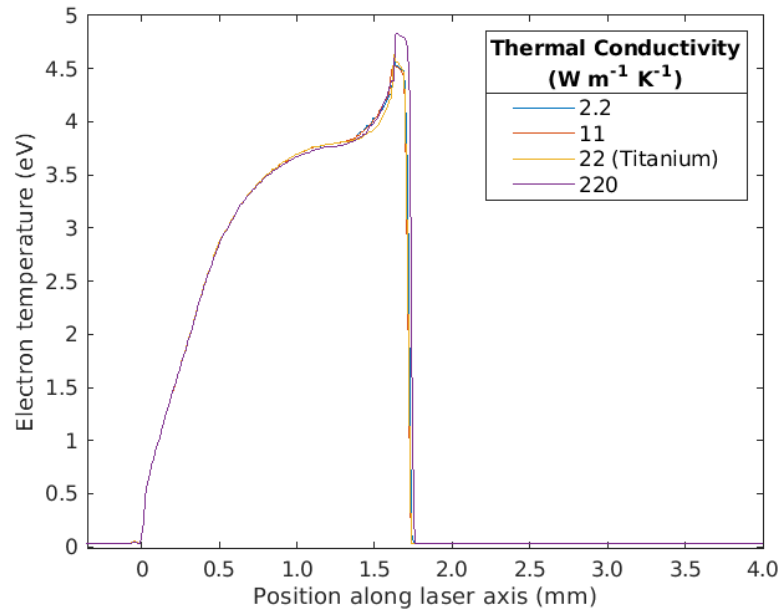


Figure 4.6: Comparison of the spatial distribution of the electron temperature of an ablated titanium plasma plume with varied thermal conductivity coefficient 25 ns after the laser pulse. The default thermal conductivity of titanium is  $22 \text{ W m}^{-1}\text{K}^{-1}$ . The laser fluence was  $100.5 \text{ J cm}^{-2}$  and the laser focus was  $100 \mu\text{m}$ .

### 4.3 Comparison of the laser ablation of plasma plumes from different materials

With the knowledge gained from investigating the effects of individual material parameters on plasma plumes, the laser ablation of six real materials was simulated, as outlined in section 3.2.

Figure 4.7 contains the simulated electron temperature of the six plasma plumes 25 ns after the laser pulse. Here, the peak temperatures of the plumes varied between 2.61-10.9 eV, with aluminium having the coolest peak and tantalum having the hottest. Moreover, the peak temperatures, and the shape of the temperature distribution, are strongly correlated to the atomic number variation in figure 4.3, e.g. Al ( $Z=13$ ) has a peak around 2 eV, similar to the peak electron temperature of the  $Z=11$  curve. It shows that the temperature profiles of the different elements are closely related to the atomic number of the target material. Similarly, figure 4.8 contains the simulated particle density of the six plasma plumes 25 ns after the laser pulse, with the materials of smaller atomic number such as aluminium

producing plumes with higher particle densities, showing direct correlation to results in figure 4.3b, where only atomic number was changed.

Interestingly, Au, Ta (highest atomic number and mass density) and Al (lowest atomic number and mass density) have similar plume lengths that are shorter than the other elements. The investigations in section 4.2 show opposing trends for plume length with atomic number and target mass density; plume length increases with atomic number and decreases with increasing mass density. The results in figure 4.7 do not show a clear trend with either, indicating a more complex interplay between the two properties. It is again noted, that the change in target mass density also changes the background gas density, which may affect the plume expansion dynamics. Experimental verification of the results is required to determine the accuracy of the plume length predictions from the model. Nevertheless, from these investigations, it is clear that atomic number has the biggest impact on the plasma plume, with increasing electron temperature and decreasing density with increasing atomic number. The mass density, melting temperature, and thermal conductivity coefficient of the material have only a very limited influence on the plume behaviour.

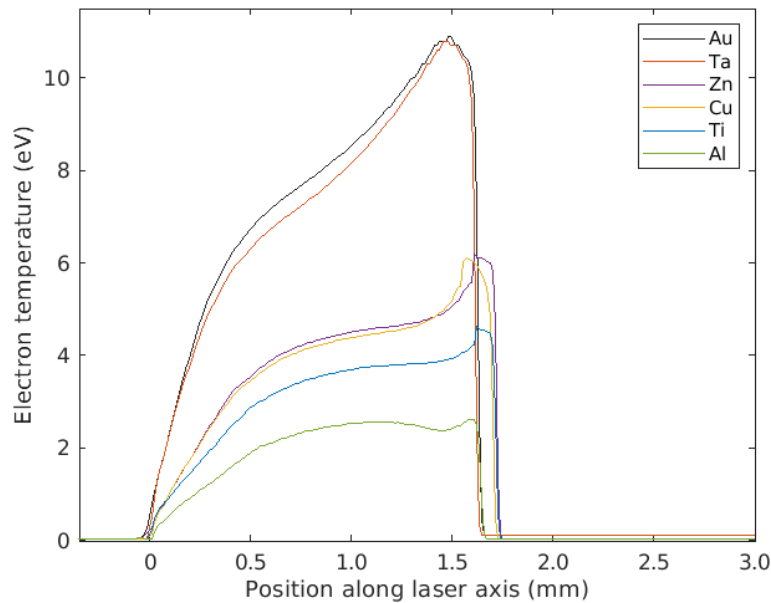


Figure 4.7: The spatial distribution of the electron temperature of plasma plumes from six different materials, 25 ns after the laser pulse. The laser fluence was  $100.5 \text{ J cm}^{-2}$  and the laser focus was  $100 \mu\text{m}$ .

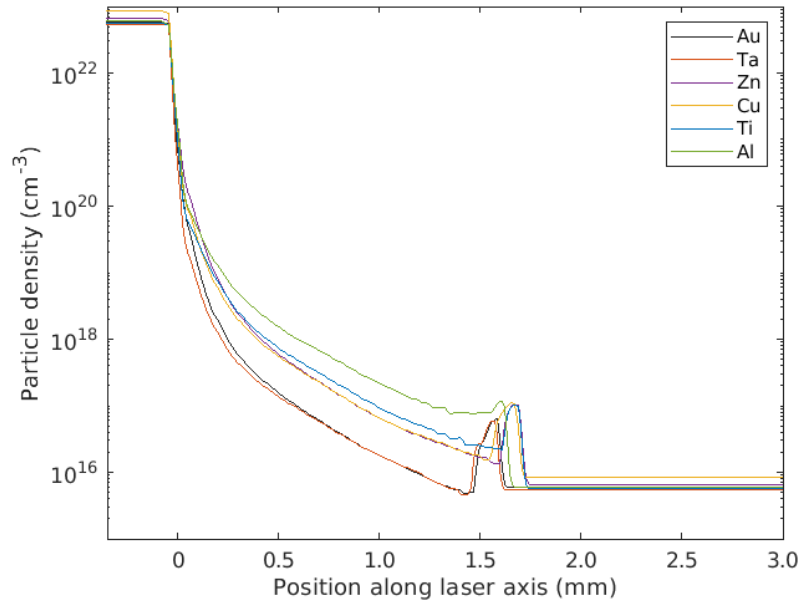


Figure 4.8: The spatial distribution of the particle density of plasma plumes from six different materials, 25 ns after the laser pulse. The laser fluence was  $100.5 \text{ J cm}^{-2}$  and the laser focus was  $100 \mu\text{m}$ .

#### 4.4 Conclusions

In this chapter, the laser ablation of different metals was modelled using the hydrodynamic code POLLUX. In particular, the material properties which contribute to the characteristics of the plasma plumes were investigated. This was carried out in two parts: first, titanium was modelled as a benchmark after which single material parameters were varied (creating non-existing ‘Ti-variant’ materials), in order to investigate the link between these parameters and the plasma plume properties. Secondly, the evolution of electron temperature and particle density of plumes of six real elements varying in atomic number and mass density was modelled to verify the links identified in the work on non-existing materials. The results from modelling the titanium-variants showed that the atomic number of the material,  $Z$ , affected the electron temperature and mass density of the subsequent plasma plume, with both parameters increasing with atomic number. Conversely, the mass density, thermal conductivity, and melting temperature appeared to have no effect on the electron temperature or particle density of the bulk of the plumes. These correlations were observed in the modelling of real elements, with the heavier elements with higher atomic number and mass

density giving rise to hotter, denser plasma plumes. The length of the plume was not directly correlated to a single material parameter; there was an interplay between atomic number and mass density effects, with the heaviest and lightest elements producing shorter plumes compared to the elements with intermediate values for atomic number and mass density.

Since kinetic energy  $E_k = \frac{1}{2}mv^2$ , plasma plumes arising from lighter metals will have higher velocity when energy is applied to the plume by the laser. Increasing the mass of the target results in a greater number of electrons to be coupled via inverse bremsstrahlung. It is likely the atomic number dictates the coupling of energy, and the mass density of the metal dictates how far the plume expands.

Overall, the results in this chapter have shown that the atomic number of the target material has the biggest influence on the temperature and density of the plasma plume, providing useful insights for experimental situations such as PLD where the aim is to change the target material, but with the plume parameters kept as constant as possible.

## Chapter 5

# Characterising atomic O and N densities in a low-pressure O<sub>2</sub>/N<sub>2</sub> plasma

This chapter will present work from characterising the O<sub>2</sub>/N<sub>2</sub> background plasma using the spectroscopy diagnostic, TALIF, as outlined in section 3.3. The work focuses on identifying the desired amount of atomic oxygen and atomic nitrogen densities to achieve stoichiometric oxynitride thin films. This is done by characterising the mix of reactive oxygen and nitrogen plasma species, represented by atomic O and N, under a variation of operational parameters in order to give an operational range for tuning the O/N reactive plasma content.

### 5.1 Atomic density of pure oxygen

The first TALIF experiments involved measuring the density of atomic oxygen species in a pure oxygen plasma as a function of applied RF power and GEC chamber pressure. As with the POLLUX parameters in chapter 4, the parameters investigated in TALIF were varied in turn. During power scans, the RF power was varied from 200-700 W in steps of 100 W whilst pressure in the chamber was kept constant at 20 Pa. During pressure scans, the pressure was varied between 15-40 Pa in steps of 5 Pa, while the RF power was kept constant at 600 W. As described in section 3.3, at each individual step, the energy of the laser was measured, and a wavelength and lifetime scan was performed. The iCCD camera gate was programmed on the DDG to trigger 700  $\mu$ s in the afterglow of the plasma pulse, to keep

consistent with the afterglow time for the nitrogen measurements (see section 5.2 for why this afterglow time was chosen). Once all measurements were taken for each scan, the atomic density was calculated using a TALIF Analysis code developed in Python at the University of York by M. Kellermann-Stunt as part of his PhD research, and the evolution of atomic density of oxygen was plotted with respect to power and pressure, see figures 5.1 and 5.2. In each of the plots in this chapter, the uncertainties of the atomic density values were derived by adding each term in equation 3.8 in quadrature, as discussed in section 3.3.5.

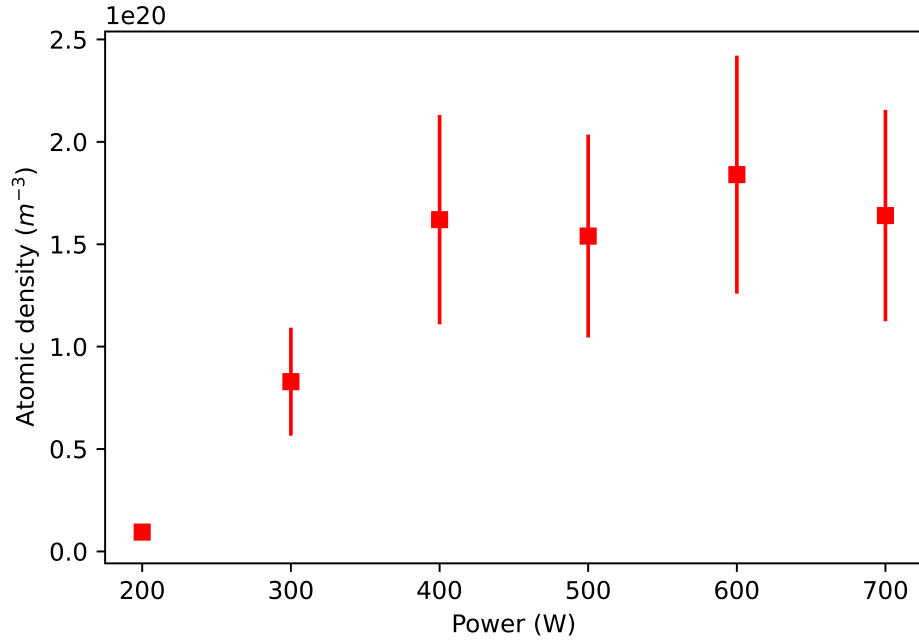


Figure 5.1: The evolution of atomic density of a pure oxygen plasma with respect to applied radiofrequency power. GEC chamber pressure is fixed at 20 Pa and images are taken  $700 \mu s$  in the afterglow of the plasma pulse.

From the pure oxygen power and pressure scans in figures 5.1 and 5.2, the atomic density increases with power and pressure. In fig. 5.1, the atomic density increases from about  $1.0 \times 10^{19} m^{-3}$  at 200 W RF power to between  $1.5-2.0 \times 10^{20} m^{-3}$  from 400-700 W. This exhibits a trend similar to previous TALIF work performed by Mo, as seen in figure 4.6a of [114], in which the increase in atomic density between 500-700 W (and slightly beyond) is similarly weak. Furthermore, the results in figure 5.1 are similar to the work done by Taylor and Tynan, who used actinometry and atomic mass spectroscopy instead of TALIF to measure the atomic density, which increased from  $1.3 \times 10^{18}$  to  $2.0 \times 10^{18} m^{-3}$  between 300-2000 W at 10 mTorr (1.3 Pa). In figure 5.2, the atomic density increases linearly from

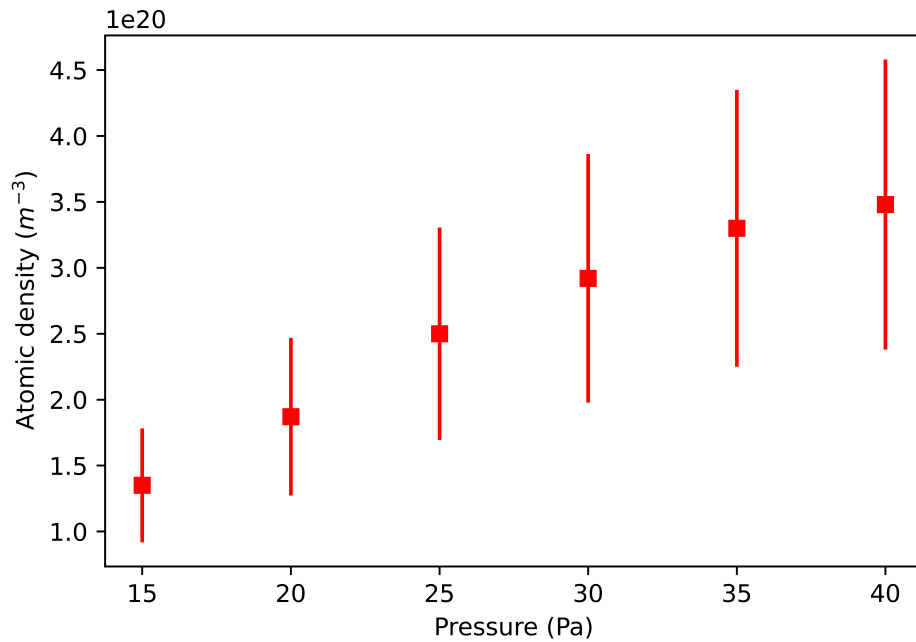
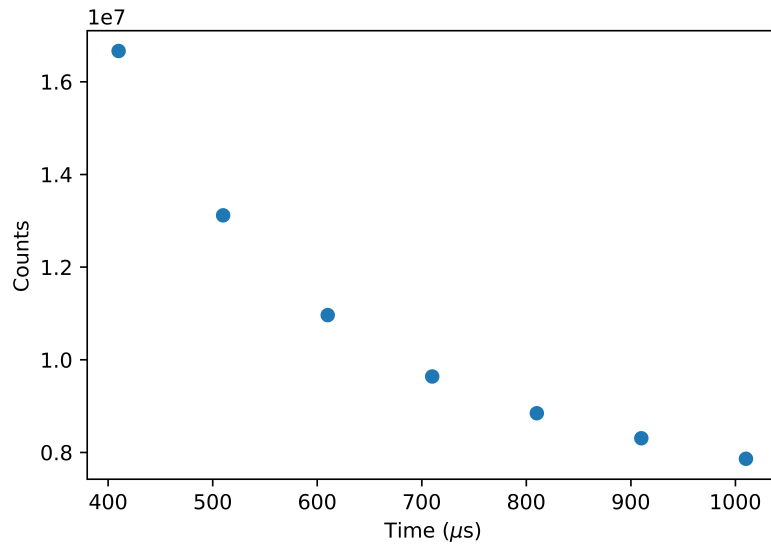


Figure 5.2: The evolution of atomic density of a pure oxygen plasma with respect to GEC chamber pressure. Applied radiofrequency power is fixed at 600 W and images are taken 700  $\mu$ s in the afterglow of the plasma pulse.

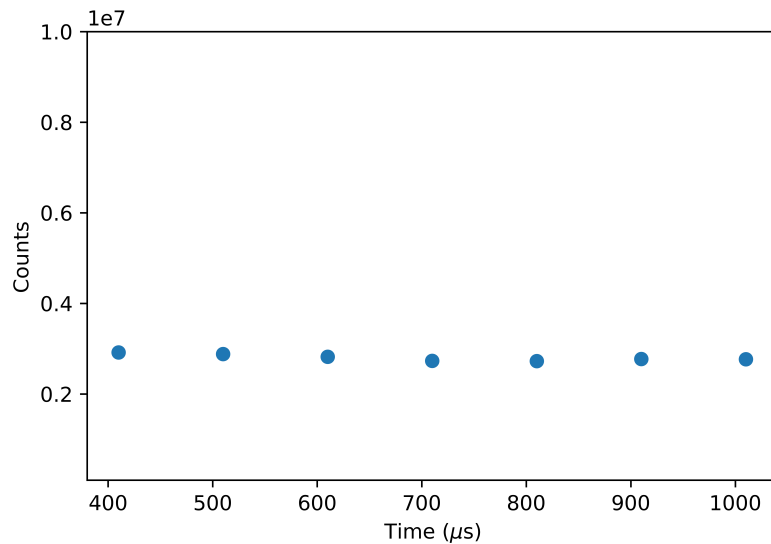
approximately  $1.5 \times 10^{20} \text{ m}^{-3}$  to about  $3.5 \times 10^{20} \text{ m}^{-3}$  as the pressure increases from 15-40 Pa. Once again, this is consistent with work from Mo (see figure 4.7a of [114]), and also from Hsu et al. [115], who see an increase from  $2.5 \times 10^{18}$  to  $1.75 \times 10^{19} \text{ m}^{-3}$  using mass spectrometry. Furthermore, Taylor and Tynan, Corr et al. and Gudmundsson et al. all document similar correlations between atomic oxygen density and pressure, albeit between pressure ranges between 5-100 mTorr [116–118]. By increasing the pressure, the concentration of oxygen within the chamber increases, meaning an increasing number of oxygen molecules will be dissociated into atomic oxygen by the electrons originating from the RF, resulting in the clear, linear increase in atomic density with pressure. However, by increasing the applied power, the electron density within the chamber increases, while the amount of oxygen remains the same. This also results in more dissociation, but the amount of oxygen gas to be dissociated remains unchanged. Further, the increased RF power results in higher gas temperatures, which in turn results in lower oxygen density if the same amount of oxygen gas is dissociated in the chamber. Both of these circumstances result in the diminishing increase in atomic density at higher powers, as can be observed between powers 400-700 W.

## 5.2 Atomic N density of pure nitrogen

Obtaining fluorescence signals of nitrogen plasmas proved to be a much bigger challenge than for oxygen. The radiation emitted from the relaxation of nitrogen plasma species from excited electronic states (known simply as plasma emissions) can be so strong that they can sometimes obstruct the fluorescence, which has been a common occurrence with nitrogen plasma in TALIF [119, 120] and can be overcome by measuring at substantial times later on in the afterglow of the plasma pulse. The technique of measuring in the afterglow works because the plasma light emission will fall very quickly (e.g. in hundreds of microseconds, as seen in figure 5.3a), while the fluorescence signal stays relatively constant on such time scales (figure 5.3b). As such, the time at which the iCCD took images of the GEC chamber was set to 700  $\mu\text{s}$  after the end of the nitrogen plasma pulse, when the nitrogen plasma emissions were less overwhelming and the fluorescence signal remained visible. The atomic density calculated by the analysis script at this time after the end of the plasma pulse could be extrapolated back to what the values were estimated to be at the very end of the plasma pulse, but measurements showed negligible decrease in atomic density between the end of the pulse and 700  $\mu\text{s}$  afterwards.



(a) Nitrogen plasma decay



(b) Evolution of nitrogen fluorescence in plasma afterglow

Figure 5.3: (a) Decay of atomic nitrogen plasma at 20 Pa GEC chamber pressure and 600 W RF power; (b) background-subtracted fluorescence counts in the plasma afterglow. Uncertainties in counts were derived from the square root of the number of counts.

The steps outlined in section 5.1 for measuring the atomic density of pure oxygen plasma were repeated for pure nitrogen plasma. From the nitrogen scans in figures 5.4 and 5.5, the atomic density once again increases with power and pressure. Comparing figures 5.1 and 5.5, the atomic nitrogen densities are higher than atomic oxygen by varying factors, with the largest factor being at 700 W, where the atomic nitrogen density is over 5 times greater than that of oxygen at the same power, and the smallest factor being at 300 W, in

which the atomic nitrogen density is only higher than atomic oxygen by a factor of about 1.75. Meanwhile, comparing figures 5.2 and 5.5, the difference between atomic nitrogen and oxygen densities decreased with pressure, despite atomic nitrogen densities remaining higher overall. At 15 Pa, the atomic nitrogen density was about 5 times greater than atomic oxygen, and this factor decreased with power, with the atomic nitrogen density being approximately a factor of 2.88 higher than atomic oxygen at 35 Pa.

As with  $O_2$ , increasing the RF power increases the electron density, resulting in increased atomic density of nitrogen plasma due to dissociation of  $N_2$ . Interestingly, the increase in atomic density does not seem to diminish at higher powers for atomic nitrogen, and there is very little increase with pressure. The difference between the progressions shown in figures 5.1 and 5.4, and between figures 5.2 and 5.5 is most likely because the electron density in oxygen plasmas is typically several factors of 10 greater than nitrogen plasmas under equal pressures, according to electron energy distribution function (EEDF) measurements by E.I. Toader [121]. Even when the power of the nitrogen discharge plasma was double that of the oxygen discharge plasma, the natural logarithm of the electron energy probability function (EEDF) for nitrogen still remained many factors of 10 below that for oxygen. In other literature, electrons have been shown to lose a lot more energy in vibrational excitation of nitrogen, such as in work done by Guerra et al. [122], which could further explain the difference in progressions between the pure oxygen and nitrogen TALIF measurements in this work.

### 5.3 Atomic density of oxygen and nitrogen plasma admixtures

To deposit metal oxynitride thin films, an admixture composed of oxygen and nitrogen plasma is generated in the chamber. Initially, the flow for each of the gases was set to 5.00 sccm, giving an equal (50/50) amount of oxygen and nitrogen content in the chamber, and power and pressure scans were performed in a similar manner to sections 5.1 and 5.2. Due to the TALIF setup, the fluorescence of only one species can be measured at a time, meaning separate scans were performed: a power and pressure scan in which the laser conditions required to observe oxygen fluorescence were used, then repeated with the laser conditions for nitrogen fluorescence, as shown in figures 5.6-5.9.

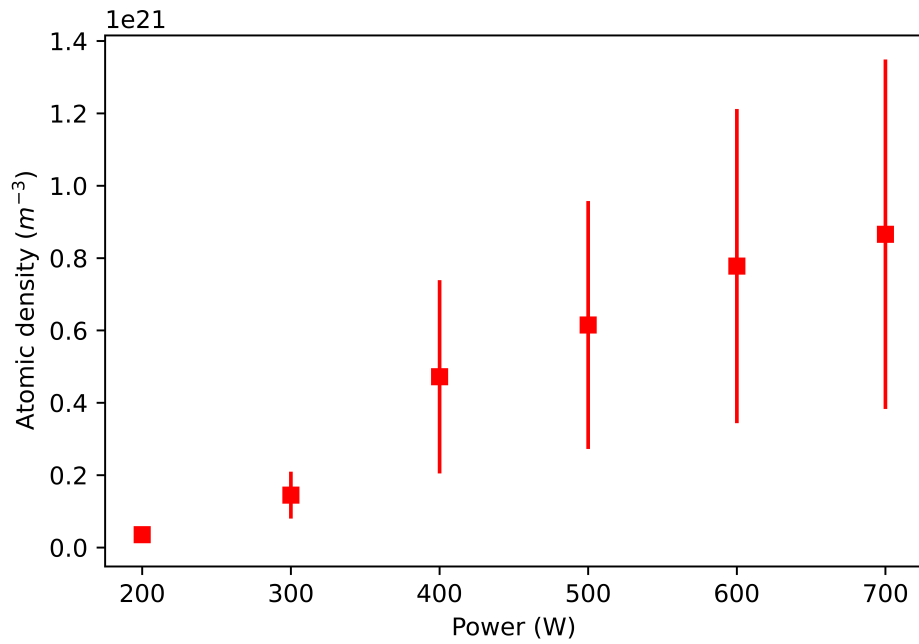


Figure 5.4: The evolution of atomic density of a pure nitrogen plasma with respect to applied radiofrequency power. GEC chamber pressure is fixed at 20 Pa and images are taken  $700 \mu s$  in the afterglow of the plasma pulse.

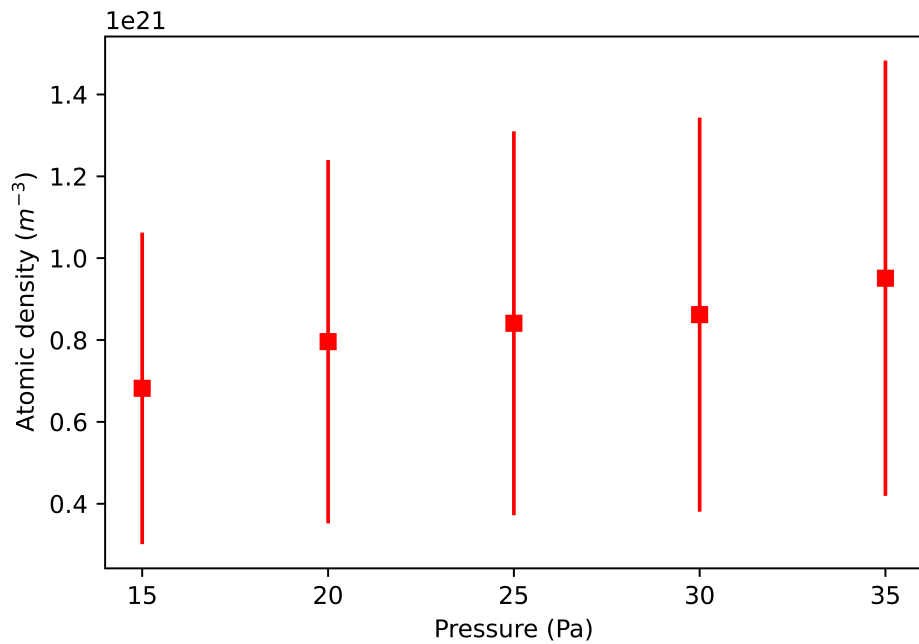


Figure 5.5: The evolution of atomic density of a pure nitrogen plasma with respect to GEC chamber pressure. Applied radiofrequency power is fixed at 600 W and images are taken  $700 \mu s$  in the afterglow of the plasma pulse.

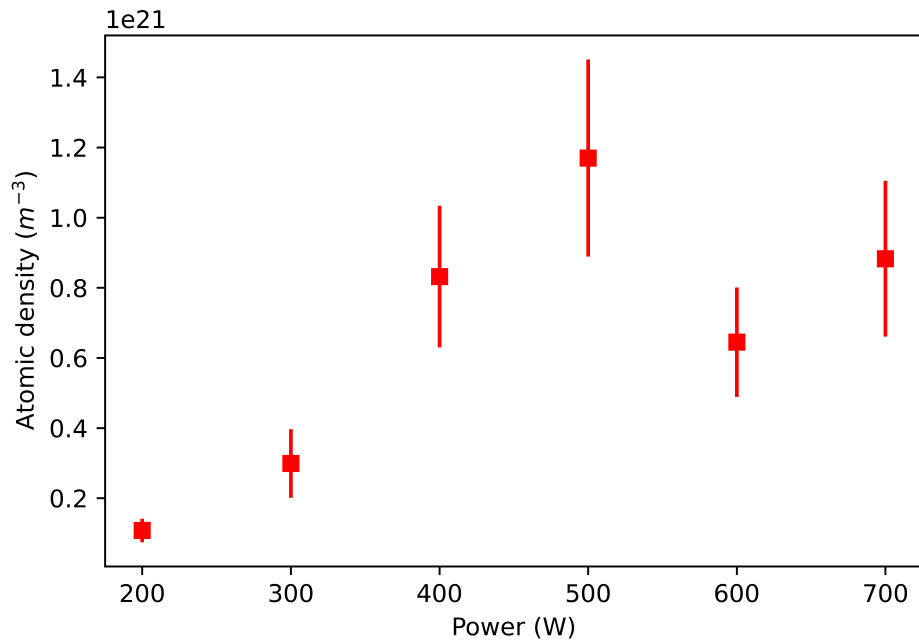


Figure 5.6: The evolution of atomic density of oxygen in a 50/50 oxygen and nitrogen plasma admixture with respect to applied radiofrequency power. Chamber pressure is fixed at 20 Pa and images were taken 700  $\mu s$  in the afterglow of the plasma pulse.

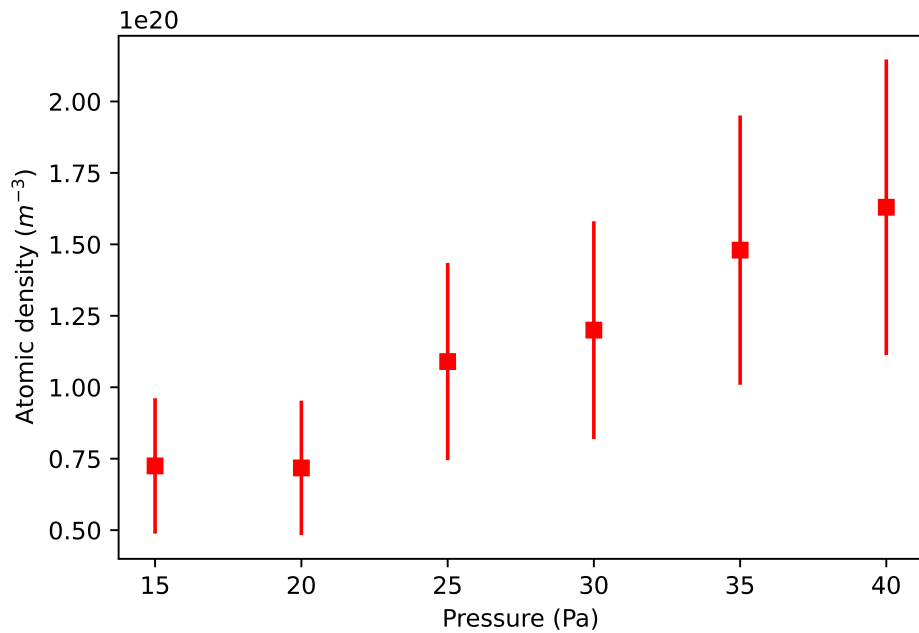


Figure 5.7: The evolution of atomic density of oxygen in a 50/50 oxygen and nitrogen plasma admixture with respect to GEC chamber pressure. The applied radiofrequency power is fixed at 600 W and images are taken 700  $\mu s$  in the afterglow of the plasma pulse.

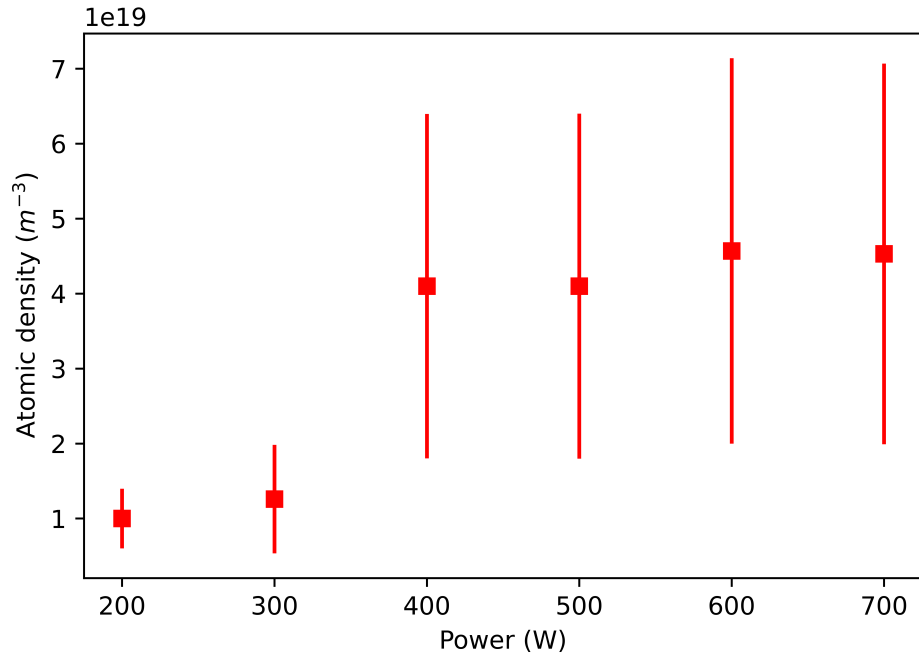


Figure 5.8: The evolution of atomic density of nitrogen in a 50/50 oxygen and nitrogen plasma admixture with respect to applied radiofrequency power. GEC chamber pressure is fixed at 20 Pa and images are taken  $700 \mu s$  in the afterglow of the plasma pulse.

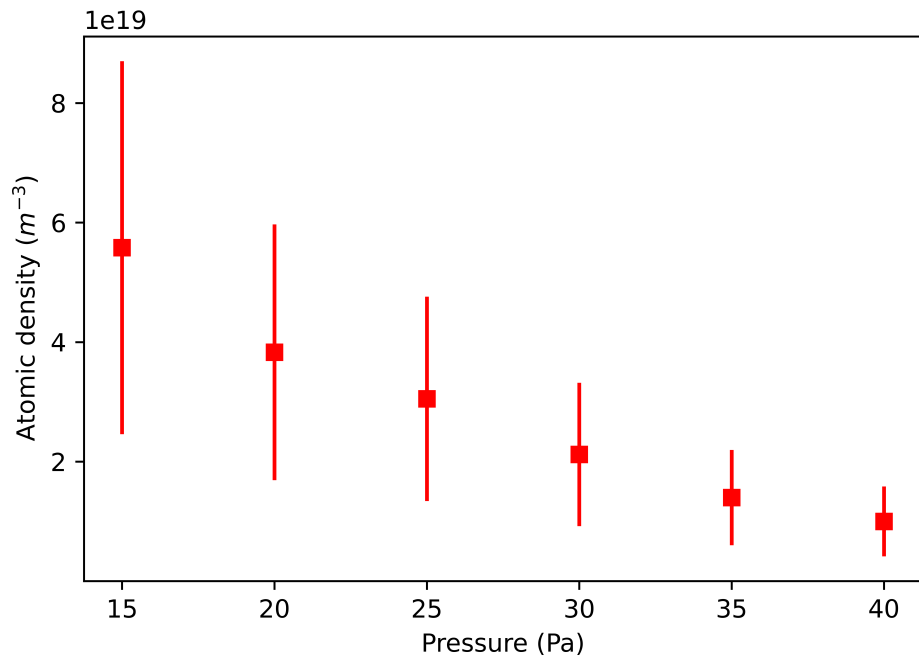


Figure 5.9: The evolution of atomic density of nitrogen in a 50/50 oxygen and nitrogen plasma admixture with respect to pressure. Applied radiofrequency power was set to 600 W and images were taken  $700 \mu s$  in the afterglow of the plasma pulse.

As with the pure oxygen plasma, the density of atomic oxygen in the 50/50 admixture increased with power and pressure (figs 5.6 and 5.7). However, the atomic density of oxygen in the admixture was much greater than with pure oxygen as the power increased, and about half when pressure changed. The density of O is approximately  $10^{20} \text{ m}^{-3}$  throughout, which is similar to what is observed in the pure  $\text{O}_2$  plasma (figure 5.2), but slightly lower, possibly due to oxygen making up about half the total gas content this time.

As seen in figure 5.8, the atomic density of nitrogen increased with power, with a noticeably larger rise in density between 300 and 400 W. This is likely due to the E-H mode transition lying at approximately 370 W for plasmas in the GEC cell.

Figure 5.9 shows the atomic density of nitrogen decreased as pressure was increased – a noticeable contrast compared to pure nitrogen and oxygen, and even oxygen in  $\text{O}_2/\text{N}_2$  admixtures, in which the density had always been observed to increase in each case. What is observed here in figure 5.9 is likely due to complex chemistry between oxygen and nitrogen plasmas. According to figure 8 in [123], as the pressure in K. Katsonis and C. Berenguer’s ICP mode plasma reactor increased, the density of  $\text{N}_2\text{O}$  increased while N decreased, and the density of O species either increased or decreased depending on excited state. This suggests the possibility that  $\text{N}_2\text{O}$  is being produced at higher pressures, reducing the N content as a result. Further, the atomic nitrogen density here in figure 5.9 appears to be within an order of magnitude of  $10^{19} \text{ m}^{-3}$  throughout, which is a dramatic difference to that observed in pure  $\text{N}_2$  (figure 5.5), where the density varies between about  $(6.8 - 9.5) \times 10^{20} \text{ m}^{-3}$ . This suggests further possibility that there is some chemistry taking place between the two plasma species. Many different chemical reactions may be occurring within the chamber, leading to many different products, including  $\text{NO}_x$  gases produced by Zel’dovich mechanism reactions, as well as  $\text{O}_3$  produced by ozone formation mechanism reactions [122, 124].

In interest of achieving optimal thin film stoichiometry, an admixture scan was performed to examine how the ratio of oxygen to nitrogen content in the plasma admixture affected the atomic density of the two species. The flow of the oxygen and nitrogen gas entering the chamber was varied while keeping the overall pressure constant at 20 Pa, with the applied RF power fixed at 600 W. This was done by changing the set points on the mass flow controller. The following ratios of oxygen:nitrogen were used: 10:90; 25:75; 40:60; 50:50; 60:40; 75:25; 90:10. Since measurements for both oxygen and nitrogen cannot be undertaken simultaneously, separate scans had to be taken, focusing on either O or N respectively,

keeping all other conditions the same. When oxygen made up 10% of the admixture, it was assumed that nitrogen made up 90%. The resulting plot is seen in figure 5.10. Here, the atomic density of both species increased as the percentage content of the respective species entering the chamber increased, as expected. The density of atomic oxygen at 10:90 O:N ratio is similar to that of atomic nitrogen at a 90:10 O:N ratio. However, the density of atomic nitrogen rapidly increases with relative flow input compared to that of atomic oxygen, and the atomic N density at a 10:90 O:N ratio is approximately double the atomic O density at a 90:10 ratio. Once again, this difference is likely due to complex chemistry between the oxygen and nitrogen interactions within the chamber. Burnette et al. reported that two of the most dominant thermal reactions in the afterglow of oxygen/nitrogen LTPs were the reverse of the Zel'dovich reaction  $\text{NO} + \text{N} \rightleftharpoons \text{N}_2 + \text{O}$ , and the ozone formation reaction  $\text{O} + \text{O}_2 + \text{M} \rightarrow \text{O}_3 + \text{M}$  (where M is a gas molecule e.g.  $\text{N}_2$  or  $\text{O}_2$ ). The rate coefficient for the reverse Zel'dovich reaction is almost 5 times greater than that of the ozone formation reaction, which could contribute to the larger number density of atomic nitrogen species over atomic oxygen [124].

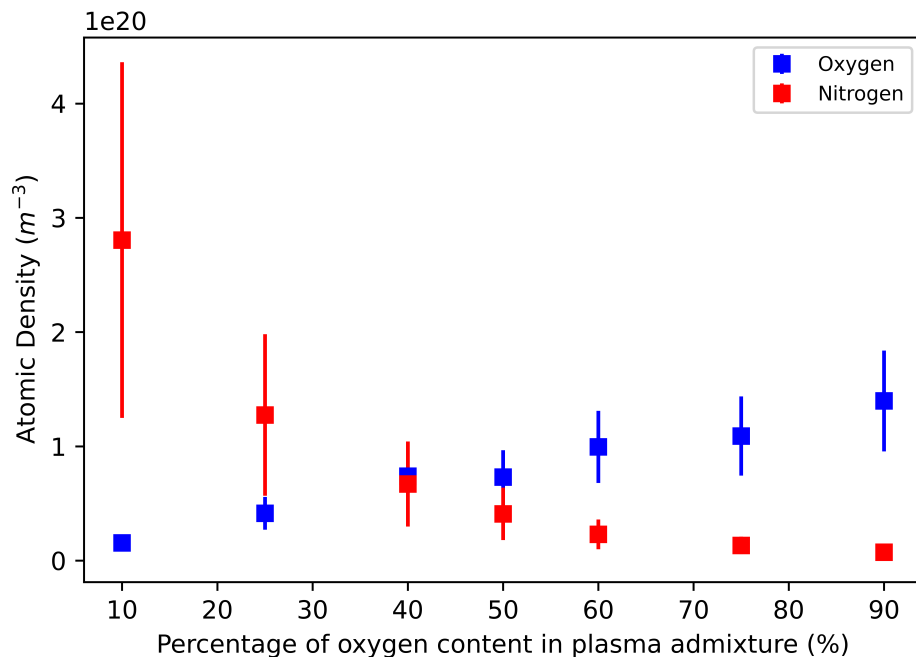


Figure 5.10: The evolution of atomic density of oxygen and nitrogen with respect to percentage mix of oxygen content in an oxygen and nitrogen plasma admixture. The applied radiofrequency power was set to 600 W, the total pressure of the GEC chamber was set to 20 Pa, and images were taken 700  $\mu\text{s}$  in the afterglow of the plasma pulse. When the oxygen mix is 10%, the nitrogen mix is assumed to be 90%, and so on.

Observing how the ratio of the atomic oxygen density to atomic nitrogen density changes with power, pressure, and percentage mix can give an idea about the range in O/N that can be achieved in the plasma, which can subsequently be used to tune the O/N thin film content in PE-PLD. Figure 5.11 showed an unclear correlation between the O/N density ratio and applied RF power, with relatively small variations between  $12 \pm 7$  to  $32 \pm 23$ , an approximate range of factor 3. Figure 5.12 showed a much clearer, near-quadratic interrelationship between the O/N density ratio and chamber pressure, with the ratio varying between about  $1.3 \pm 0.8$  to  $16 \pm 11$  between selected pressures, i.e. a range of about factor 10. However, it is clear that the percentage content of the species in the plasma mixture is the parameter that provides the most control over the density ratio, as shown in figure 5.13. Here, the O/N density ratio changes on a logarithmic scale, varying between 0.05-81.95 (An approximate range of factor 1500), peaking at 75% oxygen and 25% nitrogen.

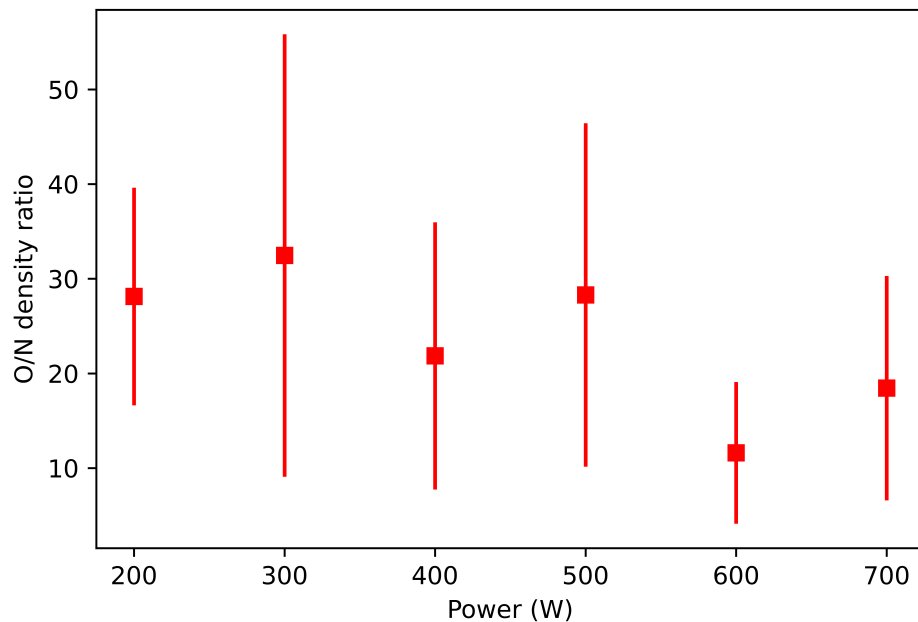


Figure 5.11: The evolution of the ratio of the atomic density of oxygen and nitrogen with respect to applied RF power in an oxygen and nitrogen plasma admixture. The total chamber pressure was set to 20 Pa and images were taken  $700 \mu\text{s}$  in the afterglow of the plasma pulse.

## 5.4 Conclusions

In this chapter, the  $\text{O}_2:\text{N}_2$  background plasma in PE-PLD was characterised using the TALIF diagnostic. This was done by verifying the ground-state atomic density of pure oxygen

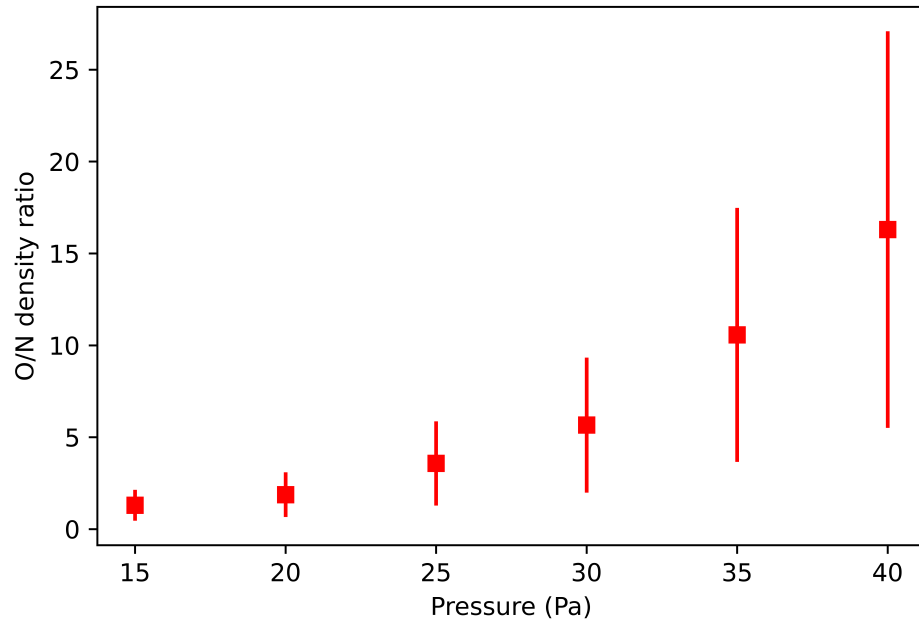


Figure 5.12: The evolution of the ratio of the atomic density of oxygen and nitrogen with respect to GEC chamber pressure in an oxygen and nitrogen plasma admixture. The applied radiofrequency power was set to 600 W and images were taken 700  $\mu$ s in the afterglow of the plasma pulse.

plasma, pure nitrogen plasma, and plasma admixtures comprising both oxygen and nitrogen in varying pressures. Afterwards, the oxygen:nitrogen atomic density ratio was determined in order to observe which plasma parameters allowed for the most control over this ratio to achieve stoichiometric thin films. The effect of varying applied power and pressure on the atomic density of pure oxygen plasmas was consistent with the literature [114–118]. Changing the applied RF power did not appear to provide as much control over the O/N density ratio. However, varying the admixture content provided a wider range of O/N density ratio values, and it was clear that the key parameter that gave the most range for optimising thin film stoichiometry was the admixture ratio. This will be the focus of the next chapter in this thesis.

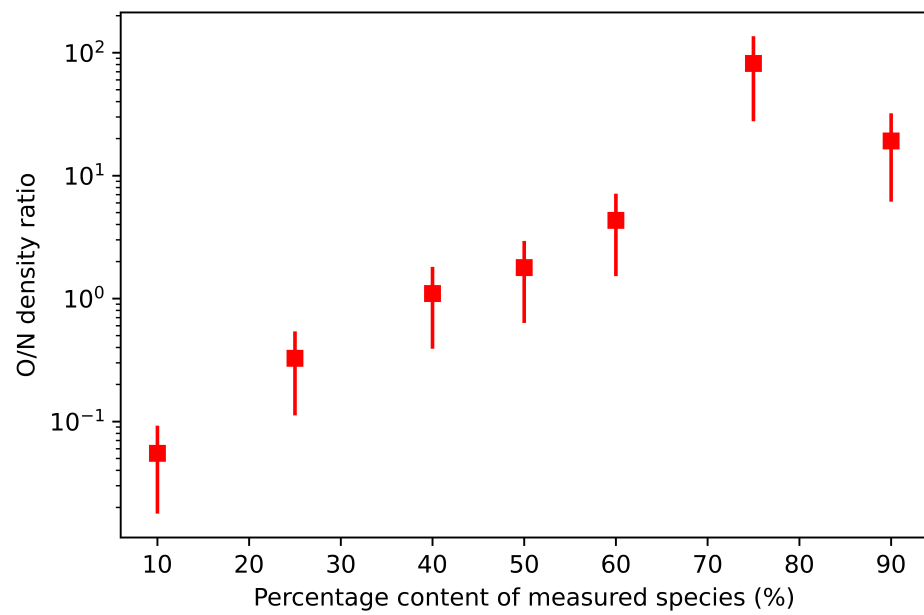


Figure 5.13: The evolution of the ratio of the density of atomic oxygen to nitrogen with respect to percentage content of oxygen. Applied radiofrequency power was set to 600 W, the total chamber pressure was set to 20 Pa, and images were taken  $700 \mu\text{s}$  in the afterglow of the plasma pulse. When the oxygen mix is 10%, the nitrogen mix is assumed to be 90%, and so on.

## Chapter 6

# Analysis of thin films deposited by PE-PLD

This chapter focuses on the analysis of titanium and tantalum oxide and oxynitride thin films deposited by PE-PLD, utilising diagnostic techniques to study their structure and chemical composition. The results here will evaluate the suitability of the PE-PLD technique in producing stoichiometric oxynitride thin films for photocatalysis.

Since silicon substrates are incompatible with UV/Vis spectroscopy, and quartz substrates are incompatible with SEM and XPS diagnostics, all thin films in this chapter were deposited onto silicon-quartz dual substrates, as outlined in section 3.1. SEM analysis of films deposited onto a silicon-only substrate has shown uniformity across the entire depth of the films [28], and so the quartz and silicon layers of the dual substrate were also assumed to be uniform.

Analysis was performed on 7 key films whose deposition conditions are contained in table 6.1. The third TiON thin film deposited with an O:N input ratio of 10:90 was meant to be deposited at a chamber pressure of 20 Pa, but this caused unwanted reflective power within the chamber, meaning the deposition had to be done at 15 Pa instead, allowing for a more stable plasma. The TaON plasma was also meant to be deposited at 20 Pa, but was done at 17 Pa for the same reason.

Table 6.1: Deposition conditions of the 7 thin films. All thin films were deposited onto a dual quartz/silicon substrate for 90 minutes, as outlined in section 3.1.

Desired thin film	RF Plasma Power (W)	Pressure (Pa)	O <sub>2</sub> :N <sub>2</sub> input ratio (if applicable)
TiO <sub>2</sub>	600	15	-
TiON (1)	300	20	50:50
TiON (2)	600	20	50:50
TiON (3)	600	15	10:90
TiN	600	20	-
Ta <sub>2</sub> O <sub>5</sub>	600	20	-
TaON	600	17	25:75

All SEM images in this work were taken with a working distance (distance between bottom of SEM column and top of sample) of 10 mm, electron beam energy of 10 keV, probe current of 12  $\mu$ A, 1,000x magnification, and an LED filter.

## 6.1 Titanium oxide thin films

In previous work, the PE-PLD setup in the York Plasma Institute (YPI) Laboratories has been shown to produce stoichiometric copper and zinc oxide thin films on silicon and quartz substrates. As such, a titanium oxide thin film was deposited onto a silicon-quartz substrate to compare to previous work. Deposition conditions for this film can be seen in table 6.1.

### 6.1.1 SEM and EDX Analysis - Film composition and surface morphology

Figure 6.1 shows an example of an SEM image of titanium oxide material deposited onto a silicon substrate. This image shows a uniform film with small particulates present on the top which are slightly oval in shape, each approximately 2-3  $\mu$ m in diameter. Although these particulates are present throughout the entire area of the surface, they are lacking in structural arrangement, similar to some CuO and Al<sub>2</sub>O<sub>3</sub> films deposited by PE-PLD in previous work done by S. Rajendiran [27] and D. Meehan [28] respectively. To determine

the composition of the deposited film, EDX analysis was performed.

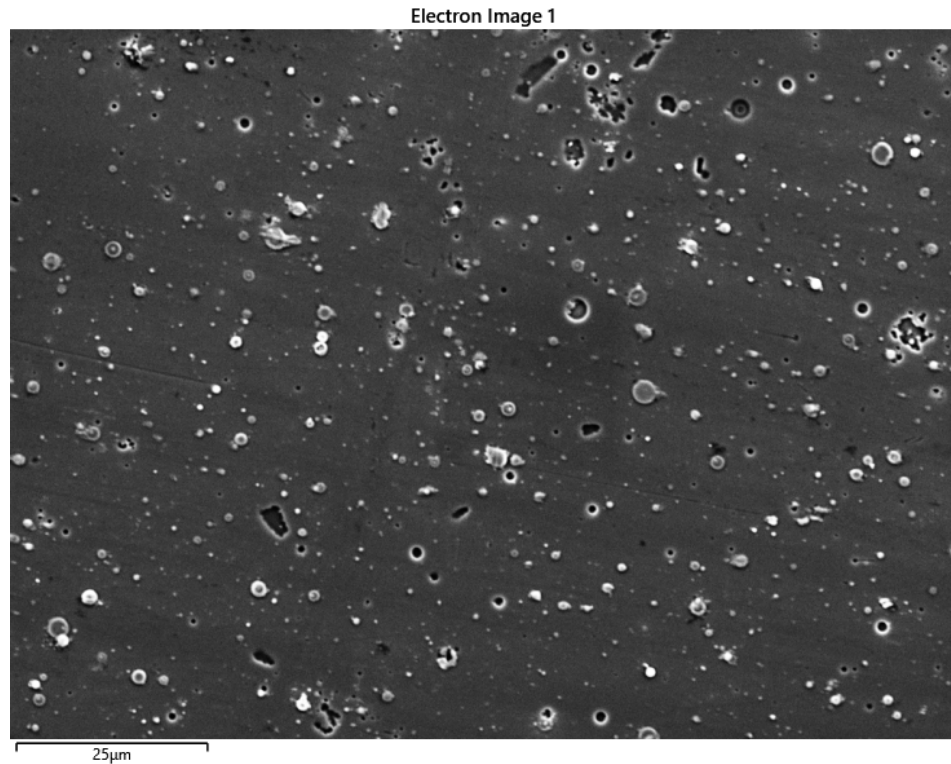


Figure 6.1: 10 kV 1,000x SEM image of the bottom edge of the deposition area for the  $\text{TiO}_2$  thin film deposited at 600 W RF power and 15 Pa pressure.

Three images of the deposition area of the  $\text{TiO}_2$  film were taken with the SEM, each producing an EDX spectrum. Figure 6.2 shows the EDX spectrum created using the image taken in figure 6.1. Here, a carbon impurity can be seen at approximately 0.6 keV. Such an impurity appeared on all the spectra taken of all the deposited thin films. This is likely due to the use of carbon tape on the side of the silicon substrate facing the bottom, which was used to secure the silicon shard onto a steel stub to be read by the SEM camera. Traces of carbon may have been transferred to top of the thin film when the sample was handled in preparation for SEM analysis. Additionally, as silicon was the substrate, the  $K_\alpha\text{Si}$  peak had by far the largest intensity. This is due to the beam energy, which is proportional to the penetration depth of the electron beam, as discussed in [125]. Although the penetration depth of the SEM electrons was not measured, it is clear from the EDX analysis that it is significantly larger than the thin films, which are assumed to have a rough thickness of a few 100 nm based on previous PE-PLD work [28]. It was possible to reduce the  $K_\alpha\text{Si}$  peak by reducing the beam energy, but this also reduced some of the other more important peaks

required to calculate the thin film stoichiometry. Therefore, the beam energy was kept at 10 keV, and the  $K_{\alpha}\text{Si}$  was removed when calculating the stoichiometry of the thin film. A peak corresponding to  $K_{\alpha}\text{Ti}$  can be found at 0.5 keV, and a peak corresponding  $K_{\alpha}\text{O}$  at 0.6 keV. Finally, a doublet peak corresponding to  $L_{\alpha}\text{Ti}$  can be seen between 4.5-5.0 keV.

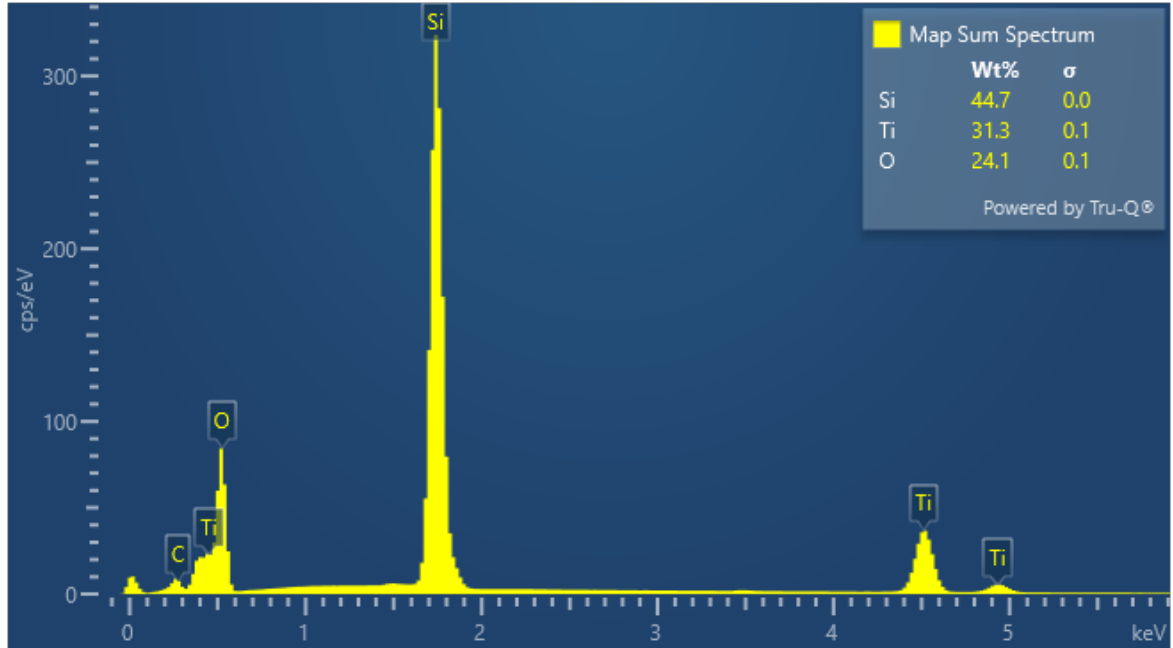


Figure 6.2: 10 kV 1'000x EDX spectrum of  $\text{TiO}_2$  thin film.

For the  $\text{TiO}_2$  film and every subsequent film in this chapter, 2-3 images were taken in different locations of the deposition area, producing a spectrum for each location. Once the spectra were obtained, a calculation for the stoichiometry of the thin film was performed by taking an average value of the atomic percentage of each element recorded by the EDX diagnostic in the 2-3 different locations. The calculation of the stoichiometry of the  $\text{TiO}_2$  film is shown in table 6.2, as an example. This calculation was repeated for all other films.

Table 6.2: Calculation for the chemical composition of the TiO<sub>2</sub> film using 10 kV 1,000x EDX analysis. Uncertainties in the percentage of average atomic content are derived from the standard deviations of the percentages of atomic content without silicon.

Element	Atomic%			Atomic% w/o Si			Avg Atomic%	Stoic wrt Ti
O	40.16	27.72	38.42	69.76	71.79	69.99	71 ± 1	2.39 ± 0.0546
Ti	17.41	10.89	16.47	30.24	28.21	30.01	29 ± 1	1
N	-	-	-	-	-	-	-	-
Si	42.43	61.39	45.11	-	-	-	-	-
Total	100	100	100	100	100	100	100	-
Total w/o Si	57.57	38.61	54.89	-	-	-	-	-

**Average stoichiometry:** TiO<sub>2.39±0.05</sub>

The overall stoichiometry of this titanium oxide thin film was calculated by EDX to be TiO<sub>2.39±0.05</sub>, giving slightly more oxygen than expected. The most likely explanation for this is that the Si wafer may be covered in a layer of SiO<sub>2</sub> as a result of oxidation from being stored under air. If such a layer is on top of the substrate, and the thin film is then deposited on top of it, the EDX would pick up the SiO<sub>2</sub> layer. This means that although the contribution of Si from the SiO<sub>2</sub> is removed from the calculation, the O is not. Since the  $K_{\alpha}$ Ti and  $K_{\alpha}$ O peaks are very close together, it is unclear which counts close to the overlap of the peaks correspond to oxygen content and which correspond to titanium content. To ascertain whether the stoichiometry calculated by EDX was reliable or not, each film analysed with EDX was also analysed and compared with XPS, which probes only the surface layer and not deep into the Si substrate.

### 6.1.2 XPS analysis - Film chemical stoichiometry

XPS analysis of the titanium oxide thin film produced two separate spectra: one corresponding to TiO<sub>2</sub> 2p electrons (see figure 6.3), and one corresponding to O 1s electrons (see figure 6.4). The stoichiometry was calculated as described in section 3.4.5.

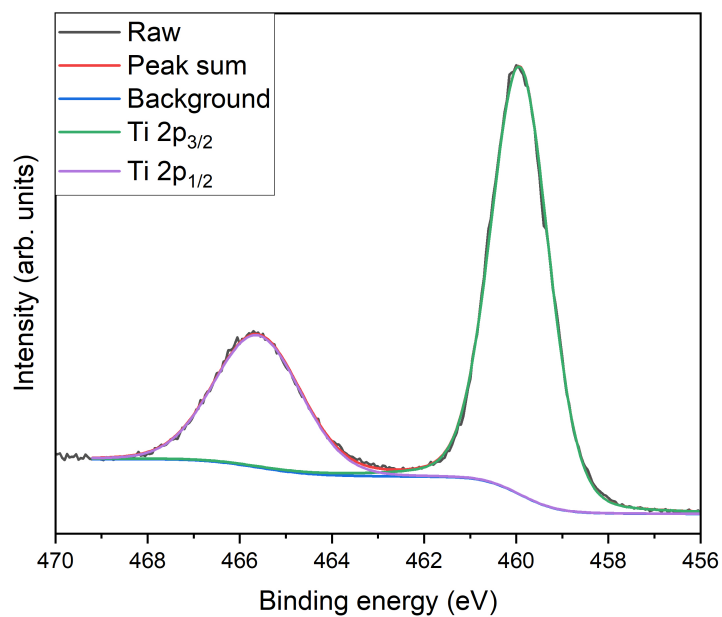


Figure 6.3: XPS spectrum of TiO<sub>2</sub> 2p electrons from the titanium oxide thin film.

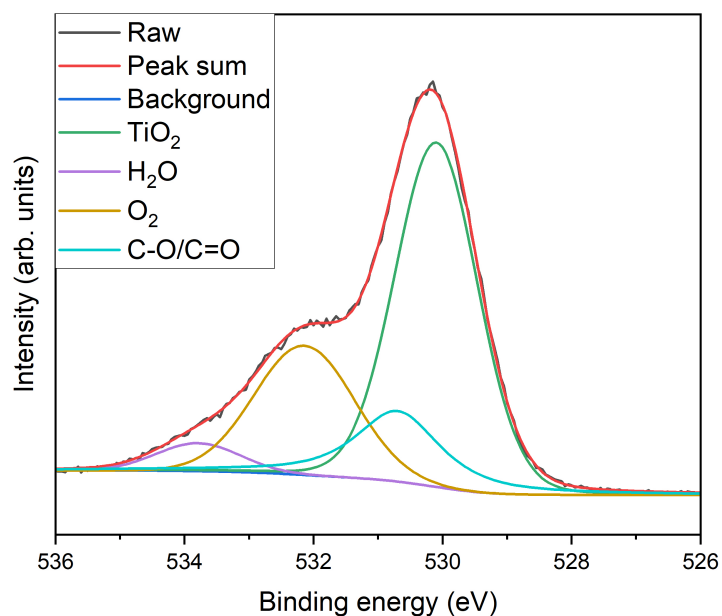


Figure 6.4: XPS spectrum of O 1s electrons from the titanium oxide thin film.

In figure 6.4, the C–O and C=O contributions likely correspond to carbon impurities

present on the surface, as mentioned in the previous subsection. The  $O_2$  curve that is present suggests there is additional oxygen either in the film or adsorbed onto the surface, and does not make up  $TiO_2$ , which is likely to explain the higher O concentration in EDX. The stoichiometry was calculated by XPS as  $TiO_{1.995}$ , which is much closer to the desired stoichiometry than the respective EDX calculation. However, the XPS calculation excludes  $O_2$  and C–O contributions and only takes into account contributions from  $TiO_2$ , so it is not unexpected to find a value approximately equal to 2. An additional difference between the two diagnostics is XPS provides more detailed information about the chemical composition on the top 1-10 nm of the thin film, whereas EDX probes deeper into the film (about 1-2  $\mu m$ ) to provide information over a larger volume. These results suggest even more strongly that the deposited thin film has very small thickness, and that the EDX calculation of stoichiometry would have almost certainly included layers beneath the surface which are made up almost entirely of silicon with little to no titanium or oxygen content. Despite this, it is clear from analysis with these two diagnostics that PE-PLD can successfully produce highly stoichiometric  $TiO_2$  thin films.

### 6.1.3 XRD analysis - Film crystal structure

Figure 6.5 shows an XRD spectrum of the titanium oxide thin film. Here, there is a clear, sharp intensity peak at the  $2\theta/\omega$  angle of  $69^\circ$  corresponding to (100) silicon, with almost no other clear peaks.  $TiO_2$  materials with a more crystalline structure tend to produce peaks towards the lower end of the spectrum. For example, if (110) rutile and (101) anatase  $TiO_2$  structures are present, they are expected to peak between angles of  $20-30^\circ$ , but evidently, that is not observed here. Therefore, it can only be concluded that the deposited titanium oxide material is amorphous with the stoichiometry that can be measured.

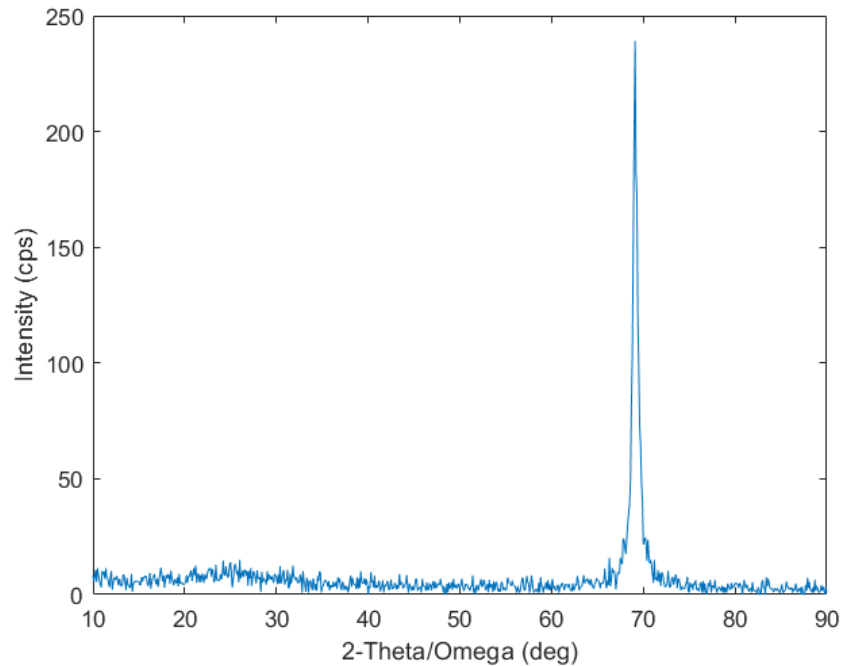


Figure 6.5: XRD spectrum of  $\text{TiO}_2$  thin film. The peak at approximately  $69^\circ$  signifies (100) silicon.

#### 6.1.4 UV/Vis absorption spectroscopy - Film absorption

The UV/Vis absorption profile for deposited  $\text{TiO}_2$  on a quartz substrate is displayed in figure 6.6. The film is shown to absorb light mostly within the UV range, peaking between 200-270 nm, which is well outside the visible spectrum. This absorption is consistent with literature on  $\text{TiO}_2$ , as it is known to absorb light in a range similar to that seen in this work, and not light in the visible region [126]. Additionally, the absorbance value is minimum between the 400-500 nm region, which was also observed in work published by J. Dharma et al. [127]. There have been cases of  $\text{TiO}_2$  films displaying an absorbance peak closer to the visible part of the spectrum, such as in E. Arpaç's work, in which undoped  $\text{TiO}_2$  showed a peak between 300-400 nm, but the films were synthesised by a special method called the hydrothermal process [128].

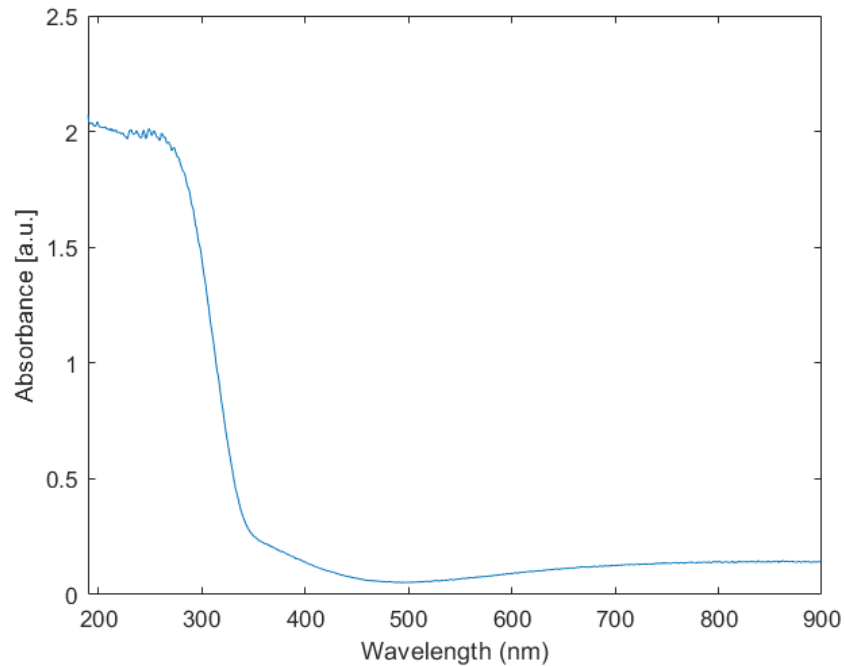


Figure 6.6: UV/Vis absorption spectrum for deposited TiO<sub>2</sub> film, with absorption profile for plain quartz substrate subtracted.

## 6.2 Titanium oxynitride and nitride thin films

A total of three TiON thin film depositions were attempted, each varying in deposition conditions, as outlined in table 6.1. Since the results from chapter 5 showed that power and pressure had a minimal effect on the atomic density of the background plasma compared to admixture ratio, this change in pressure was assumed to have negligible effect on the thin film deposition. Following the deposition of the third TiON film, a TiN film was also deposited to observe the chemical composition of the film without any oxygen present in the chamber.

### 6.2.1 SEM and EDX Analysis - Film composition and surface morphology

An SEM image of the film deposited with O:N input ratio 50:50, RF plasma power 300 W, and chamber pressure 20 Pa is seen in figure 6.8, and an image of a similar film deposited at almost identical conditions with the exception of an RF plasma power of 600 W can be seen in figure 6.7. As with the TiO<sub>2</sub> film in the previous section, the deposited films here appear to be homogeneous with small thickness due to the size and uniformity of the deposited

content. The brightness varies between the two images, but the size of the particulates does not appear to vary significantly between the two, suggesting plasma power does not affect the size of the particulates.

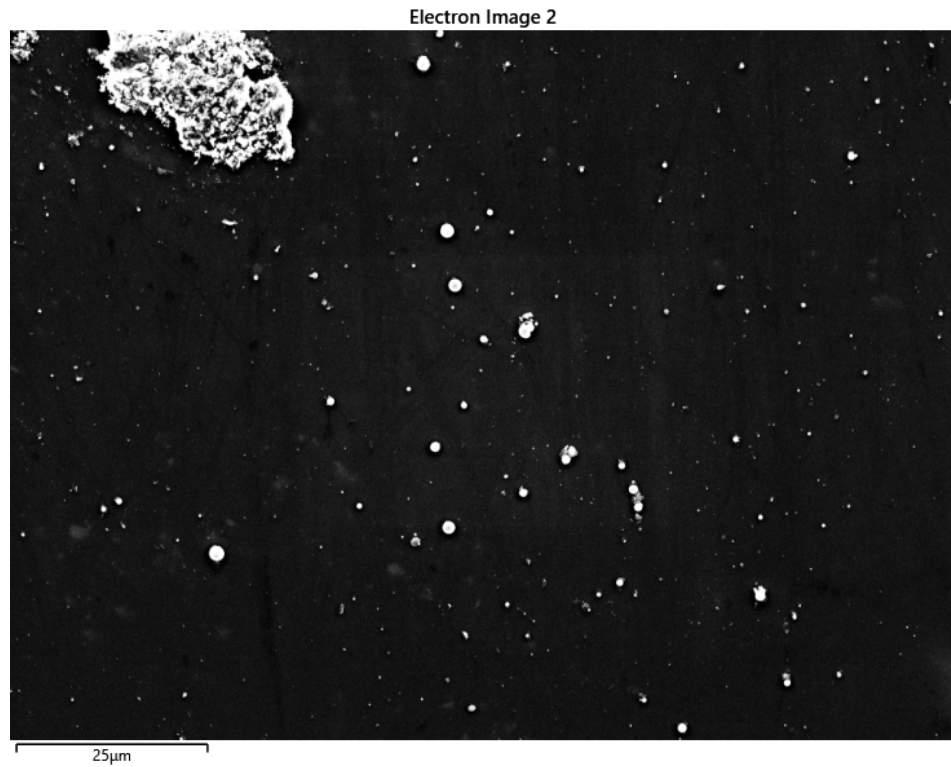


Figure 6.7: 10 kV 1,000x SEM image of part of the deposition area for the O:N = 50:50 TiON thin film no. 1 deposited at 300 W RF power and 20 Pa pressure. The large white cluster near the top left corner of the image is carbon dirt.

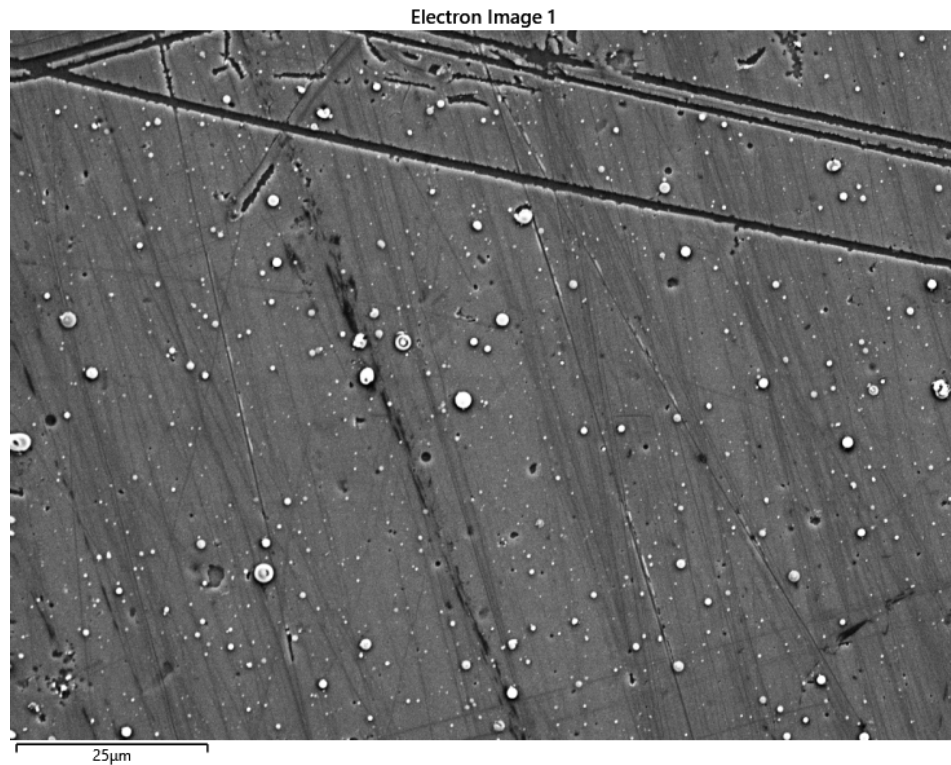


Figure 6.8: 10 kV 1,000x SEM image of part of the deposition area for the O:N = 50:50 TiON thin film no. 2 deposited at 600 W RF power and 20 Pa pressure. The large, dark lines seen at the top of the image indicate slight scratching of the silicon substrate.

All 7 films analysed by EDX in this work had a silicon intensity peak at an electron energy of approximately 1.5-2.0 keV, as seen in figure 6.2. As such, all EDX spectra shown henceforth shall be zoomed in towards the more important intensity peaks related to deposited content such as oxygen and nitrogen. Figures 6.9, 6.10, and 6.11 show the EDX spectra of the three respective TiON deposition attempts.

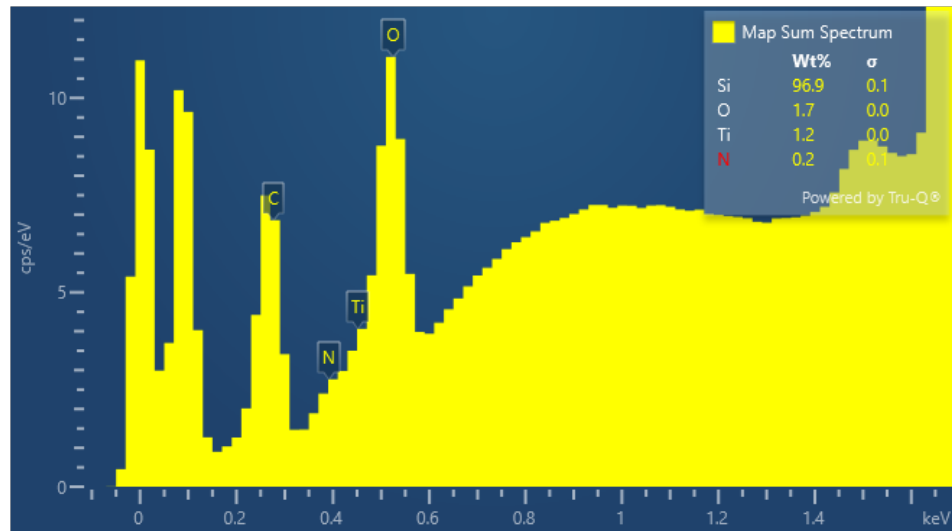


Figure 6.9: 10 kV 1'000x EDX spectrum of TiON thin film no. 1 deposited at 300 W power, 20 Pa pressure, and O:N input ratio of 50:50. Figure zoomed upon the  $K_{\alpha}O$  and  $K_{\alpha}N$  intensity peaks. A carbon impurity is present between 0.25-0.3keV.

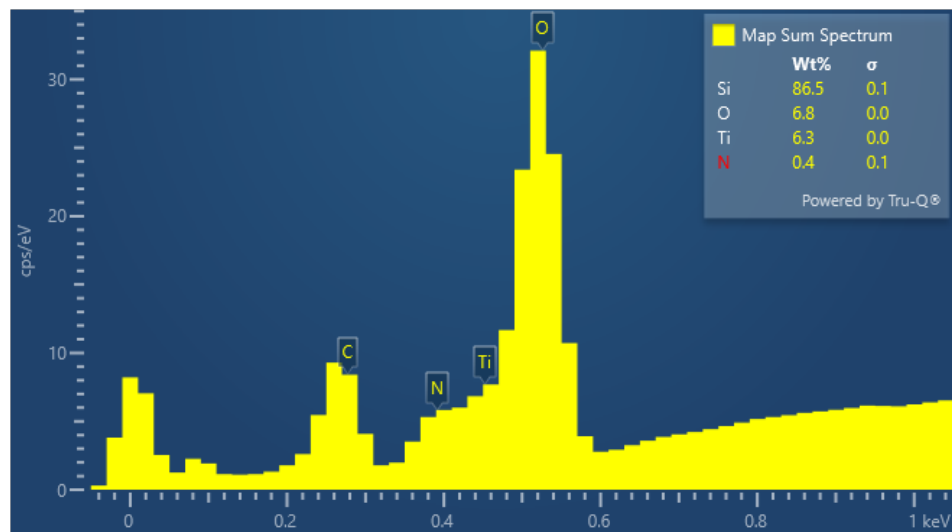


Figure 6.10: 10 kV 1'000x EDX spectrum of TiON thin film no. 2 deposited at 600 W power, 20 Pa pressure, and O:N input ratio of 50:50. Figure zoomed upon the  $K_{\alpha}O$  and  $K_{\alpha}N$  intensity peaks. A carbon impurity is present between 0.25-0.3keV.

Table 6.3: Average stoichiometries of the three TiON thin film deposition attempts calculated by EDX. A negligible amount of nitrogen was detected by EDX in the third attempt, despite the O:N ratio of 10:90, causing the atomic percentage of N present to equal 0%, resulting in no nitrogen in the stoichiometry calculation. The derivation of the uncertainty values is described in table 6.2.

TiON Film no.	Power (W)	Pressure (Pa)	O:N Ratio	Mean Stoichiometry
1	300	20	50:50	$\text{TiO}_{3.576 \pm 0.950} \text{N}_{0.278 \pm 0.097}$
2	600	20	50:50	$\text{TiO}_{3.182 \pm 0.126} \text{N}_{0.207 \pm 0.036}$
3	600	15	10:90	$\text{TiO}_{3.033 \pm 0.038}$

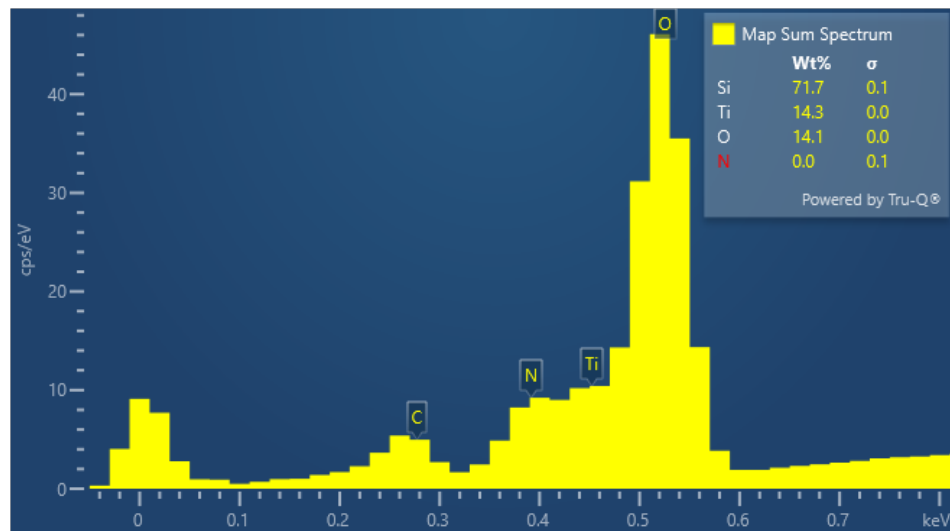


Figure 6.11: 10 kV 1'000x EDX spectrum of TiON thin film no. 3 deposited at 600 W power, 15 Pa pressure, and O:N input ratio of 10:90. Figure zoomed upon the  $K_{\alpha}\text{O}$  and  $K_{\alpha}\text{N}$  intensity peaks. A carbon impurity is present between 0.25-0.3keV.

Very little nitrogen was detected in any of the three thin films. The peaks corresponding to  $K_{\alpha}\text{O}$ ,  $K_{\alpha}\text{N}$ , and  $K_{\alpha}\text{Ti}$  are overlapped in all three EDX spectra, which made it difficult for the diagnostic to distinguish between the three elements. Despite the fact a peak labelled with N showed up at around 0.4 keV on the spectrum of the third TiON thin film attempt (figure 6.11), the nitrogen content recorded by the software was negligible, equalling 0, as seen in the figure. This unfortunately resulted in no nitrogen in the stoichiometry calculation of that particular thin film, as seen in table 6.3.

Following the TiON results, a TiN film deposition was attempted, in which titanium remained the target and nitrogen was the only non-metal background plasma species present in the chamber, with no oxygen fed into the chamber at all. This was performed to ascertain the suitability of PE-PLD creating stoichiometric thin films with pure nitrogen plasma.

Figure 6.12 contains an SEM image of the deposited film. As with the previous images, the particulates of deposited material show the film is inhomogeneous, but unlike the previous images, the particulates appear to range from about 3-5  $\mu\text{m}$  in diameter compared to those seen on the  $\text{TiO}_2$  film (figure 6.1), which range from  $< 1\mu\text{m}$  to about 4  $\mu\text{m}$  in diameter. The particulates on the TiN film also appear to be more spread out from each other.

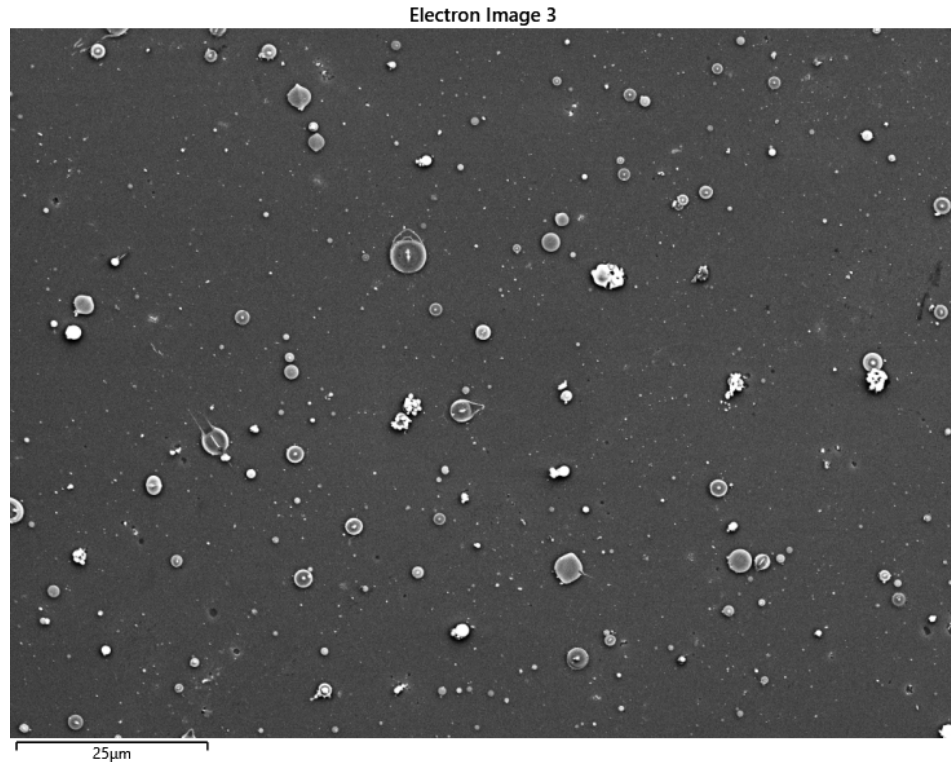


Figure 6.12: 10 kV 1,000x SEM image of part of the deposition area for the TiN thin film deposited at 600 W RF power and 20 Pa pressure.

Despite the absence of oxygen plasma in the chamber during the deposition, there was a surprising amount of oxygen detected by EDX, as seen on the spectrum in figure 6.13. This is possibly due to a silicon oxide layer beneath the surface of the film, as silicon is known to oxidise easily at room temperature [129], as well as by deposition techniques [130]. There could also be oxygen present on the complete surface of the sample, perhaps due to air exposure. It is unlikely the thin film itself is oxidising in the air as titanium materials typically require temperatures of hundreds of degrees Celsius for oxidation to occur [131]. Further investigation is needed to understand why little nitrogen is detected on the film, and why such an unexpected amount of oxygen is observed. The average stoichiometry of this film was calculated as  $\text{TiO}_{3.405}\text{N}_{0.068}$ .

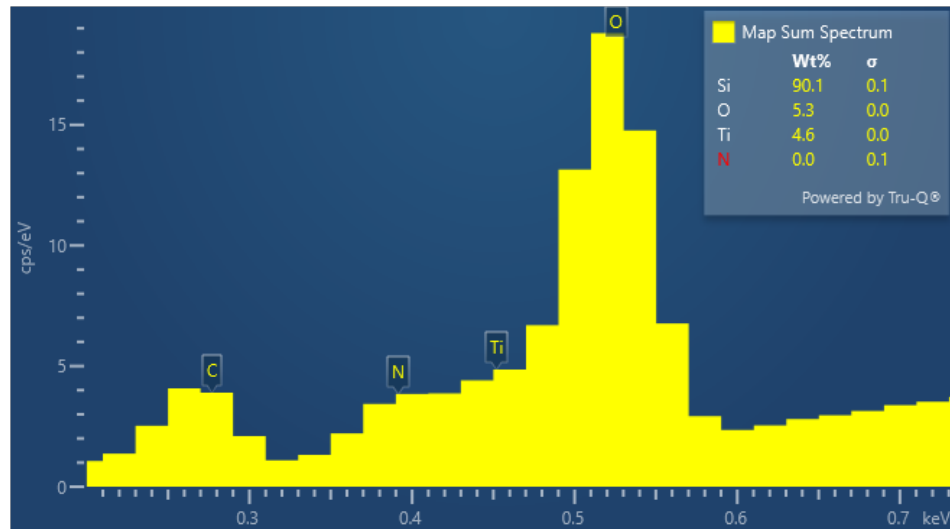


Figure 6.13: 10 kV 1'000x EDX spectrum of TiN thin film deposited at 600 W power and 20 Pa pressure. Figure zoomed upon the  $K_{\alpha}O$  and  $K_{\alpha}N$  intensity peaks. A carbon impurity is present between 0.25-0.3keV.

### 6.2.2 XPS analysis - Film chemical stoichiometry

The XPS analysis of the TiON deposition attempts showed results consistent with the EDX spectra, showing little to no nitrogen present on the surface of the thin film as seen in figures 6.14 and 6.15. Instead, peaks between 530-532 eV corresponding to  $TiO_2$  appear to be present. This is reflected in the stoichiometry calculations in 6.4, in which there was insufficient nitrogen to be included in the calculations, showing stoichiometries close to  $TiO_2$  instead. Any TiON material detected would be expected to peak approximately between those corresponding to Ti  $2p_{3/2}$  electrons in  $TiO_2$  and TiN compounds, which would be between 455-460 eV on figure 6.14, according to the ThermoFisher database of XPS spectra [132]. This suggests the oxygen plasma is reacting more quickly with the titanium plasma plume than the nitrogen plasma in the chamber, producing titanium oxide before the nitrogen is able to interact, resulting in mostly  $TiO_2$  on the surface. However, even without the presence of oxygen plasma in the chamber, it is apparent that the nitrogen plasma struggles to react with the titanium plasma plume, with the XPS spectrum seen in figure 6.16 showing no nitrogen peak. Since only  $TiO_2$  peaks are fitted, nitrogen could not be included in the stoichiometry calculation. Overall, the XPS results show consistency with the EDX results in that little to no nitrogen is detected.

Table 6.4: Average stoichiometries of the three TiON thin film deposition attempts calculated by XPS. A negligible amount of nitrogen was detected by XPS in all three attempts, resulting in no nitrogen in the stoichiometry calculation.

TiON Film no.	Power (W)	Pressure (Pa)	O:N Ratio	Mean Stoichiometry
1	300	20	50:50	TiO <sub>1.99</sub>
2	600	20	50:50	TiO <sub>1.97</sub>
3	600	15	10:90	TiO <sub>1.99</sub>

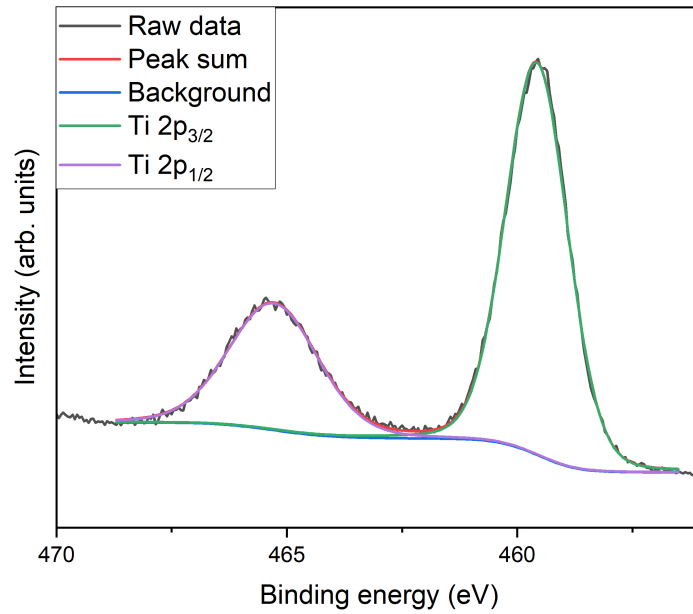


Figure 6.14: XPS spectrum of Ti  $2p_{3/2}$  and  $2p_{1/2}$  electrons from the titanium oxynitride thin film deposition attempt with O:N input ratio 10:90 (figure repeated from figure 3.24 in section 3.4.5).

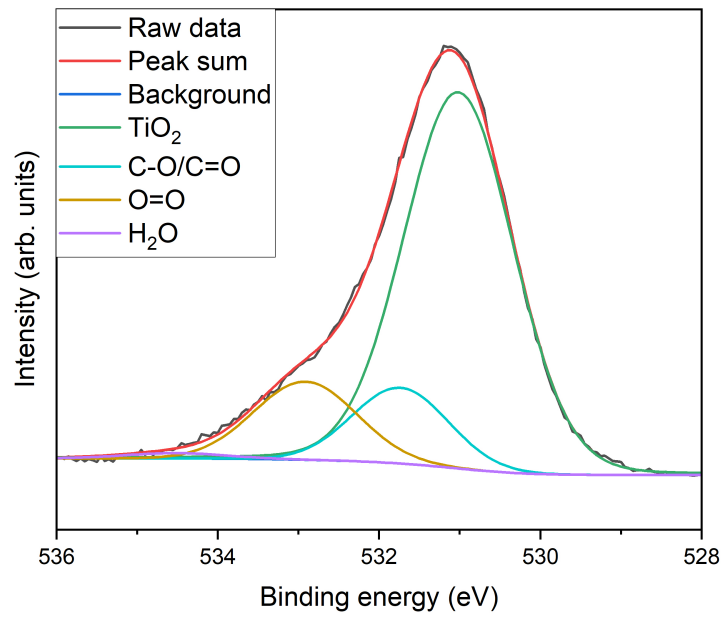


Figure 6.15: XPS spectrum of O 1s electrons from the titanium oxynitride thin film deposition attempt with O:N input ratio 10:90.

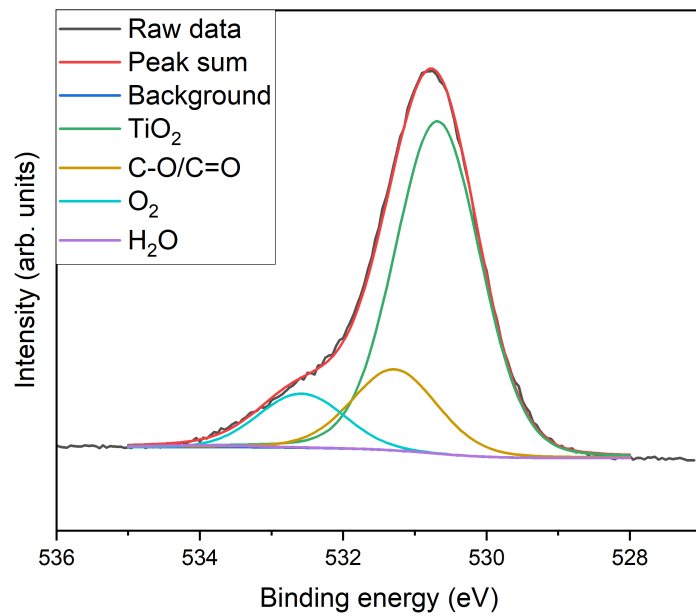


Figure 6.16: XPS spectrum of O 1s electrons from the titanium nitride thin film deposition attempt.

### 6.2.3 XRD analysis - Film crystal structure

The XRD spectrum of the TiON thin film deposition attempt with O:N input ratio 10:90 is presented in figure 6.17. This spectrum has a couple of similarities to that of figure 6.5, including the peak at  $69^\circ$  corresponding to (100) silicon, and no other notable peaks, once again signifying the small thickness of the thin film compared to the silicon substrate. However, there are also a few distinct differences between the two spectra: the (100) silicon peak in the TiON spectrum gives a much higher intensity (approximately 16 times greater), with a small amount of noise fluctuating at intensities similar to the  $\text{TiO}_2$  spectrum, suggesting the TiON film is thinner than the  $\text{TiO}_2$  one.

With the deposition method being consistent between all 7 deposited thin films, it is evident from the two XRD spectra that all films deposited in this work are amorphous with a very small thickness.

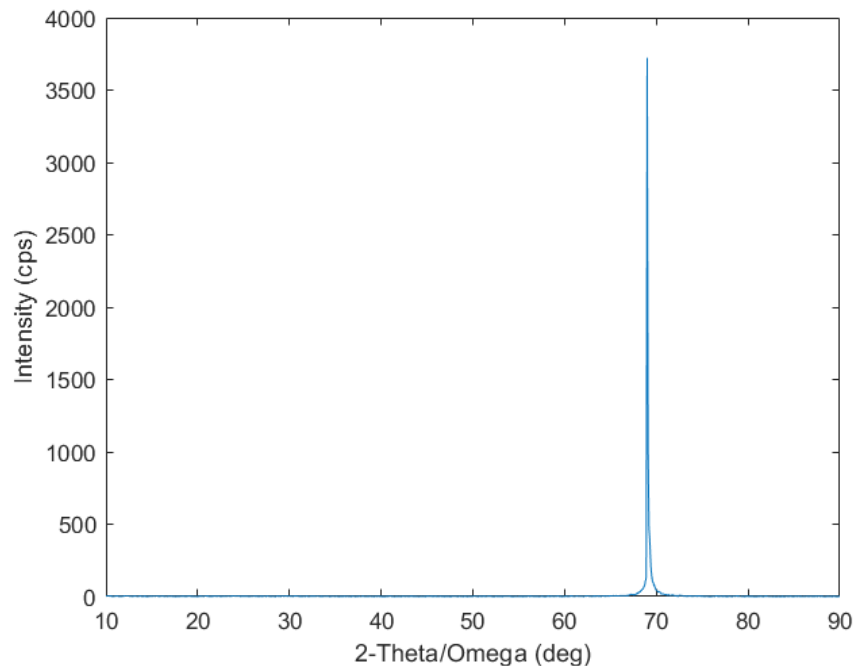


Figure 6.17: XRD spectrum of TiON thin film deposition attempt with flow ratio O:N = 10:90. The peak at approximately  $69^\circ$  signifies (100) silicon.

### 6.2.4 UV/Vis absorption spectroscopy - Film absorption

Like the  $\text{TiO}_2$  UV/Vis absorption profile, each of the TiON deposition attempts displayed an absorbance peak between 200-270 nm. However, compared to the  $\text{TiO}_2$  spectrum, the

amount of radiation absorbed by the TiON films was much smaller within the 200-270 nm region, see figure 6.18 as an example. Additionally, the TiON films absorbed a little more radiation at wavelengths closer to the visible spectrum, such as 400 nm. Successfully deposited TiON thin films are expected to show absorption peaks either between 400-500 nm, or between 600-700 nm, which covers most of the visible spectrum [74]. However, this is not observed here due to insufficient nitrogen content and amorphous structure. The third TiON film deposited at 15 Pa gave a higher absorbance peak than the other two TiON films deposited at 20 Pa each. However, this is insufficient to conclude that background plasma pressure affects the absorbance peak. In work published by N. Mucha et al. [74], in which TiON films were produced from TiN targets and O<sub>2</sub> plasma, no clear trend was observed between O<sub>2</sub> pressure and absorbance peak, despite all three films showing multiple absorbance peaks within the visible region.

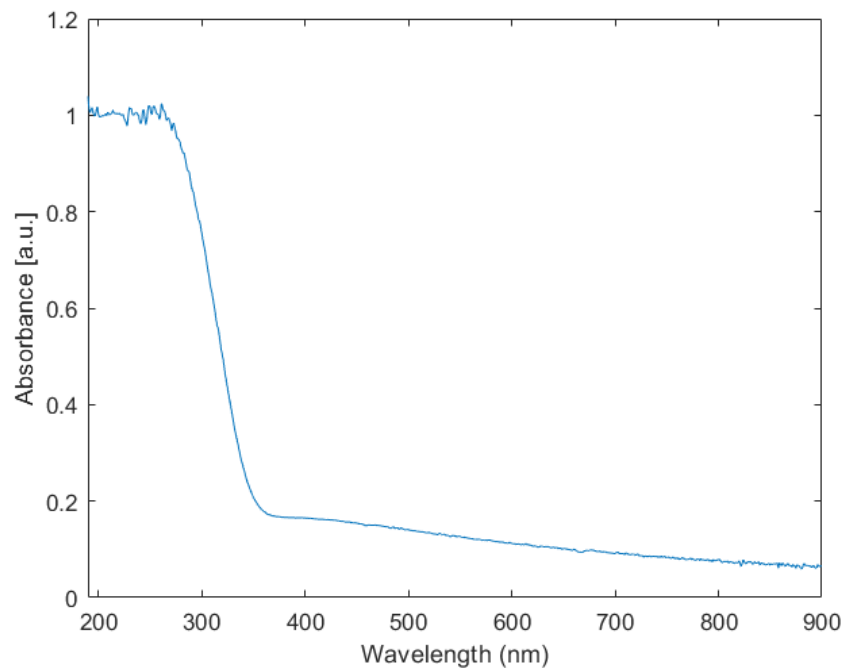


Figure 6.18: UV/Vis absorption spectrum for deposited TiON film attempt no. 3 (O:N = 10:90), with absorption profile for plain quartz substrate subtracted.

The maximum absorbance by TiON thin film no. 3 was roughly half that of the TiO<sub>2</sub> film. Taking this and the EDX spectra into account, it was hypothesised that there was a correlation between maximum absorbance and amount of silicon detected by EDX, which in turn suggested absorbance could be interpreted as film thickness. Thus, the absorbance

profiles of all titanium compound thin films were plotted onto one figure for comparison, see figure 6.19.

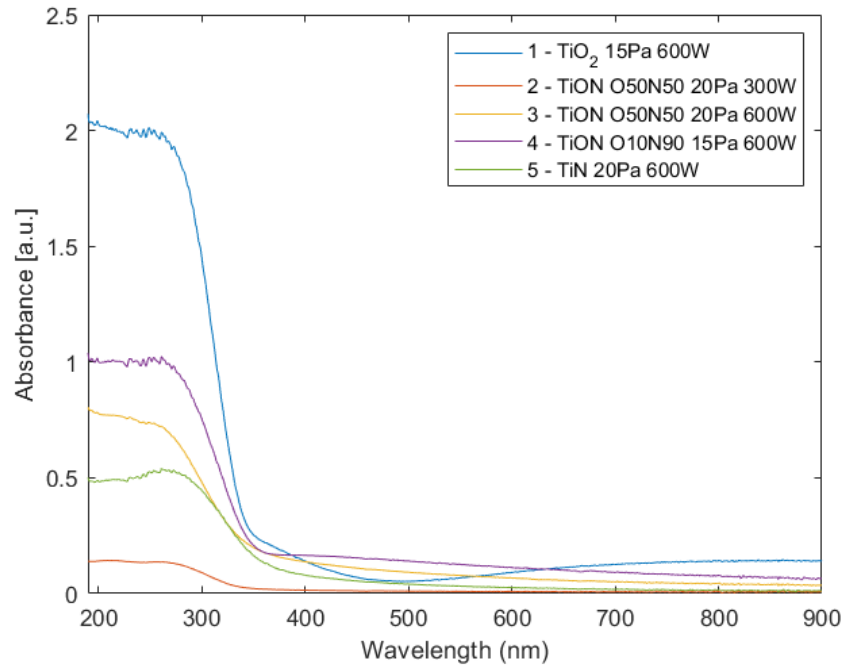


Figure 6.19: UV/Vis absorption spectrum for all deposited titanium compound films, with absorption profile for plain quartz substrate subtracted.

If the absorbance peak in figure 6.19 is read as film thickness, this could correlate with the silicon content in EDX. In other words, films with low silicon content show a thicker film. Table 6.5 compares the UV-Vis peaks of all titanium compound thin films with their respective percentage of silicon content detected by EDX. Comparing these values, there is a palpable correlation between absorbance and detected silicon content, with the TiO<sub>2</sub> film showing the highest absorbance and lowest amount of detected Si, and the first TiON film showing the lowest absorbance and highest amount of detected Si.

Table 6.5: The average percentage of silicon content detected by EDX compared with the maximum UV/Vis absorbance for each of the five deposited titanium compound thin films.

Deposited thin film	Average % of Si content detected by EDX	Maximum UV/Vis absorbance (a.u.)
TiO <sub>2</sub>	49.64	2.0719
TiON (1)	95.96	0.1429
TiON (2)	82.42	0.8053
TiON (3)	71.34	1.0392
TiN	86.28	0.5395

To check if the absorbance peak shifts to lower wavelengths, each curve in figure 6.19 was normalised so the absorbance went from 1 to 0 with increasing wavelength, allowing for direct comparison between the part of the profile in which the absorbance drops at a fast rate, see figure 6.20. For the normalised peaks, the drop happens further to the right in the TiN and TiON O:N = 10:90 film, i.e. it shifts further in towards the visible range. The two TiON O:N = 50:50 peaks appear to drop at earlier wavelengths than the others, meaning these two films would be least ideal for absorbing visible light. Since two of the films with deposited nitrogen drop earlier than the TiO<sub>2</sub> one, and the other two drop later, this is insufficient to support the current argument for using nitrogen in these films for photocatalysis.

Figure 6.20 also shows that some of the films give absorbance peaks at different wavelengths. The TiN peaks at 261 nm, and the first TiON film peaks at 209 nm and again at 214 nm. However, the TiO<sub>2</sub>, second TiON, and third TiON films peak at the starting wavelength, 190 nm, which is the shortest wavelength the spectrophotometer can read, so this may be due to a hardware limitation. The data in this spectrum could indicate there is at least some nitrogen in the background plasma used in the deposition process, though there is still insufficient evidence of nitrogen in the film. The films with the most nitrogen detected lead to a slight shift of the absorption curve towards the visible light range. It is not a huge difference by any means, but this could be an indication that there is some nitrogen in the film after all, albeit smaller than can be measured.

An additional point that may indicate the presence of nitrogen is the absorbance of each film past 350 nm. As seen in figure 6.20, the TiO<sub>2</sub> film gives the the lowest absorbance,

whilst all the films which were deposited with nitrogen in the background plasma show a little more absorbance throughout the 350 nm range and beyond. Once again, this small difference is not conclusive but may provide a possibility that there could be a small amount of nitrogen in the other films besides the  $\text{TiO}_2$  one after all. This may mean the concept of photocatalytic metal oxynitride thin films could still work. It would, however, require a higher concentration of N in the film for a bigger effect and so the N content can be measured. This suggests a better approach would be to ablate a TiN target in an  $\text{O}_2$  plasma instead of a Ti target in a  $\text{O}_2:\text{N}_2$  plasma as part of future research.

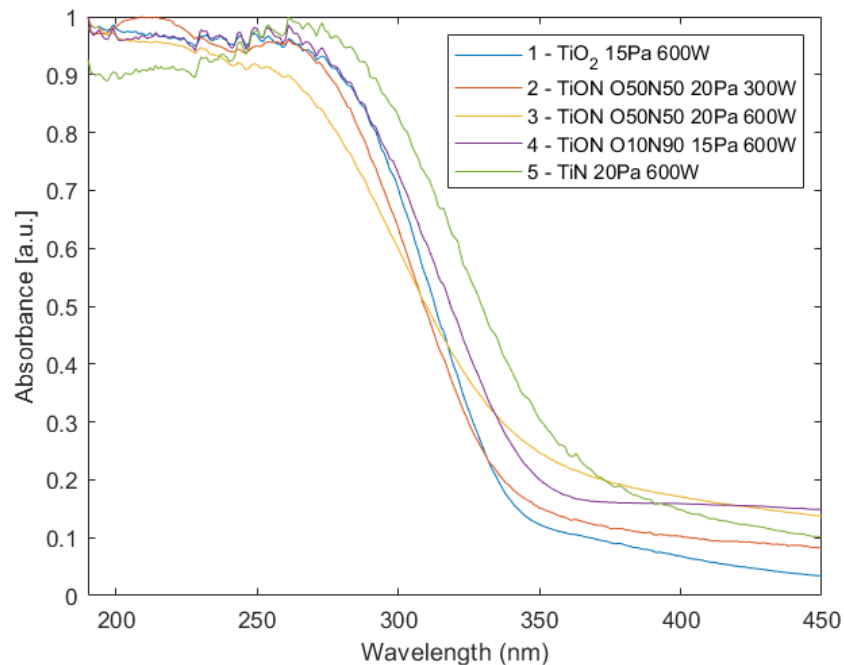


Figure 6.20: UV/Vis absorption spectrum for all deposited titanium compound films, with absorption profile for plain quartz substrate subtracted and normalised absorbance, zoomed in on the  $\lambda = 190 - 450\text{nm}$  region.

### 6.3 Tantalum oxide thin films

Another candidate material for photocatalytic thin films is tantalum. As concluded in chapter 4, tantalum plumes showed higher electron temperatures than titanium plumes, which is likely to lead to a different interaction between plume and background plasma, which could in turn result in a deposited film with different characteristics. A tantalum oxide and tantalum oxynitride thin film were deposited to investigate possible differences in O:N content,

stoichiometry, and UV/Vis absorption compared to titanium thin films. The deposition conditions for both films can be found in table 6.1.

### 6.3.1 SEM and EDX Analysis - Film composition and surface morphology

As seen in figure 6.21, the content on the tantalum oxide thin film consisted of non-spherical particulates once again, albeit much smaller in size than on the titanium compound thin films, with the largest observable particulate being approximately  $2 \mu\text{m}$  in diameter. Additionally, there is much less deposited content on the substrate compared to the previous thin films, which is reflected in the EDX spectrum in figure 6.22, in which silicon made up approximately 88.6% of the detected species, a much higher percentage than in most previous thin films. However, as observed on the spectrum, the Ta and Si peaks are positioned very close together, much like the O, N, and Ti peaks in the titanium compound thin films earlier in the chapter, making the quantification of Ta more challenging. The overall calculated stoichiometry of this tantalum oxide film was calculated as  $\text{TaO}_{3.299 \pm 0.262}$ , or  $\text{Ta}_2\text{O}_{6.598 \pm 0.523}$ , to give the same proportion of Ta atoms with that of the ideal stoichiometric compound  $\text{Ta}_2\text{O}_5$ . As with many of the previous thin films, there is more oxygen present in the film than expected, likely due to oxidation of the silicon substrate once again.

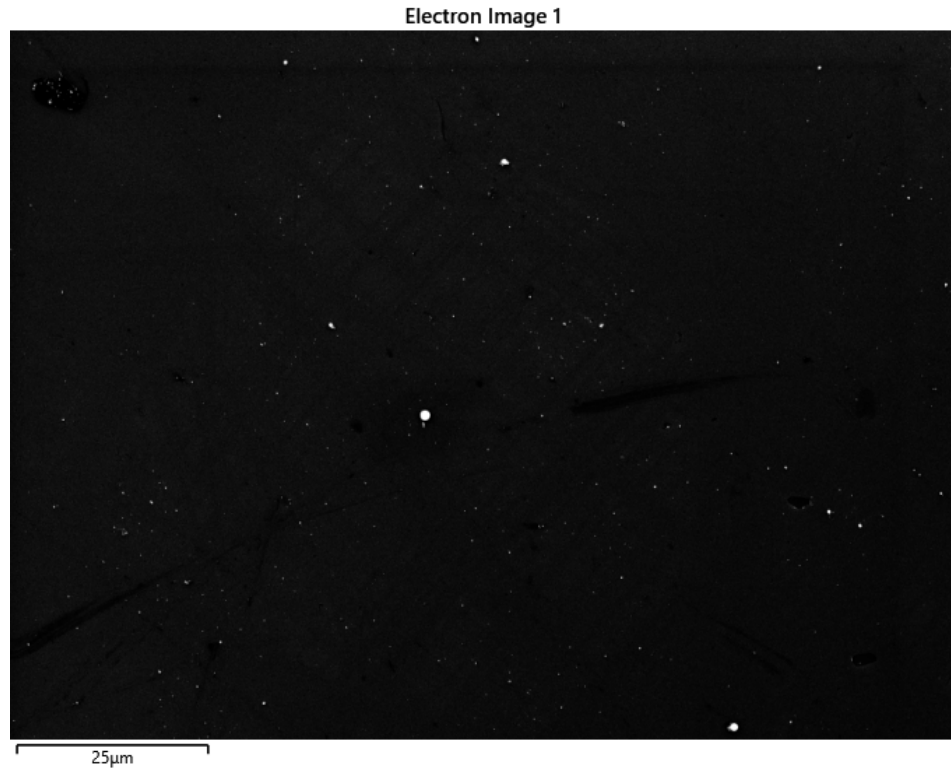


Figure 6.21: 10 kV 1,000x SEM image of the bottom edge of the deposition area for the  $\text{Ta}_2\text{O}_5$  thin film deposited at 600 W RF power and 20 Pa pressure.

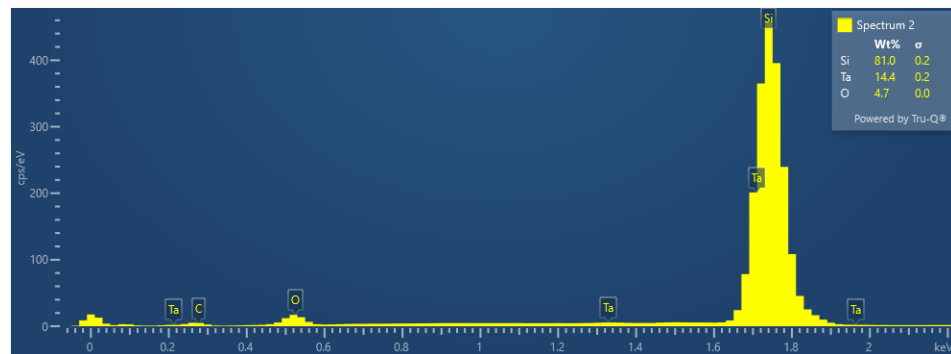


Figure 6.22: 10 kV 1'000x EDX spectrum of the  $\text{Ta}_2\text{O}_5$  thin film deposited at 600 W power and 20 Pa pressure. A carbon impurity is present between 0.25-0.3keV.

### 6.3.2 XPS analysis - Film chemical stoichiometry

Although peaks corresponding to tantalum oxide were detected, as seen in figure 6.23, the stoichiometry was calculated as  $\text{TaO}_{1.82}$ , or  $\text{Ta}_2\text{O}_{3.64}$ , which is lower than the expected  $\text{Ta}_2\text{O}_5$ . This is significantly different from the EDX calculation, which gave more oxygen than expected. It is possible that tantalum metal is present on the silicon substrate, in

addition to oxygen accrued on the surface over time due to oxidation of silicon.

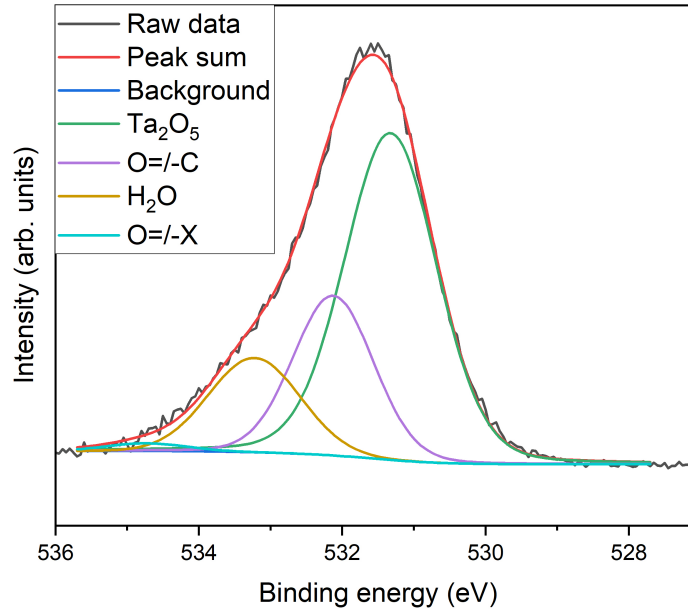


Figure 6.23: XPS spectrum of O 1s electrons from the tantalum oxide thin film deposition attempt.

### 6.3.3 UV/Vis absorption spectroscopy - Film absorption

Unfortunately, due to the misalignment of the substrates during the deposition, there was very little material deposited onto the quartz substrate, meaning no meaningful UV/Vis could be obtained for  $\text{Ta}_2\text{O}_5$ .

## 6.4 Tantalum oxynitride thin films

The final film deposited in this work was a TaON film under an RF power of 600 W, chamber pressure of 17 Pa, and O:N flow ratio of 25:75.

### 6.4.1 SEM and EDX Analysis - Film composition and surface morphology

The TaON SEM image in figure 6.24 and its respective EDX spectrum in figure 6.25 showed little content was deposited, with silicon once again making up 88-90% of the detected species. The stoichiometry of the thin film was calculated to be  $\text{TaO}_{2.898 \pm 0.326} \text{N}_{0.128 \pm 0.001}$ ,

but similar to the tantalum oxide film discussed earlier, the quantification is challenging due to the overlap of the  $K_{\alpha}$ Ta and  $K_{\alpha}$ Si peaks, and the  $K_{\alpha}$ O and  $K_{\alpha}$ N peaks.



Figure 6.24: 10 kV 1,000x SEM image of the bottom edge of the deposition area for the TaON thin film deposited at 600 W RF power and 17 Pa pressure.

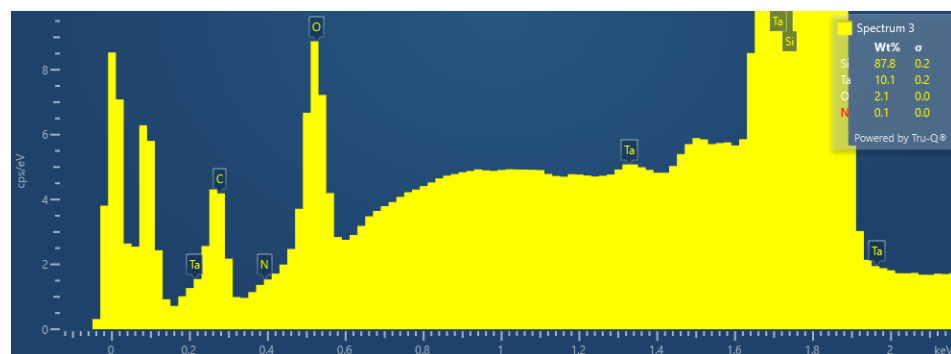


Figure 6.25: 10 kV 1'000x EDX spectrum of the TaON thin film deposited at 600 W power and 17 Pa pressure. Figure zoomed upon the  $K_{\alpha}$ Ta,  $K_{\alpha}$ O, and  $K_{\alpha}$ N intensity peaks. A carbon impurity is present between 0.25-0.3keV.

### 6.4.2 XPS analysis - Film chemical stoichiometry

Once again, the amount of nitrogen present on the surface was insufficient to be detected by XPS (figure 6.26), and no nitrogen was included in the final calculated stoichiometry value of  $\text{TaO}_{1.53}$ . Once again, this differs considerably to the stoichiometry calculated by EDX. Possible reasons for this include that EDX is picking up a lot of the  $\text{SiO}_2$  content on the substrate due to its penetration depth as discussed before, and there may be additional Ta on the surface that only XPS has picked up. The overlapping of peaks from the EDX analysis make it difficult to accurately quantify the chemical composition, complicating this as well.

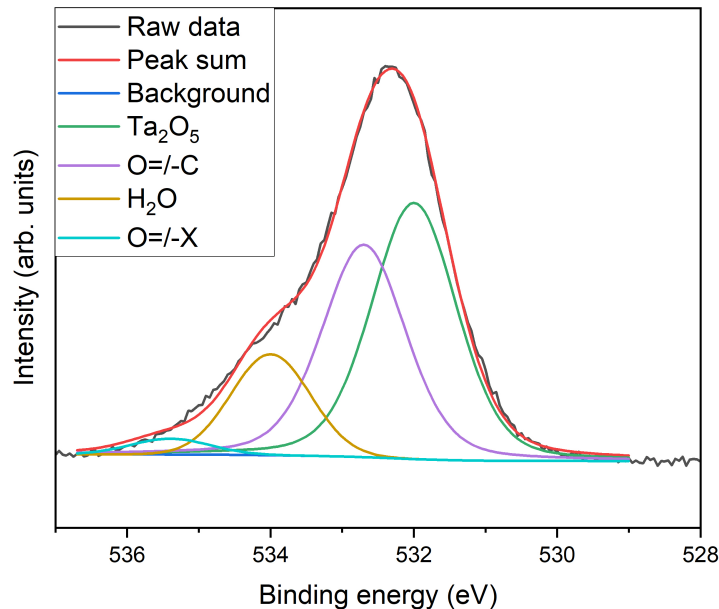


Figure 6.26: XPS spectrum of O 1s electrons from the tantalum oxynitride thin film deposition attempt. The O= $-$ C and O= $-$ X contributions likely correspond to either carbon impurities or oxidation on the surface, though the intensity in the O= $-$ X contribution is too small to accurately specify.

### 6.4.3 UV/Vis absorption spectroscopy - Film absorption

The UV/Vis absorbance for the TaON thin film peaked in approximately the 200-220 nm region of the spectrum, as seen in figure 6.27. Although this is largely different to the peak in the 400 nm region given by the TaON film in G. Hitoki's work, it is very similar to the peak caused by the  $\text{Ta}_2\text{O}_5$  film in the same figure [1] (see 2.6 in chapter 2), suggesting the

film largely comprised tantalum oxide, which is consistent with the EDX results.

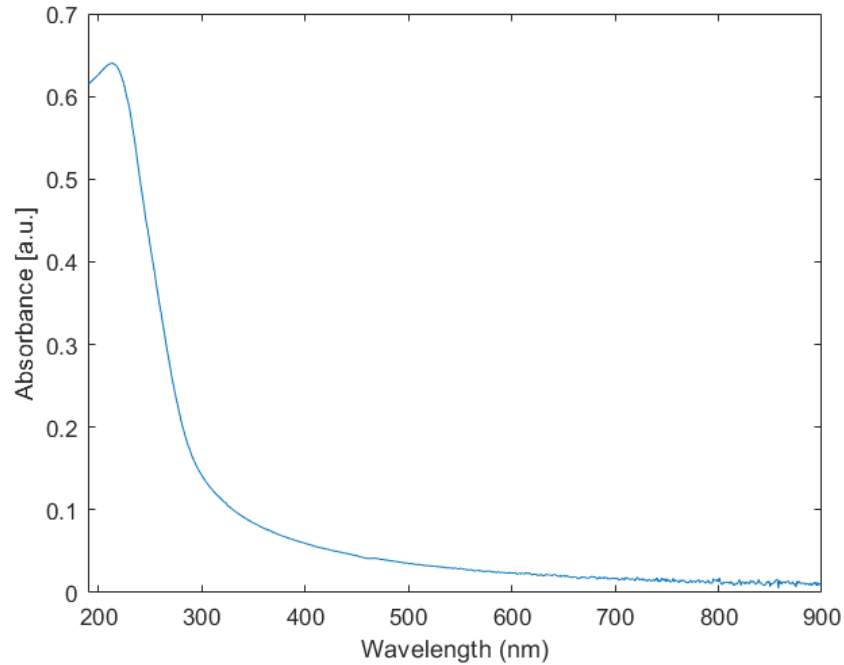


Figure 6.27: UV/Vis absorption spectrum for deposited TaON film, with absorption profile for plain quartz substrate subtracted.

## 6.5 Conclusions

SEM images showed deposited material was a layer of  $\text{TiO}_2$  with little homogeneity, with spherical particulates on top. EDX and XPS evidence unfortunately show almost no nitrogen in the film. EDX shows little, but is unreliable due to close peaks with other elements including Ti and O. Additionally, the Ta peaks are close to the Si peaks, meaning the amount of tantalum detected in the two respective thin films is unreliable. With this in mind, it is imperative to conclude that EDX is not a suitable nor reliable diagnostic to determine the chemical composition of titanium or tantalum oxide/oxy-nitride thin films deposited onto silicon substrates. XPS results showed  $\text{TiO}_2$  was present on all titanium compound thin films, including the titanium oxy-nitride film attempts, with the O/Ti ratio consistently lying between 1.95-1.99, and almost no detection of nitrogen to perform a stoichiometry calculation. XRD showed the films are amorphous in structure, with no crystalline material. The UV/Vis absorption spectroscopy results showed that for both the titanium and tantalum compound thin films, titanium oxide and tantalum oxide are being deposited respectively,

producing absorption peaks between 200-270 nm, similar to previous literature [1, 15, 127]. When comparing the UV/Vis absorption peaks between deposited titanium compound thin films at different pressures, no significant shift in the peak is observed, which is consistent with literature [74]. Finally, the tantalum oxide deposition attempt did not show UV/Vis absorption peaks which matched G. Hitoki's work [1], but the tantalum oxynitride attempt did, which further implied the deposited material was tantalum oxide with small amounts of nitrogen. Analysis methods in this work do not allow for differentiation between different plasma admixture ratios. Despite changing the background plasma conditions to optimise the N content, the films are heavily dominated by O content. It is clear that there is preferential interaction with oxygen despite there being a higher density of N in the plasma. It remains unclear whether the non-metal plasma, e.g. oxygen, and the metal plasma plume are reacting before they reach the substrate surface, or if the plume reaches the surface first, with the oxygen forming after the end of the laser pulse and plasma plume. The results in this chapter show this particular method of producing oxynitride thin films needs improving.

## 6.6 Suggestions for future investigation

Titanium oxide can be deposited with this method. Therefore, deposition with a TiN target in an oxygen background plasma could be feasible. However, the method is not as promising as it was suggested in controlling the content of individual elements. Moreover, it is worth studying the oxygen-nitrogen plasma chemistry, as well as the chemistry of the plume with the plasma background. In particular, the fraction of background plasma which successfully reacts with the plume is of key importance. An important question to address is how the content is being deposited onto the substrate, and the order at which the different chemical interactions take place before deposition.

XRD shows that there is only amorphous material, which could mean substrate heating is required after all to improve the crystal structure of the films. Annealing may also be required for better quality film growth, which unfortunately disregards the suggested PE-PLD advantage of no annealing required, but does at least maintain the most important advantage of controlling the stoichiometry.

## Chapter 7

# Conclusions

### 7.1 Conclusions with respect to project aims

Work presented in this thesis was centred around the thin film deposition technique, PE-PLD, and its suitability in producing metal oxynitride thin films for photocatalytic water splitting. Three integral parts of the technique were investigated: first, the laser ablation of different metal plasma plumes was modelled using the hydrodynamic code POLLUX, to explore the link between material properties and plasma plume characteristics. Secondly, the TALIF diagnostic measured ground-state densities of pure O<sub>2</sub> and N<sub>2</sub> plasmas, as well as O<sub>2</sub>/N<sub>2</sub> plasma admixtures, to establish which parameters provided the most control over the O:N density ratio. Thirdly, thin films were deposited using the PE-PLD setup in the YPI laboratories and analysed using multiple diagnostic techniques to observe key characteristics. These diagnostics included SEM and EDX analysis to determine the chemical composition and surface morphology; XPS analysis to determine the chemical stoichiometry; XRD analysis to observe the crystal structure; and UV/Vis spectroscopy to determine the film absorption.

There were two stages to the POLLUX investigation: first, titanium plumes were modelled as a benchmark, creating non-existing “Ti-variant” materials which varied in parameters that otherwise could not be varied experimentally, such as atomic number, to investigate the effects of those parameters on the subsequent plume behaviour. Secondly, six real elements were modelled to verify the links established by the Ti-variants. POLLUX successfully highlighted that the atomic number of the target material had the greatest effect on the electron temperature and mass density of the plasma plume, and is likely the parameter which dic-

tates the coupling of energy via inverse bremsstrahlung. On the other hand, the mass density of the target material is likely the parameter responsible for the plume expansion. Parameters such as thermal conductivity and melting temperature of the target material had little to no effect on plume parameters. These successful results provide a deeper understanding of the laser ablation of pure metal targets in PE-PLD, as well as other similar laser ablation applications.

The investigation with the TALIF diagnostic also took place in two stages: verifying the ground-state atomic densities of pure O<sub>2</sub> and N<sub>2</sub> plasma, as well as plasma mixtures comprising both species; and subsequently determining the O:N atomic density ratio to learn which plasma parameters influenced this ratio the most. There were clear differences in how varying RF plasma power and chamber pressure affected the change in atomic density between pure oxygen and pure nitrogen plasmas: atomic nitrogen density showing a clear, linear correlation with RF power compared to pressure, which produced little variation in atomic density; and atomic oxygen density displaying a linear increase with pressure and a much smaller increase with power. These differences are likely due to differences in electron energy loss via vibrational excitation between the two species. Varying the plasma power and pressure caused the O:N atomic density ratio to change by up to factors of 20-30, but varying the relative flow input of oxygen and nitrogen in O<sub>2</sub>/N<sub>2</sub> plasma admixtures had the greatest influence and control over the plasma content, allowing the density ratio to change by up to a factor of 100. This provides valuable insight into the varying plasma content in PE-PLD and other plasma-assisted applications.

The thin-film analysis showed unexpected yet consistent results between the diagnostics. SEM images showed that deposition content was spread in an inhomogeneous layer topped with non-spherical particulates, and XRD analysis revealed the thin films were amorphous. EDX and XPS analysis showed almost no nitrogen present in the films deposited with an O<sub>2</sub>/N<sub>2</sub> background plasma, and peaks on XPS spectra largely resembled TiO<sub>2</sub> for all films deposited with a Ti target. EDX stoichiometry calculations of each of the three titanium oxynitride deposition attempts gave O/Ti ratios as low as  $3.033 \pm 0.038$  and as high as  $3.576 \pm 0.950$ , while calculating N/Ti ratios of  $0.278 \pm 0.097$  at best and nothing at all at worst. Moreover, the amount of nitrogen detected by XPS was insufficient to even produce a stoichiometry, producing stoichiometries between TiO<sub>1.97</sub> and TiO<sub>1.99</sub> instead. The TiN deposition attempt showed unexpected results, with little to no nitrogen present on the

substrate, yet substantially more oxygen, likely due to oxidation. The lack of nitrogen suggests the nitrogen plasma is struggling to react with the metal plasma plume. EDX analysis was found to be an unreliable diagnostic for examining the chemical composition of titanium and tantalum compound thin films on silicon substrates due to N and Ti peaks overlapping with each other, making them difficult to distinguish, while Ta and Si peaks also overlapped with each other. Tantalum thin film depositions were attempted with even less success, with stoichiometries for the tantalum oxide and oxynitride thin films calculated by EDX as  $\text{Ta}_2\text{O}_{6.598 \pm 0.523}$  and  $\text{TaO}_{2.898 \pm 0.326}\text{N}_{0.128 \pm 0.001}$  respectively, while XPS produced stoichiometries of  $\text{Ta}_2\text{O}_{3.64}$  and  $\text{TaO}_{1.53}$  respectively, with insufficient nitrogen detected as with the titanium oxynitride deposition attempts. UV/Vis spectroscopy results showed the absorption for all thin film deposition attempts were within the 200-300 nm range of the spectrum, making them not very effective for photocatalysis, as expected with their stoichiometries. The titanium films with more nitrogen in their calculated stoichiometry give absorbance peaks that lie closer to the visible range than those with less or no nitrogen, suggesting that nitrogen does still improve the absorbance, provided more nitrogen is present on the film. Overall, the lack of nitrogen present on the films despite the conclusions gained from the background plasma characterisation work shows there is a clear gap in the knowledge of the plasma chemistry which takes place in PE-PLD, particularly the interactions between the  $\text{O}_2/\text{N}_2$  plasma species and their effect on the deposition of material onto the substrate.

## 7.2 Suggestions for future work

Although the disappointing results from the thin film analysis have shown PE-PLD is currently not as adequate in producing photocatalytic metal oxynitride thin films as previous work has suggested, they have highlighted many areas lacking in knowledge which could be expounded upon using the success from some of the other results in this work such as the plume modelling and  $\text{O}_2:\text{N}_2$  plasma characterisation, as well as by other means suggested below, as a pointer in the right direction.

The most obvious area in need of address is the complex oxygen:nitrogen plasma chemistry, which is lacking in literature at present. As oxygen and nitrogen plasma species are generally more reactive than metal plasma plumes, it is likely that reactions between different oxygen and nitrogen species may take place before the metal plasma plume is able to

react, forming products such as NO, NO<sup>+</sup>, and NO<sub>2</sub><sup>+</sup>, some of which may not interact with the metal plume at all, which could explain the lack of nitrogen deposited. It is likely that Zel'dovich reactions involving species with oxygen and nitrogen, as well as ozone formation reactions, are taking place in the chamber. Many of the reaction mechanisms in LTPs and individual reaction rates are largely unknown, and so the development of such mechanisms and rate constants, corroborated with benchmark experiments, would prove beneficial to research in PE-PLD as well as wider LTP research involving applications of nitrogen and oxygen plasma discharges.

The method and order in which the material from different sources is being deposited onto the substrate is also lacking information. For metal oxide thin films, it is ambiguous whether the oxygen background plasma reacts with the plasma plume first, producing metal oxide plasma before deposition, or if the plume and background plasma deposit at separate times, producing metal oxide on the substrate at a later point in time. An extra step will also be required for TiON, when nitrogen plasma is also present. It remains unclear whether the non-metal background plasma and the metal plasma plume are reacting before they reach the substrate surface, or if the plume reaches the surface first, with the oxygen/nitrogen forming after the end of the laser pulse and plasma plume. A model which can address the plume interaction with the background plasma may construct a clearer picture of the chemical and physical processes that occur within the chamber, especially when combined with models such as POLLUX and HPEM [26].

TALIF results have shown controlling the flow ratio of O<sub>2</sub>:N<sub>2</sub> plasma provides the most control over the admixture tuning, but this cannot be used to its full potential if it is unclear how the species interact with each other. Presently, there is literature that outlines the basics of kinetic modelling in low-temperature O<sub>2</sub>:N<sub>2</sub> plasmas [122], providing the reader with detailed knowledge to build an O<sub>2</sub>-N<sub>2</sub> plasma model, but leaves many questions to address, particularly plasma-surface interactions. As PLD has regularly been shown to require additional oxygen for metal oxide film growth, it is vital to learn more about the underlying chemistry of the material deposition onto the substrate.

This work has shown PE-PLD can produce stoichiometric TiO<sub>2</sub> thin films with relative ease as evidenced by EDX and XPS analysis, suggesting pure oxygen plasma interacts well with Ti plumes. Therefore, the use of TiN targets and O<sub>2</sub> plasma may produce TiON films with improved stoichiometry. Target and substrate heating may supplement the stoichiom-

etry, despite ignoring benefits previously suggested by PE-PLD. With these suggestions for future work, a revised PE-PLD method capable of successfully depositing stoichiometric metal oxynitride thin films for photocatalytic water splitting may yet be achievable.

## Appendix A

# List of publications and communications

*Prior to the publication of this thesis, work within has been published and presented in the following literature and conferences:*

### Publications

**M. Hill**, E. Waganaars. Modelling of Plasma Temperatures and Densities in Laser Ablation Plumes of Different Metals. *Photonics*, **9**, 937. <https://doi.org/10.3390/photonics9120937> (2022)

### Oral presentations

**M. Hill**, E. Waganaars. Investigating the Plasma Physics of Plasma-Enhanced Pulsed Laser Deposition of Photocatalytic Thin Films, *IOP Plasma Surfaces and Thin Films* (2023)

**M. Hill**. Thin films: tiny materials with tremendous potential, *University of York Three Minute Thesis* (2023)

**M. Hill**, E. Waganaars. Investigating the Plasma Physics of Plasma-Enhanced Pulsed Laser Deposition of Photocatalytic Thin Films, *49th International Conference on Metallurgical Coatings & Thin Films* (2023)

**Poster presentations**

**M. Hill**, E. Wagenaars. Comparison of material properties of plasma plumes using ns-pulsed laser ablation modelling, *IOP Plasma Surfaces and Thin Films* (2022)

# List of References

- [1] G. Hitoki et al. An oxynitride, TaON, as an efficient water oxidation photocatalyst under visible light irradiation ( $\lambda \leq 500$  nm). *Chem. Commun.*, pages 1698–1699, 2002.
- [2] K. Niemi et al. Absolute atomic oxygen density measurements by two-photon absorption laser-induced fluorescence spectroscopy in an RF-excited atmospheric pressure plasma jet. *Plasma Sources Sci. Technol.*, 14:375, 2005.
- [3] K. Gazeli et al. Progresses on the use of two-photon absorption laser induced fluorescence (TALIF) diagnostics for measuring absolute atomid densities in plasmas and flames. *Plasma*, 4:145, 2021.
- [4] T. Bird. Understanding and controlling the reactivity of metal oxide nanoparticles. PhD thesis. *University of York*, 2022.
- [5] P. Auger et al. The Auger effect. *Surf. Sci.*, 48(1):1, 1975.
- [6] K. L. Chopra and I. Kaur. *Thin Film Device Applications*. Plenum Press: New York and London, 1983.
- [7] C. Julien et al. Growth of  $V_2O_5$  thin films by pulsed laser deposition and their applications in lithium microbatteries. *Materials Science and Engineering B.*, 65:170, 1999.
- [8] B. M. Hidalgo-Robatto et al. Pulsed laser deposition of copper and zinc doped hydroxyapatite coatings for biomedical applications. *Surface & Coatings Technology*, 333:168, 2018.
- [9] M. A. El Khakani et al. Pulsed laser deposition of nanostructured tin oxide films for gas sensing applications. *Sensors and Actuators B*, 77:383, 2001.

- [10] D. Djikkamp and T. Venkatesan. Preparation of Y-Ba-Cu oxide superconductor thin films using pulsed laser evaporation from high  $T_c$  bulk material. *Appl. Phys. Lett.*, 51:619, 1987.
- [11] P. P. Edwards et al. Hydrogen and fuel cells: Towards a sustainable energy future. *Energy Policy*, 36:4356, 2008.
- [12] G. Nicoletti et al. A technical and environmental comparison between hydrogen and some fossil fuels. *Energ. Convers. Manage.*, 89:205, 2015.
- [13] S. Rajendiran et al. Plasma-enhanced pulsed laser deposition of copper oxide and zinc oxide thin films. *AIP Advances*, 10, 2020.
- [14] H. N. C. Dharma et al. A review of titanium dioxide  $\text{TiO}_2$ -based photocatalyst for oilfield-produced water treatment. *Membranes*, 12(3):345, 2022.
- [15] K. Honda and A. Fujishima. Electrochemical photolysis of water at a semiconductor electrode. *Nature*, 238:37, 1972.
- [16] A. Fuertes. Chemistry and applications of oxynitride perovskites. *J. Mater. Chem.*, 22:3293, 2012.
- [17] K. Maeda and K. Domen. New non-oxide photocatalysts designed for overall water splitting under visible light. *J. Phys. Chem. C*, 111:7851, 2007.
- [18] F. Dong et al. Band structure and visible light photocatalytic activity of multi-type nitrogen doped  $\text{TiO}_2$  nanoparticles prepared by thermal decomposition. *J. Hazard. Mater*, 162:763, 2009.
- [19] J. A. Greer. History and current status of commercial pulsed laser deposition equipment. *J. Phys. D: Appl. Phys.*, 47(034005), 2014.
- [20] M. Escalona et al. Study of titanium nitride film growth by plasma-enhanced pulsed laser deposition at different experimental conditions. *Surf. Coat. Technol.*, 405(126492), 2021.
- [21] S. H. Huang et al. Room temperature radio-frequency plasma-enhanced pulsed laser deposition of ZnO thin films. *Appl. Surf. Sci*, 266:194, 2013.

- [22] A. De Giacomo et al. Spectroscopic investigation of the technique of plasma assisted pulsed laser deposition of titanium dioxide. *Spectrochim.*, 56:1459, 2001.
- [23] M. Escalona et al. Comparative study on the dynamics and the composition between a pulsed laser deposition (PLD) and a plasma enhanced PLD (PE-PLD). *Results Phys*, 24(104066), 2021.
- [24] G. J. Pert. Inverse bremsstrahlung absorption in large radiation fields during binary collisions-classical theory. II. integrated rate coefficients for Coulomb collisions. *Journal of Physics A: Mathematical and General*, 9(3):463, 1976.
- [25] G. J. Pert. Inverse bremsstrahlung absorption in large radiation fields during binary collisions-classical theory. II(b). summed rate coefficients for Coulomb collisions. *Journal of Physics A: Mathematical and General*, 9(10):1797, 1976.
- [26] M. J. Kushner. Hybrid modelling of low temperature plasmas for fundamental investigations and equipment design. *J. Phys. D: Appl. Phys.*, 42:194013, 2009.
- [27] S. Rajendiran. Plasma-enhanced pulsed laser deposition. PhD thesis. *University of York*, 2017.
- [28] D. Meehan. Plasma-enhanced pulsed laser deposition: A study of laser produced and radio frequency plasmas, and deposited films. PhD thesis. *University of York*, 2019.
- [29] E. Hecht. *Optics, Global ed.* Harlow: Pearson Education, Limited, 2016.
- [30] J. Heller et al. Temperature dependence of the reflectivity of silicon with surface oxide at wavelengths of 633 and 1047 nm. *Appl. Phys. Lett.*, 75:43–45, 1999.
- [31] T. T. D. Huynh and N. Semmar. In situ probing of pulsed laser melting and laser-induced periodic surface structures formation by dynamic reflectivity. *Surf. Topogr.: Metrol. Prop.*, 5:1459, 2017.
- [32] T. G. Mayerhöfer et al. Employing theories far beyond their limits—the case of the (Boguer-) Beer–Lambert Law. *Chem. Phys. Chem.*, 17(13):1948, 2016.
- [33] D. Bäuerle. *Laser Processing and Chemistry.* Springer Science & Business Media, 2013.
- [34] S. Link et al. Laser photothermal melting and fragmentation of gold nanorods: Energy and laser pulse-width dependence. *J. Phys. Chem. A*, 103(9):1165, 1999.

- [35] B. N. Chichkov et al. Femtosecond, picosecond and nanosecond laser ablation of solids. *Appl. Phys. A*, 63:109–115, 1996.
- [36] S. Rand. Inverse bremsstrahlung with high-intensity radiation fields. *Phys. Rev.*, 136(1B):B231, 1964.
- [37] J. F. Seely and E. G. Harris. Heating of a plasma by multiphoton inverse bremsstrahlung. *Phys. Rev. A*, 7(3):1064, 1973.
- [38] G. J. Tallents. *An introduction to the atomic and radiation physics of plasmas*. Cambridge University Press, 2018.
- [39] A. Miziolek, V. Palleschi, and I. Schechter. *Laser induced breakdown spectroscopy*. Cambridge University Press, 2006.
- [40] R. Cong et al. Measurement of photoionization cross sections of the excited states of titanium, cobalt, and nickel. *J. Appl. Phys.*, 106:013103, 2009.
- [41] S. I. Anisimov et al. An analytical model for three-dimensional laser plume expansion into vacuum in hydrodynamic regime. *Appl. Surf. Sci.*, 96:24, 1996.
- [42] M. W. Stapleton et al. Expansion dynamics and equilibrium conditions in a laser ablation plume of lithium: Modeling and experiment. *J. Appl. Phys.*, 97(6):064904, 2005.
- [43] K. Orsel et al. Spatial and temporal mapping of Al and AlO during oxidation in pulsed laser ablation of LaAlO<sub>3</sub>. *J. Instrum.*, 8(10):10021, 2013.
- [44] R. Eason. *Pulsed laser deposition of thin films: applications-led growth of functional materials*. Wiley, 2006.
- [45] S. L. Gupta and R. K. Thareja. ZnO thin film deposition using colliding plasma plumes and single plasma plume: Structural and optical properties. *J. Appl. Phys.*, 114:224903, 2013.
- [46] I. Petrov et al. Microstructural evolution during film growth. *J. Vac. Sci. Technol. A*, 21(5):117, 2003.
- [47] Y.-Q. Hou et al. Influence of annealing temperature on the properties of titanium oxide thin film. *Appl. Surf. Sci.*, 218:97, 2003.

- [48] A. Y. Cho and J. R. Arthur. Molecular beam epitaxy. *Prog. Solid State Ch.*, 10(3):157, 1975.
- [49] X. L. Li et al. Thermodynamic theory of growth of nanostructures. *Prog. Mater. Sci.*, 64:121, 2014.
- [50] M. Lieberman and A. Lichtenberg. *Principles of plasma discharges and materials processing 2nd ed.* Wiley-Interscience, 2005.
- [51] H. Conrads and M. Schmidt. Plasma generation and plasma sources. *Plasma Sources Sci. Technol.*, 9(4):441, 2000.
- [52] H. Liu et al. Wavelength-dependent variations of the electron characteristics in laser-induced plasmas: A combined hydrodynamic and adiabatic expansion modelling and time-gated, optical emission imaging study. *Journal of Applied Physics*, 125(083304), 2019.
- [53] G. Cristoforetti et al. Investigation on the role of air in the dynamical evolution and thermodynamic state of a laser-induced aluminium plasma by spatial- and time-resolved spectroscopy. *Spectrochim. Acta Part B*, 65:787, 2010.
- [54] G. Cristoforetti et al. Local Thermodynamic Equilibrium in Laser-Induced Breakdown Spectroscopy: Beyond the McWhirter criterion. *Spectrochim. Acta Part B*, 65:86, 2010.
- [55] W. Yang et al. Strategies for enhancing the photocurrent, photovoltage, and stability of photoelectrodes for photoelectrochemical water splitting. *Chem. Soc. Rev.*, 48:4979, 2019.
- [56] B. A. Pinaud et al. Technical and economic feasibility of centralized facilities for solar hydrogen production via photocatalysis and photoelectrochemistry. *Energy Environ. Sci.*, 6:1983, 2013.
- [57] H. Ahmad et al. Hydrogen from photo-catalytic water splitting process: A review. *Renew. and Sust. Energ. Rev.*, 43:599, 2015.
- [58] K. Lalitha et al. Continuous hydrogen production activity over finely dispersed Ag<sub>2</sub>O/TiO<sub>2</sub> catalysts from methanol:water mixtures under solar irradiation: a structure–activity correlation. *Int. J. Hydrogen Energy.*, 35:3991, 2010.

- [59] N.-L. Wu and M.-S. Lee. Enhanced  $\text{TiO}_2$  photocatalysis by Cu in hydrogen production from aqueous methanol solution. *Int. J. Hydrogen Energy.*, 29:1601, 2004.
- [60] C. W. Lai and S. Sreekantan. Preparation of hybrid  $\text{WO}_3$ - $\text{TiO}_2$  nanotube photoelectrodes using anodization and wet impregnation: improved water-splitting hydrogen generation performance. *Int. J. Hydrogen Energy.*, 38:2156, 2013.
- [61] J. Georgieva et al. Bi-component semiconductor oxide photoanodes for the photoelectrocatalytic oxidation of organic solutes and vapours: a short review with emphasis to  $\text{TiO}_2$ - $\text{WO}_3$  photoanodes. *Int. J. Hydrogen Energy.*, 38:211, 2012.
- [62] T. T. ThanhThuy et al. Photocatalytic degradation of pentachlorophenol on  $\text{ZnSe}/\text{TiO}_2$  supported by photo-fenton system. *Chem. Eng. J.*, 223:379, 2013.
- [63] H. Park et al. Surface modification of  $\text{TiO}_2$  photo-catalyst for environmental applications. *J. Photochem. Photobiol C.*, 15:1, 2013.
- [64] N. R. Khalid et al. Graphene modified  $\text{Nd}/\text{TiO}_2$  photocatalyst for methyl orange degradation under visible light irradiation. *Ceram. Int.*, 39:3569, 2013.
- [65] X. Jiang et al. Graphene oxide as a chemically tunable 2-d material for visible-light photocatalyst applications. *J. Catal.*, 299:204, 2013.
- [66] V. N. H. Nguyen et al. Effect of formate and methanol on photoreduction/removal of toxic cadmium ions using  $\text{TiO}_2$  semiconductor as photocatalyst. *Chem. Eng. Sci.*, 58:4429, 2003.
- [67] W.-Y. Wang and K. Young. Effect of solution pH on the adsorption and photocatalytic reaction behaviors of dyes using  $\text{TiO}_2$  and Nafion-coated  $\text{TiO}_2$ . *Colloids Surf., A.*, 302:261, 2007.
- [68] S. P. Meshram et al. Facile synthesis of  $\text{CuO}$  nanomorphs and their morphology dependent sunlight driven photocatalytic properties. *Chem. Eng. J.*, 302:158, 2012.
- [69] T. T. Le et al. Water splitting on Rh B dye sensitized Co-doped  $\text{TiO}_2$  catalyst under visible light. *Chem. Eng. J.*, 111-112:397, 2012.
- [70] C. Siritwong et al. Doped-metal oxide nanoparticles for use as photo-catalysts. *Prog. Cryst. Growth Charact. Mater.*, 58:145, 2012.

- [71] J. S. Jang et al. Heterojunction semiconductors: a strategy to develop efficient photocatalytic materials for visible light water splitting. *Catal Today*, 185:270, 2012.
- [72] J. Zhu and M. Zäch. Nanostructured materials for photocatalytic hydrogen production. *Curr Opin Colloid Interface Sci.*, 14:260, 2009.
- [73] M. Yamaguchi et al. Black titanium oxynitride thin films prepared by nitrogen plasma-assisted pulsed laser deposition for flat-panel displays. *Appl. Surf. Sci.*, 534:147616, 2020.
- [74] N. R. Mucha et al. Electrical and optical properties of titanium oxynitride thin films. *J Mater. Sci.*, 55:5123–5134, 2020.
- [75] P. J. Hargis et al. The Gaseous Electronics Conference radio-frequency reference cell: A defined parallel-plate radio-frequency system for experimental and theoretical studies of plasma-processing discharges. *Rev. Sci. Instrum.*, 65(1):140, 1994.
- [76] G. J. Pert. Models of laser-plasma ablation. *Journal of Plasma Physics*, 35(1):43, 1986.
- [77] G. J. Pert. Models of laser-plasma ablation part 2 – steady-state theory: Self-regulating flow. *Journal of Plasma Physics*, 36(1):415, 1986.
- [78] G. J. Pert. Models of laser-plasma ablation part 3 - steady-state theory: deflagration flow. *Journal of Plasma Physics*, 39(1):241, 1988.
- [79] G. J. Pert. Two-dimensional hydrodynamic models of laser-produced plasmas. *Journal of Plasma Physics*, 39(1):263, 1989.
- [80] M. S. Qaisar and G. J. Pert. Laser ablation of Mg, Cu and Pb using infrared and ultraviolet low-fluence lasers. *Journal of Applied Physics*, 94(10):1468, 2014.
- [81] S. Rajendiran et al. Modelling of laser ablation and reactive oxygen plasmas for pulsed laser deposition of zinc oxide. *Surface & Coatings Technology*, 260(10):417, 2014.
- [82] J. P. Boris and D. L. Book. Flux-corrected transport. I. SHASTA, a fluid transport algorithm that works. *Journal of Computational Physics*, 11(1):38, 1973.
- [83] S. L. Thompson. Improvements in the Chart-D radiation-hydrodynamic code I: analytic equations of state, Sandia Labs Report. (SC-RR-70-28), 1970.

- [84] R. Latter. Temperature behavior of the Thomas-Fermi statistical model for atoms. *Physical Review*, 99(1):1854, 1955.
- [85] D. S. Kershaw. The incomplete Cholesky—conjugate gradient method for the iterative solution of systems of linear equations. *Journal of Computational Physics*, 26(1):1854, 1978.
- [86] Periodic Table. *Royal Society of Chemistry*, 2021.
- [87] J. Zhang et al. Thermal equations of state for titanium obtained by high pressure – temperature diffraction studies. *Physical Review B*, 78(054119), 2008.
- [88] K. W. Katahara. Pressure derivatives of the elastic moduli of niobium and tantalum. *Journal of Applied Physics*, 47:434, 2008.
- [89] G. I. Kerley. Equations of state for Titanium and Ti6Al4V alloy. *Sandia Report*, (SAND 2003-3785), 2003.
- [90] C. W. Greeff and J. D. Johnson. New Sesame equation of state for tantalum. *Los Alamos Report*, (LA-13681-MS), 2000.
- [91] C. Kittel and P. McEuen. *Introduction to Solid State Physics*. John Wiley & Sons, 2000.
- [92] P. D. Desai. Thermodynamic properties of Aluminium. *International Journal of Thermophysics*, 8:621, 1987.
- [93] J. W. Arblaster. Thermodynamic properties of Gold. *Journal of Phase Equilibria and Diffusion*, 37:229, 2016.
- [94] J. R. McCreary and R. J. Thorn. Enthalpy of sublimation of Zinc and Cadmium. *Journal of Chemical Physics*, 50:3725, 1969.
- [95] J. W. Arblaster. Thermodynamic properties of Copper. *Journal of Phase Equilibria and Diffusion*, 36:422, 2015.
- [96] P. D. Desai. Thermodynamic properties of Titanium. *International Journal of Thermophysics*, 8:781, 1987.

- [97] J. W. Arblaster. Thermodynamic properties of Tantalum. *J. Phase. Equilib. Diffus.*, 39:255, 2018.
- [98] Properties of Chemical Elements. *Material Properties*, 2021.
- [99] G. J. Pert. Approximations for the rapid evaluation of the Thomas-Fermi equation. *J. Phys. B: At. Mol. Opt. Phys.*, 32(2):415, 1999.
- [100] J. Hermann et al. Local thermodynamic equilibrium in a laser-induced plasma evidenced by blackbody radiation. *Spectrochim. Acta Part B*, 144:82, 2018.
- [101] L. Spitzer Jr and R. Härm. Transport phenomena in a completely ionized gas. *Phys. Rev.*, 89(5):977, 1953.
- [102] G. J. Pert. The hybrid model and its application for studying free expansion. *J. Fluid Mech.*, 131:401, 1983.
- [103] K. Niemi et al. Absolute calibration of atomic density measurements by laser-induced fluorescence spectroscopy with two-photon excitation. *J. Phys. D: Appl. Phys.*, 34(15):2330, 2001.
- [104] J. Ellis. An investigation into plasma surface interactions, focussing on surface produced, and surface assisted, negative ion generation. PhD thesis. *University of York*, 2020.
- [105] G. D. Stancu. Two-photon absorption laser induced fluorescence: rate and density-matrix regimes for plasma diagnostics. *Plasma Sources Sci. Technol.*, 29:054001, 2020.
- [106] W. K. Bischel. Two-photon laser-induced fluorescence in oxygen and nitrogen atoms. *Chem. Phys. Lett.*, 82:85, 1981.
- [107] S. Schröter et al. The formation of atomic oxygen and hydrogen in atmospheric pressure plasmas containing humidity: picosecond two-photon absorption laser-induced fluorescence and numerical simulations. *Plasma Sources Sci. Technol.*, 29:105001, 2020.
- [108] H. Horiguchi et al. Radiative lifetimes and two-body collisional deactivation rate constants in Ar for Xe( $5p^56p$ ), Xe( $5p^56p$ ), and Xe( $5p^57p$ ) states. *J. Chem. Phys.*, 75:1207, 1981.

- [109] A. T. West. Optical and Electrical Diagnosis of Atmospheric Pressure Plasma jets. PhD thesis. *University of York*, 2024.
- [110] S. Gražulis et al. Crystallography open database – an open-access collection of crystal structures. *J. Appl. Cryst.*, 42:726, 2009.
- [111] R. Jenkins et al. JCPDS — International Centre for Diffraction Data Sample Preparation Methods in X-Ray Powder Diffraction. *J. Appl. Cryst.*, 1(2):51, 1986.
- [112] M. P. Seah. The quantitative analysis of surfaces by XPS: A review. *Surf. Interface Anal.*, 2(6):222, 1980.
- [113] J. Végh. The Shirley background revised. *J. Electron Spectrosc. & Relat. Phenom.*, 151:159, 2006.
- [114] M. K. T. Mo. Atomic Oxygen Densities in Pulsed Inductively Coupled Plasmas: — Laser Spectroscopy and — Energy Resolved Actinometry. PhD thesis. *University of York*, 2023.
- [115] C.-C. Hsu et al. Comparison of model and experiment for Ar, Ar/O<sub>2</sub>. and Ar/O<sub>2</sub>/Cl<sub>2</sub> inductively-coupled plasmas. *J. Phys. D: Appl. Phys.*, 39:3272, 2006.
- [116] K. J. Taylor and G. R. Tynan. Control of dissociation by varying oxygen pressure in noble gas admixtures for plasma processing. *J. Vac. Sci. Technol. A*, 23(4):643–650, 2005.
- [117] C. S. Corr et al. Discharge kinetics of inductively coupled oxygen plasmas: experiment and model. *Plasma Sources Sci. Technol.*, 21(5):055024, 2012.
- [118] J. T. Gudmundsson et al. Electronegativity of low-pressure high-density oxygen discharges. *J. Phys. D: Appl. Phys.*, 34:1100, 2001.
- [119] T. L. Chng et al. TALIF measurements of atomic nitrogen in the afterglow of a nanosecond capillary discharge. *Plasma Sources Sci. Technol.*, 29:035017, 2020.
- [120] S. F. Adams and T. A. Miller. Two-photon absorption laser-induced fluorescence of atomic nitrogen by an alternative excitation scheme. *Chem. Phys. Lett.*, 295:305, 1998.

- [121] E. I. Toader. Experimental electron energy distribution functions in argon, nitrogen, and oxygen high-density and low-pressure reflex and microwave plasma sources. *Plasma Sources Sci. Technol.*, 13:646, 2004.
- [122] V. Guerra et al. Modelling  $N_2$ - $O_2$  plasmas: volume and surface kinetics. *Plasma Sources Sci. Technol.*, 28:073001, 2019.
- [123] K. Katsonis and C. Berenguer. Global modeling of  $N_2O$  discharges: Rate Coefficients and Comparison with ICP and Glow Discharges Results. *Int. J. Aerosp. Eng.*, 2013:737463, 2013.
- [124] D. Burnette. Nitric oxide kinetics in the afterglow of a diffuse plasma filament. *Plasma Sources Sci. Technol.*, 23:045007, 2014.
- [125] K. Kanaya and S. Okayama. Penetration and energy-loss theory of electrons in solid targets. *J. Phys. D: Appl. Phys.*, 5:43, 1972.
- [126] Y. Hu and C. Yuan. Low-temperature preparation of photocatalytic  $TiO_2$  thin films from anatase sols. *J. Cryst. Growth*, 274:563, 2005.
- [127] J. Dharma, A. Piscal, and C. T. Shelton. Simple method of measuring the band gap energy value of  $TiO_2$  in the powder form using a UV/Vis/NIR spectrometer. *Application Note Shelton, CT:PerkinElmer*, pages 1–4, 2009.
- [128] E. Arpaç et al. Photocatalytic performance of Sn-doped and undoped  $TiO_2$  nanostructured thin films under UV and vis-lights. *J. Hazard. Mater.*, 140(1-2):69, 2007.
- [129] X. Y. Chen et al. Annealing and oxidation of silicon oxide films prepared by plasma-enhanced chemical vapor deposition. *J. Appl. Phys.*, 97:014913, 2005.
- [130] G. F. Cerofolini et al. Gas-phase room-temperature oxidation of (100) silicon. *Appl. Surf. Sci.*, 93:255, 1996.
- [131] H. Chen and F. Lu. Oxidation behaviour of titanium nitride films. *J. Vac. Sci. Technol. A*, 23:1006, 2005.
- [132] X-ray photoelectron spectroscopy of atomic elements. *ThermoFisher*, 2024.